

NONEQUILIBRIUM GREEN'S FUNCTION
FORMALISM FOR TOPOLOGICAL
MATERIALS AND SOME APPLICATIONS

A thesis

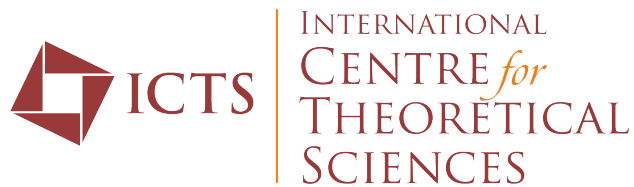
SUBMITTED TO THE
TATA INSTITUTE OF FUNDAMENTAL RESEARCH, MUMBAI

for the degree of

DOCTOR OF PHILOSOPHY IN PHYSICS

by

JUNAID MAJEED BHAT



TATA INSTITUTE OF FUNDAMENTAL RESEARCH

INTERNATIONAL CENTRE FOR THEORETICAL SCIENCES, BENGALURU,
INDIA-560089

AUGUST 2023

DECLARATION

This thesis is a presentation of my original research work. Wherever contributions of others are involved, every effort is made to indicate this clearly, with due reference to the literature, and acknowledgement of collaborative research and discussions. The work was done under the guidance of Prof. Abhishek Dhar, at the International Centre for Theoretical Sciences, Tata Institute of Fundamental Research, Bengaluru.



Junaid Majeed Bhat

In my capacity as supervisor of the candidates thesis, I certify that the above statements are true to the best of my knowledge.



Prof. Abhishek Dhar



Date

Publications relevant to the thesis

1. Junaid Majeed Bhat and Abhishek Dhar. Transport in spinless superconducting wires. *Physical review B*, 102:224512, Dec 2020. <https://link.aps.org/doi/10.1103/PhysRevB.102.224512>.
2. Junaid Majeed Bhat and Abhishek Dhar. Equivalence of negf and scattering approaches to electron transport in the kitaev chain. *arXiv-2101.06376*, 2021. <https://arxiv.org/abs/2101.06376>.
3. Gaëtan Cane, Junaid Majeed Bhat, Abhishek Dhar, and Cédric Bernardin. Localization effects due to a random magnetic field on heat transport in a harmonic chain. *Journal of Statistical Mechanics: Theory and Experiment*, 2021(11):113204, 2021. <https://iopscience.iop.org/article/10.1088/1742-5468/ac32b8>.
4. Junaid Majeed Bhat, Gaëtan Cane, Cédric Bernardin, and Abhishek Dhar. Heat transport in an ordered harmonic chain in presence of a uniform magnetic field. *Journal of Statistical Physics*, 186(1):1–15, 2022. <https://link.springer.com/article/10.1007/s10955-021-02848-5>.
5. Junaid Majeed Bhat, R. Shankar, and Abhishek Dhar. Quantized longitudinal conductance and edge states in an open geometry 2-dimensional chern insulator. *arXiv-2305.07640*, 2023. <https://doi.org/10.48550/arXiv.2305.07640>.

Other Publications

1. Saurav Pandey, Junaid Majeed Bhat, Abhishek Dhar, Sheldon Goldstein, David A. Huse, Manas Kulkarni, Anupam Kundu, and Joel L. Lebowitz. Boltzmann entropy of a freely expanding quantum ideal gas. *arXiv-2303.12330*, 2023. <https://arxiv.org/abs/2303.12330>.

ACKNOWLEDGEMENTS

My journey till the completion of my Ph.D. has been very smooth, *Alhamdulillah*. This has been primarily due to my ever-supporting family and numerous good people that I met along the way and shared time with. They have helped me grow as a physicist and as a human being.

From my personal life, I thank my family (*Faju, Neenu, Mummy, and Papa*) for their unwavering support, love, and encouragement. I also thank *Faizan*, a friend from a long time, for always helping me see the upside of things at low moments in life. I thank *Didi* and *Choti* for practically taking care of me during my early school days and *Chota-maamu* for teaching me elementary mathematics.

I have practically learned most of the physics I know through discussions with my friends from my master's and Ph.D. Particularly, I thank *Aritra, Farmaan, and Anuj* for enlightening discussions on fundamental aspects of different areas in physics. During my Ph.D., discussions with *Adhip, Basudeb*, and other friends at ICTS have been very helpful. I have had a great time working at ICTS and it was made more pleasant by amazing friends: *Divya, Basudeb, Jitendra, Tamoghna, Godwin, and Aditya Sharma*.

Last, but not least, I am grateful to *Abhishek* for his guidance. I couldn't have asked for a better supervisor!

List of Figures

1.1	Experimental results for the differential tunnelling conductance with the bias voltage, V , from experiments in Ref. [38, 39]. A peak could be seen developing at zero bias, $V = 0$, at strong enough magnetic fields.	4
2.1	Comparison of numerical time-evolution and analytical steady state results: Parameter values — $N = 2$, $N_b = 100$, $\mu_R = 1$, $\beta_R = 10$, $\mu_L = 0$, $\beta_L = 0$, $V_L = V_R = \eta_w = 1$, $\mu_w = 0$, $\eta_b = 1.5$ and $\Delta = 0.40$. (a) Comparison of the numerically calculated particle current at the left, $J_L(t)$, and the right, $J_R(t)$, end of the wire with the corresponding value, J_{th} , given by the expression in Eq. (2.39). (b) Comparison of the numerically calculated densities, $N_1(t) = \langle a_1^\dagger(t)a_1(t) \rangle$ and $N_2(t) = \langle a_2^\dagger(t)a_2(t) \rangle$, on the two sites of the wire with the corresponding value, N_{th} , given by the expression in Eq. (2.51). Similarly, (c) and (d) show the comparison of the energy current and the energy density from direct numerics with the values obtained from steady state expressions. Note that the left and the right heat currents have the same magnitude unlike the particle currents. The initial oscillations seen in the plots correspond to the transient phase, while the behaviour near $t = 60$ is due to the finite size of the baths. In the intermediate region we see perfect agreement between the numerical solution and the steady state value.	24

2.2	Spectrum of the entire system at parameter values $N = 2$, $N_b = 100$, $V^L = V^R = \eta_w = 1$, $\mu_w = 0$ and $\eta_b = 2.5$ for two values of Δ . In (a) we do not see any discrete energy level while in (b) a discrete energy level outside the main band can be seen. As discussed in the text, the non-existence of a steady state, indicated in a non-vanishing I_{ij} , is related to the existence of the discrete level which corresponds to a bound state (see Fig. (2.3)).	25
2.3	(a) The variation of $\sum_{ij} I_{ij} ^2$ over different parameters of the Hamiltonian in Eq. (2.64) with $\eta_s = V_L = V_R = 1$ and $N = 2$. Physically this quantity should identically vanish. We see that this happens only for certain parameter regimes of the Hamiltonian. In (b) we verify that the non-zero values are associated to the presence of high energy bound states in the spectrum of the full system seen in Fig. (2.2). This plot shows the gap between the bound state energy and the edge of the band, E_{bound} , for the same parameters as in (a). We see that the value of Δ at which the bound state appears is exactly the same value where the corresponding curves in (a) start taking non-zero values. (c) and (d) demonstrate that the numerical simulation for the two-point correlators agrees with the analytic results obtained by adding the bound state contributions to the steady-state values. While (c) shows that the commutation relations are satisfied when we add the bound state contribution (d) on the other hand depicts the persistent oscillations in the particle densities due to the bound states. Parameter values for these two plots are $N = 2$ for (c) and $N = 3$ for (d), $N_b = 100$, $\mu_R = 1$, $\beta_R = 10$, $\mu_L = 0$, $\beta_L = 0$, $V_L = V_R = \eta_w = 1$, $\mu_w = 0$, $\eta_b = 1$ and $\Delta = 0.80$	27
2.4	Variation of zero temperature conductance and the terms contributing to it with the left bath chemical potential, μ_L . Parameter values– $N = 100$, $V_L = V_R = 0.2$, $\eta_w = \mu_w = 1$, $\eta_b = 1$ and $\Delta = 0.25$	28

2.5	(a)Variation of thermal conductance at $\mu_L = 0$ in units of $\pi^2 k_B^2 T_L/6$ with the chemical potential, μ_w , on the wire for different wire sizes. (b) shows the wave function of the Majorana zero mode at μ_w far away and close to the topological phase transition point for $N = 100$. The extended nature of the Majorana wave functions spreading across the wire can be clearly seen when μ_w is close to the phase transition point. Other Parameter values– $V_L = V_R = 0.25$, $\eta_w = \eta_b = 1$ and $\Delta = 0.3$	29
2.6	(a) and (b) show the spectrum of an isolated next nearest neighbour Kitaev chain at the parameter values $\eta_1 = 1$, $\mu_w = -2$, $N = 100$, $V_L = V_R = 0.3$ and $\eta_b = 1.5$ at zero and non-zero values of θ and for the values of $\eta_2 = -1.5$, -0.5 and 1 corresponding to phase-2, phase-0 and phase-1 respectively. The topological edge modes can be seen in the spectral plots in between the superconducting gap. The corresponding conductance results obtained from Eq. 2.45 are shown in (c) and (d). The conductance plots for $\theta = 0$ show a single zero bias peak for the two topologically non-trivial phases while they show two distinct peaks for a non-zero θ value for phase-2.	32
3.1	Plot of the MBS wavefunction for different couplings with the reservoir at parameter values– $\eta_b = 1.5$, $\mu_w = 0.5$, $\Delta = 0.5$, $\eta_w = 1$. The normalization of these wavefunctions is the same as in Eq. (3.56-3.57) and the vertical black line marks the left end of the wire. Note that the lead wavefunctions are not visible on this scale.	48
4.1	Schematic of the SBHZ wire connected to metallic leads	64
4.2	(a) and (b) Bulk Spectrum and finite size ($N_x = N_y = 10$) spectrum, with free boundary conditions at the edges, of the BHZ model at different μ_w respectively. (c) is a contour plot of some of the edge states that appear of the finite size spectrum with $\mu_w = 1$ where the Chern number is known to be -1 . The energy values of the states are printed on the top of each sub-panel in (c).	66

4.3	Schematic of two geometries used for the calculation of the current density in the SBHZ wire and the reservoirs. The red regions are the reservoirs. The green region is the normal metallic region with a Hamiltonian identical to the reservoirs. The blue region is the SBHZ wire.	67
4.4	In (a) we show the variation of the conductance with the Fermi level, μ . (b) and (c) show the variation of the conductance at the Fermi level, $\mu = 0$, with η_c and N_y , respectively at $N_x = 100$. The inset in (b) shows that, on scaling η_c with $N_y^{1/2}$, the peaks in the oscillations coincide and therefore the period of the oscillations scales as $N_y^{1/2}\eta_c$. (d) shows the variation of the conductance at zero Fermi level with η_c at different N_x with $N_y = 100$. Parameter values; for (a) $N_x = N_y = N$, $\eta_b = 2$, $\mu_w = 1$, $\eta_c = 1.5$ and for (b), (c) and (d) $\eta_b = 2$ and $\mu_w = 1$	71
4.5	Excess charge density and current density inside the Chern insulator at the Fermi level, $\mu = 0$. Deep in the insulator (marked blue) the density has a value less than 10^{-8} . In (b) and (d), the size of the arrows indicate the current strength. Parameter values: $N_x = N_y = 20$ and $\eta_b = 1$, $\eta_c = 1$, $\mu_w = 1$.	73
4.6	Excess charge and current densities in the reservoirs and the SBHZ wire. Deep inside the insulator (white region), the density has a value less than 10^{-8} . The current in the reservoirs is localized along the lines at 45 degrees to the horizontal directions. Parameter Values–Size of the SBHZ wire (blue region)= 30×20 , $\Delta\mu_R = 0$, $\eta_b = \eta_c = 1$ and $\mu_w = 1$	74
4.7	A scattering state at zero energy in a 2D metallic strip with injection at the left bottom corner. The wavefunction is non-zero only on the green-marked sites, with the amplitudes indicated by A, B, C and their combinations. The red arrows indicate the currents. If the hopping from the 1D reservoir to the 2D metallic strip is set η_c , then a similar solution for the wavefunction could be constructed by making the replacement $(A + C) \rightarrow (A + C)/\eta_c$ inside the 1D reservoir and $B \rightarrow B/\eta_c$ inside the metallic strip.	75

4.8	Excess current density in the anisotropic reservoirs and the SBHZ wire. The anisotropy is introduced by choosing different hopping, denoted by η_{bx} and η_{by} , in the x and y directions respectively. The current in the reservoirs is localized along the lines at 45 degrees to the horizontal directions. Parameter Values—Size of the SBHZ wire (blue region)= 30×20 , $\Delta\mu_R = 0$, $\eta_{bx} = \eta_c = 1$, $\mu = 0$ and $\mu_w = 1$	76
5.1	Temperature distribution for the ordered chain. Parameter values — $e = m = k = 1$, $N = 32$, $T_L = 3.5$, $T_R = 1.5$	91
5.2	Spectrum of the chain in the bulk. Parameter values — $e = m = k = 1$	92
5.3	Comparison of the transmission $\mathcal{T}_N(\omega)$ for fixed and free boundary for $N = 20$ with $\mathcal{T}_\infty(\omega)$. Parameter values — $m = k = e = 1$, $\gamma = 0.2$ and $B = 2$	95
5.4	Variation of the current with the magnetic field. Parameter values — $e = m = k = 1$, $\gamma = 0.2$, $T_L = 1$, $T_R = 0$	95
5.5	Variation of the net transmission, in units of $k_B = 1$, with ω for uniform magnetic field, panel (a), and random magnetic field, panel (b). The axes are in log scale and $\gamma = 0.2$. The magnetic field in (a) is set to be 1 on all oscillators and in (b) it was chosen uniformly from the interval $(0, 2)$. As can be seen clearly from the plots, the localization effects cause suppression of the transmission.	99
5.6	Variation of numerically calculated Lyapunov exponent, $\lambda = \frac{1}{N} \langle \log u_N \rangle$, with ω . $\langle \log u_N \rangle$ denotes average of $\log u_N $ over 100 realizations of the random magnetic field. For (a), (b) and (c) the magnetic fields were chosen randomly from the intervals $(0, 1)$, $(-1, 1)$ and $(-1, 0)$ respectively. The solid line is the data from the simulation while the dashed line is a power law fit, $C\omega^s$, to the data with C and s as fitting parameters. The obtained values of the fitting parameters agree appreciably with the theoretical values.	103
5.7	Numerically obtained power laws for the average current, averaged over 100 realizations of the disorder, with fixed and free boundary conditions. For $\langle B \rangle > 0$, B_n is chosen from $(1, 3)$ while for $\langle B \rangle = 0$, B_n is chosen from $(-2, 2)$	105

5.8	Comparison for the transmission for disordered and uniform cases for the two boundary conditions. For $\langle B \rangle \neq 0$, B_n is chosen from $(1, 3)$ while for $\langle B \rangle = 0$, B_n is chosen from $(-1, 1)$. These are compared with the transmission for the uniform cases with $B_n = \langle B \rangle$ respectively.	107
5.9	Scaling of lowest allowed normal mode, ω_s^N with the system size, N . For $\langle B \rangle \neq 0$, B_n is chosen from $(1, 3)$ while for $\langle B \rangle = 0$, B_n is chosen from $(-1, 1)$. The $B = 0$ plot corresponds to the ordered chain (the ordered case $B \neq 0$ is not shown and has the scaling N^{-2}).	107

List of Tables

5.1	Comparison of numerical values of the current for finite N and the value of the current in the thermodynamic limit for $\gamma = 0.2$, $m = k = e = 1$, $T_L = 1$, $T_R = 0$.	94
5.2	Comparison of analytical prefactor for the three cases with the numerical prefactor. For this table, $N = 10^7$.	104
5.3	Power law for the current for different boundary conditions and average magnetic fields.	105

Contents

1	Introduction	1
2	QLE-NEGF formalism for a spinless superconducting wire	7
2.1	The model	8
2.2	Quantum Langevin equations and Green's function formalism	9
2.3	Nonequilibrium steady state properties	13
2.3.1	Steady state particle and energy currents	13
2.3.2	Two point correlations	17
2.4	An exact numerical approach for computing correlations in finite systems and the bound state contribution to the two point correlators	18
2.4.1	Bound states	21
2.5	Numerical verification of QLE-NEGF results and the bound state contributions in a nearest neighbour Kitaev chain	23
2.6	Next nearest neighbour Kitaev chain	30
2.7	Conclusion	32
3	Equivalence of Scattering and QLE-NEGF in 1-D Kitaev Chain	35
3.1	The model and the equivalence of the two approaches	36
3.2	Scattering approach	41
3.3	Analytical proof of the equivalence of QLE-NEGF and scattering approaches	49
3.4	Conclusion	57
4	Quantized two-terminal longitudinal conductance and edge states in an	

open geometry 2-dimensional Chern insulator	60
4.1 The model and the NEGF results for Conductance, charge and current density	62
4.1.1 The open system setup	62
4.1.2 Isolated SBHZ wire	64
4.1.3 NEGF results for the non-equilibrium steady state	65
4.2 Numerical results	70
4.2.1 Conductance	70
4.2.2 Charge and Current density	72
4.3 Conclusion	77
5 Classical harmonic wires in presence of a magnetic field	79
5.1 The model and derivation of heat current using NEGF	81
5.1.1 The model	81
5.1.2 Heat current using NEGF	82
5.1.3 Green's function as product of matrices	85
5.2 Expressions for the current in the thermodynamic limit for the uniform mag- netic field case	91
5.3 Disordered magnetic field	97
5.3.1 Effect of localization due to random magnetic field on the net Trans- mission	98
5.3.2 Analysis of the Lyapunov exponents	100
5.3.3 Size dependence of the current	104
5.4 Conclusion	108
6 Conclusions	110
7 Appendix	113
7.1 Derivation of the current expression	113
7.2 Derivation of the expressions for bound state contribution to the correlators .	115
7.3 Lyapunov exponent for a harmonic oscillator with parametric noise	119

Abstract

Topological phases of matter are exotic states that support dissipationless currents due to the presence of special modes localized at the edges of the sample. We look at the transport characteristics of models hosting such phases in open system geometries using the quantum Langevin and non-equilibrium Green's function formalism. Using this formalism, we first consider a general model of spinless superconducting wires in contact with thermal reservoirs and obtain closed-form exact expressions for particle current, energy current, and other two-point correlations in Landauer-type forms. The current expressions are found to be a sum of three terms having simple physical interpretations. As applications of our results, we explore the transport properties of two particular models: the 1D nearest neighbor Kitaev chain, and the 2D spinless-Bernevig-Hughes-Zhang (SBHZ) model. These are some of the simplest examples of 1D topological superconductors and 2D topological insulators, respectively. For the Kitaev chain, we present results on the particle and thermal conductance and also demonstrate analytically the physical interpretations of the three different terms in the current expression. For the SBHZ model, we look at the quantization of the two-terminal longitudinal conductance, and the current density supported by the edge modes inside the insulator as well as inside the reservoirs. We discuss the finite size effects on the quantization and also find that the current density is localized inside the insulator as well as inside the reservoirs. Moreover, we also find that the injection/ejection of the current into the insulator occurs only around its corners. We also consider the application of our results to the study of heat transport in a classical system, namely a harmonic chain of charged particles in the presence of a spatially uniform or random magnetic field. For the case of the uniform magnetic field, we show that heat transmission at low frequencies is strongly modified due to the presence and absence of the magnetic field, and for the case of the random magnetic field, we find that the low-frequency behavior of the localization length depends on the expectation value of the magnetic field. Due to these reasons, for the latter case, the scaling of the current also depends on the expectation value of the magnetic field.

Chapter 1

Introduction

Topological phases are exotic states of matter and an extensively studied area of condensed matter physics [1, 2]. These states of matter support special edge modes that carry dissipation-less current and are robust, to a certain degree, towards symmetry preserving disorder. The presence or absence of these modes is determined by a topological invariant, which is calculated from the bulk Hamiltonian of the model. This invariant depends on the dimensionality and the symmetries of the bulk Hamiltonian [3] — for example, in two dimensions a system with time reversal symmetry (TRS) is characterized by a Z_2 topological index taking values ± 1 while a system without TRS is characterized by a Chern number which can be any integer. The earliest known examples of topological phases are the quantum hall phases [4]. Currently, several models of topological phases are known to exist in different spatial dimensions, some of which have been experimentally realized as well. In one dimension, the simplest examples are the Su-Schrieffer-Heeger Model [5], which describes poly-acetylene, and the Kitaev chain [6]. While the former is a topological insulator, the latter is a topological superconductor. In two dimensions, several examples of topological insulators are known, some of which are the Haldane model [7], Bernevig, Hughes and Zhang model (BHZ) [8], and Kane-Mele model [9]. Some of these models have been realized in different experimental setups [10, 11]. Two dimensional (2D) topological superconductors were first discussed by Read and Green [12] and later on another model was proposed by

Sato [13].

The presence of the edge modes leads to quantized transport characteristics. The earliest known example of such a quantized transport coefficient is the quantized transverse conductivity in two-dimensional systems hosting quantum hall phases [4]. In the past decade, exciting transport characteristics of models hosting topological phases have been predicted which go beyond the quantized transverse conductivity. Some examples include zero-bias quantized peaks in 1D topological superconductors [14, 15, 16], quantized two-terminal conductance in topological insulators [17, 18, 19], quantized thermal Hall conductivity 3D time-reversal-invariant topological superconductors, [20, 21, 22, 23] etc. The first two of these examples have been observed experimentally [24, 25, 26, 27, 28, 11].

One of the standard approaches for understanding transport is the Green-Kubo formalism that is based on linear response theory. In the Green-Kubo approach, the system is assumed to be in an equilibrium state and an external field is introduced to perturb this state of the system. Under linear response approximation, one relates the transport coefficients to the equilibrium current-current correlations of the closed system. In fact, using this formalism the transverse conductivity can be shown to be proportional to the so-called Chern invariant [29]. However, experiments on transport are usually done in open system geometry, and more importantly, transport in topological systems is often in the ballistic regime, in which case the interactions of the system with the environment and the coupling of the system with the leads become important. For such systems, a microscopic model describing the bath and its interactions with the system becomes necessary. Then, various open quantum system approaches, for example, the Landauer approach, quantum Langevin equation-non-equilibrium Greens function (QLE-NEGF) approach [30], quantum Langevin equation approach [31], path-integral approach [32] and the quantum master equation approach, have to be used to study the transport properties. In this thesis, we discuss QLE-NEGF approach to transport in models hosting topological phases such as topological insulators (TI) and topological superconductors (TS). The NEGF formalism is a powerful method to study transport in mesoscopic systems connected to external reservoirs [33, 31, 15]. This method involves elimination of reservoir degrees of freedom to obtain the exact non-equilibrium

steady state (NESS) of the system in terms of the effective Green's function of the system. The effective Green's function of the wire is the Green's function of the isolated system, with self-energy contributions from the reservoirs. From the NESS, the transport properties, such as particle and heat currents, can be obtained and expressed in standard Landauer forms.

A wide variety of models hosting topological phases are given by tight-binding Hamiltonians with superconducting pairing, if present, defined on different lattices. Therefore, for a complete understanding of the transport properties of such exotic systems, we first consider a model of superconducting wires defined on a general lattice with arbitrary hopping and superconducting pairing. Using the NEGF formalism, we obtain an exact solution for this superconducting wire in contact with the reservoirs and from this solution we derive compact formulas for the particle current, heat current, and other two point correlators of the system. The expression for the heat and particle current is put in the Landauer form, from which the physical interpretations, in terms of the scattering processes, of different terms in the expressions was explicit. As an application of our formalism, we discuss transport characteristics of two particular models: the 1D Kitaev chain and the 2D spinless-Bernevig-Hughes-Zhang (SBHZ) model. These two are some of the simplest examples of a 1D topological superconductor and 2D topological insulator respectively.

The Kitaev chain models a one-dimensional spinless p-wave superconductor [6] and provides one of the simplest examples of a topological superconductor. This system has the so-called Majorana Bound States (MBS), which are topologically protected zero-energy bound states, localised at the boundaries of an open chain. Experimental realizations of this model and observe MBS is known to be very difficult. There are two main drawbacks: Firstly, the superconductor should be spinless which needs to be engineered as electrons in any material naturally carry spin, and the second drawback is the fact that p-wave superconductivity is needed which is extremely rare in nature. Nevertheless, several proposals were put forward [34, 35, 14, 36, 37] to realise the Kitaev chain experimentally and observe the MBS. Mainly, these proposals combine three independent phenomena to effectively model a p-wave spinless superconducting wire. These three phenomena are spin orbit coupling, time-reversal symmetry breaking and proximity induced superconductivity. The former two

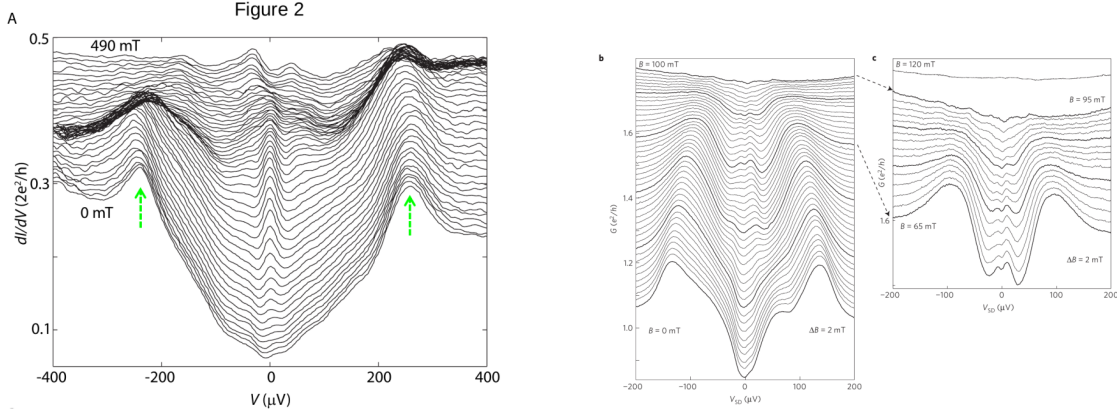


Figure 1.1: Experimental results for the differential tunnelling conductance with the bias voltage, V , from experiments in Ref. [38, 39]. A peak could be seen developing at zero bias, $V = 0$, at strong enough magnetic fields.

effectively create a spinless system and, in experimental setups, are provided by a semi-conducting nanowire, with strong spin orbit coupling, in presence of an applied external magnetic field. The latter is achieved by placing the semi-conducting wire in proximity of an s-wave superconductor. Some of these experimental proposals have already been successfully implemented [38, 39, 40, 41, 42, 43]. One of the key experimental signatures of the MBS is the zero-bias peak in the differential tunnelling conductance and Ref. [38, 39, 40] were some of first experiments which reported evidence for this peak. However, these experiments show several deviations from the expected theoretical results. For example, the strength of the zero-bias peak was found to be much smaller than the expected value $2e^2/h$, see Fig. 1. Apart from this, the disappearance of the peak should be accompanied by a gap closing and then reopening for the topological phase transition into the topologically trivial regime. As seen from Fig. 1, the peak disappears without the two adjoining peaks, due to the first excited states, closing in to mark the gap closing. Some of these issues have been resolved in very recent experiments [26, 27, 28]. However, it has also been argued that such zero bias peaks may be due to some trivial Andreev bound states. These trivial bound-states could form in presence of smooth or disordered chemical potential variations [44, 45, 46]. Therefore, while Ref. [26, 27, 28] show an encouraging progress, realization of MBS in an experimental setup beyond any doubt is still an unachieved task. It may be possible to distinguish the trivial Andreev bound state from the MBS by looking at other transport characteristics such as

the thermal conductance. It is therefore important to have a full understanding of transport characteristics of the Kitaev chain in such geometries and the QLE-NEGF formalism provides a simple and straightforward way to do so.

We next consider a simple 2D topological insulator in contact with metallic leads (reservoirs) on each ends. The existence of perfectly conducting edge modes suggests quantization of longitudinal conductance. However, this is not obvious when one considers that the contacts with the leads need not be perfect and there could be scattering of incident electron waves. In fact, to the best of our knowledge, there exists no proof (similar to TKNN) [29] of the quantization of the longitudinal conductance in the open system setup. We attempt to arrive at a better understanding of the two-terminal longitudinal conductance in the open system by use of the NEGF formalism. For our studies, we consider the spinless BHZ (SBHZ) model [47], a Chern insulator, placed in contact with two normal metallic leads. Apart from measuring the conductance obtained from NEGF, we use this formalism to also extract information on the scattering states formed by the edge modes *in the presence of the leads*.

We also discuss application of NEGF method to heat transport in ordered and disordered classical harmonic wires in the presence of a magnetic field. Low dimensional harmonic systems are known to have anomalous heat transport properties [31], and recent works on heat transfer in such systems in presence of magnetic field have led to some interesting results [48, 49, 50]. In particular, Ref. [48] studied a harmonic chain with transverse degrees of freedom and with the Hamiltonian dynamics perturbed by stochastic noise that conserves both momentum and energy. The stochastic noise is used to model the non-linearities of the interactions [51]. In the context of anomalous heat transport the authors identify a new universality class based on the system size dependence of the thermal conductivity. An interesting observation made in the paper is on the phonon dispersion in this model with a finite magnetic field — out of the two phonon bands it was found that the lower band has a low frequency dispersion $\omega \sim q^2$ and so a vanishing sound speed. A natural question is the effect of this on heat conduction in this system in the absence of stochastic noise. In the absence of the stochastic noise, this systems admits the same structure of the Green's function as the 1D Kitaev chain, we therefore use the same formalism to address the question

of heat conduction in this system in absence of stochastic noise. The effect of magnetic field on acoustic phonon modes have also been considered experimentally [52].

Outline: This thesis is structured as follows:

In chapter 2, we define a general model of superconducting wires which covers some models of topological insulators and superconductors. We evaluate explicit expressions for particle, heat conductance and other two point correlators of the system. We also discuss effects of high energy bound states, if present in the system, and find their explicit contribution to the non-equilibrium steady state of the system. We numerically verify the steady state results for the 1D Kitaev chain and discuss its transport properties. We also apply our results to study conductance of next-to-nearest Kitaev chain.

In chapter 3, we study transport in the 1D Kitaev chain using scattering method and analytically demonstrate its equivalence with the QLE-NEGF results derived in chapter 2. We also discuss the Majorana bound state in the open system geometry while deriving the conductance properties using the scattering approach.

In chapter 4, we study transport due to edge modes in a simple 2D topological insulator (SBHZ Model) in an open system geometry. We consider the quantization of the two terminal longitudinal conductance and the effects of finite system size on it. We also discuss the current density and the charge density inside the insulator as well as in the reservoirs due to the scattering states formed by the edge modes.

In chapter 5, we apply our formalism to a classical system of a 1D harmonic wire in presence of ordered and disordered magnetic fields. This system admits the same structure of the Green's function and therefore, using the formalism developed in Chapter 2 we study heat transport in this system. For the ordered case, we discuss the heat conduction in the thermodynamic limit and for the disordered case we look at the scaling of the disorder averaged current with the system size

In chapter 6, we summarize the results of this thesis.

Chapter 2

QLE-NEGF formalism for a spinless superconducting wire

In this chapter, we introduce a formalism to compute steady state properties of a general model of a spinless superconducting wire. The model we consider here is quite general in the sense that we allow non-zero hopping elements between arbitrary sites and similarly the superconducting pairing term is allowed between any pair of sites. Thus there are no restrictions on dimensionality and the structure of the underlying lattice and the range of the interactions. As an application of this formalism, we would consider the transport properties of 1D nearest neighbour Kitaev Chain and next-to-nearest neighbour Kitaev chain.

In the next section, we introduce the model and in Sec. 2.2, we derive the quantum Langevin equations for the model which we solve to obtain the exact steady state solution in terms of the nonequilibrium Green's functions. In Sec. 2.3, we derive compact expressions for particle, heat currents and the two point correlators for the steady state. We express the particle and heat current in a form from which the physical interpretations of different terms contributing to the transport are explicit. In Sec. 2.4, we introduce a numerical scheme to for computing correlations of the system, which we use to express the bound state contributions to the two point correlators in the nonequilibrium steady state. In Sec. 2.5, we use the numerical scheme in to explicitly verify the results derived in this chapter for the case of 1-D Kitaev

chain where we also discuss its transport properties. In Sec. 2.6, we discuss conductance of next to nearest neighbor Kitaev chain. We summarize our results in Sec. 2.7

2.1 The model

We consider a wire coupled to thermal baths on its two ends. The wire Hamiltonian, \mathcal{H}^W , is taken to correspond to a spinless superconductor while the two baths are modelled by the tight binding Hamiltonians, \mathcal{H}^L and \mathcal{H}^R . The L and R superscripts denote the baths on the left and the right of the wire respectively. The couplings of the wire with the two baths, \mathcal{H}^{WR} and \mathcal{H}^{WL} , are also modelled by tight binding Hamiltonians. Let us denote by $\{c_m, c_m^\dagger\}$, $\{c_\nu, c_\nu^\dagger\}$ and $\{c_{\nu'}, c_{\nu'}^\dagger\}$ the annihilation and creation operators of the system, left bath and the right bath respectively. These satisfy usual fermionic anti-commutation relations. For lattice sites on the bath we use the Latin indices, i, j, \dots , for sites on the left reservoir we use the Greek indices, α, ν, \dots , and for sites on the right reservoir, the primed Greek letters α', ν', \dots . We take the Hamiltonian of the full system of wire and baths as follows:

$$\mathcal{H} = \mathcal{H}^W + \mathcal{H}^{WL} + \mathcal{H}^{WR} + \mathcal{H}^L + \mathcal{H}^R, \quad (2.1)$$

where

$$\mathcal{H}^W = \sum_{mn} H_{mn}^W c_m^\dagger c_n + \Delta_{mn} c_m^\dagger c_n^\dagger + \Delta_{mn}^\dagger c_m c_n, \quad (2.2)$$

$$\mathcal{H}^{WL} = \sum_{\nu m} V_{m\nu}^L c_m^\dagger c_\nu + V_{\nu m}^{L\dagger} c_\nu^\dagger c_m, \quad (2.3)$$

$$\mathcal{H}^{WR} = \sum_{\nu' m} V_{m\nu'}^R c_m^\dagger c_{\nu'} + V_{\nu' m}^{R\dagger} c_{\nu'}^\dagger c_m, \quad (2.4)$$

$$\mathcal{H}^L = \sum_{\mu\nu} H_{\mu\nu}^L c_\mu^\dagger c_\nu \quad (2.5)$$

$$\mathcal{H}^R = \sum_{\mu'\nu'} H_{\mu'\nu'}^R c_{\mu'}^\dagger c_{\nu'}. \quad (2.6)$$

2.2 Quantum Langevin equations and Green's function formalism

We now follow the approach of Ref. [33] to obtain the NEGF-type results for this system. First we note that the Heisenberg equations of motion for the wire sites and bath sites are given by:

$$\dot{c}_l = -i \sum_m H_{lm}^W c_m - i \sum_m K_{lm} c_m^\dagger - i \sum_\alpha V_{l\alpha}^L c_\alpha - i \sum_{\alpha'} V_{l\alpha'}^R c_{\alpha'}, \quad (2.7)$$

$$\dot{c}_\alpha = -i \sum_\nu H_{\alpha\nu}^L c_\nu - i \sum_l V_{\alpha l}^{L\dagger} c_l, \quad (2.8)$$

$$\dot{c}_{\alpha'} = -i \sum_{\nu'} H_{\alpha'\nu'}^R c_{\nu'} - i \sum_l V_{\alpha' l}^{R\dagger} c_l, \quad (2.9)$$

where $K_{lm} = (\Delta - \Delta^T)_{lm}$. We treat the term containing c_l in Eq. (2.8) and Eq. (2.9) as the inhomogeneous parts and solve these equations using the following Green's functions corresponding to the homogeneous part of the equations:

$$g_L^+(t) = -ie^{-itH^L} \theta(t) = \int_{-\infty}^{\infty} \frac{d\omega}{2\pi} g_L^+(\omega) e^{-i\omega t}, \quad (2.10)$$

$$g_R^+(t) = -ie^{-itH^R} \theta(t) = \int_{-\infty}^{\infty} \frac{d\omega}{2\pi} g_R^+(\omega) e^{-i\omega t}. \quad (2.11)$$

In terms of these, we obtain the following solutions for the reservoir equations (for $t > t_0$):

$$c_\alpha(t) = i \sum_\nu [g_L^+(t-t_0)]_{\alpha\nu} c_\nu(t_0) + \int_{t_0}^t ds \sum_{\nu l} [g_L^+(t-s)]_{\alpha\nu} V_{\nu l}^{L\dagger} c_l(s), \quad (2.12)$$

$$c_{\alpha'}(t) = i \sum_{\nu'} [g_R^+(t-t_0)]_{\alpha'\nu'} c_{\nu'}(t_0) + \int_{t_0}^t ds \sum_{\nu' l} [g_R^+(t-s)]_{\alpha'\nu'} V_{\nu' l}^{R\dagger} c_l(s). \quad (2.13)$$

Substituting these results in the Heisenberg equation for the wire sites we have:

$$\begin{aligned} \dot{c}_l = & -i \sum_m H_{lm}^W c_m - i \sum_m K_{lm} c_m^\dagger - i\eta_l^L - i\eta_l^R \\ & - i \int_{t_0}^t ds \sum_{\alpha\nu m} V_{l\alpha}^L [g_L^+(t-s)]_{\alpha\nu} V_{\nu m}^{L\dagger} c_m(s) - i \int_{t_0}^t ds \sum_{\alpha'\nu'm} V_{l\alpha'}^R [g_R^+(t-s)]_{\alpha'\nu'} V_{\nu'm}^{R\dagger} c_m(s), \end{aligned} \quad (2.14)$$

where

$$\eta_l^L = i \sum_{\alpha\nu} V_{l\alpha}^L [g_L^+(t-t_0)]_{\alpha\nu} c_\nu(t_0), \quad (2.15)$$

$$\eta_l^R = i \sum_{\alpha'\nu'} V_{l\alpha'}^R [g_R^+(t-t_0)]_{\alpha'\nu'} c_{\nu'}(t_0). \quad (2.16)$$

At $t = t_0$, we choose the two reservoirs to be described by grand canonical ensembles at temperatures and chemical potentials given by (T_L, μ_L) and (T_R, μ_R) respectively. This allows us to determine the correlation properties of the terms η_l^L and η_l^R . For the left bath we have:

$$\langle \eta_l^L(t) \eta_m^L(t') \rangle = \langle \eta_l^{L\dagger}(t) \eta_m^{L\dagger}(t') \rangle = 0, \quad (2.17)$$

$$\langle \eta_l^{L\dagger}(t) \eta_m^L(t') \rangle = \sum_{\alpha\mu\nu\sigma} V_{l\alpha}^{L*} [g_L^{+\dagger}(t-t_0)]_{\alpha\nu} V_{m\mu}^L [g_L^+(t'-t_0)]_{\mu\sigma} \langle c_\nu^\dagger(t_0) c_\sigma(t_0) \rangle, \quad (2.18)$$

with similar expressions for η_l^R . We thus see that Eq. (2.14) has the structure of a quantum Langevin equation for the wire where the reservoir contributions are split into noise (terms given by η_l^L and η_l^R), and dissipation (the terms in Eq. (2.14) involving integral kernels).

At this point we take a digression to simplify Eq. (2.18) and write it in Fourier space. Let $\psi_q^L(\alpha)$ and λ_q^L be the single-particle eigenvectors and eigenvalues of the left reservoir Hamiltonian, \mathcal{H}^L . Using this and the fact that the left bath is initially described by a grand

canonical ensemble with temperature T_L and chemical potential μ_L we get

$$[g_L^\dagger(t-t_0)]_{\nu\sigma} = -i\theta(t-t_0) \sum_q \psi_q^L(\nu) \psi_q^{L*}(\sigma) e^{-i\lambda_q^L(t-t_0)}, \quad (2.19)$$

$$\langle c_\nu^\dagger(t_0) c_\sigma(t_0) \rangle = \sum_q \psi_q^{L*}(\nu) \psi_q^L(\sigma) f_L(\lambda_q^L), \quad (2.20)$$

where $f_L(\lambda_q^L) = f(\lambda_q^L, \mu_L, T_L)$ is the Fermi-Dirac distribution function. Using these two equations in Eq. (2.18) we have:

$$\langle \eta_l^{L\dagger}(t) \eta_m^L(t') \rangle = \sum_{\alpha\nu} V_{l\alpha}^{L*} \left(\sum_q \psi_q^{L*}(\alpha) \psi_q^L(\nu) e^{i\lambda_q^L(t-t')} f_L(\lambda_q^L) \right) V_{\nu m}^{LT}. \quad (2.21)$$

Defining the Fourier transform

$$\tilde{\eta}_l(\omega) = \int_{-\infty}^{\infty} \frac{dt}{2\pi} \eta_l(t) e^{i\omega t}, \quad (2.22)$$

we finally get the Fourier transform form of Eq. (2.21) as:

$$\langle \tilde{\eta}_l^{L\dagger}(\omega) \tilde{\eta}_m^L(\omega') \rangle = \Gamma_{ml}^L(\omega) f_L(\omega) \delta(\omega - \omega'), \quad (2.23)$$

where $\Gamma_{ml}^L(\omega) = (V^L \rho^L V^{L\dagger})_{ml}$ and $\rho_{\alpha\nu}^L = \sum_q \psi_q^L(\alpha) \psi_q^{L*}(\nu) \delta(\omega - \lambda_q^L)$. Using Eq. (2.23) we can also show that

$$\langle \tilde{\eta}_l^L(\omega) \tilde{\eta}_m^{L\dagger}(\omega') \rangle = \Gamma_{lm}^L(\omega) [1 - f_L(\omega)] \delta(\omega - \omega'). \quad (2.24)$$

The correlation properties of the right bath would be of the same form.

Let us now return back to Eq. (2.14) and obtain its steady state solution. For this we assume that one has taken the limits of infinite bath degrees of freedom and the time $t_0 \rightarrow -\infty$. Then it is expected that a steady state should exist provided certain conditions are satisfied [33]. For now we assume the existence of a steady state and will re-visit this question in the next section. The Langevin equation in Eq. (2.14) is then amenable to a solution by Fourier

transforms. To this end, we define

$$\tilde{c}_l(\omega) = \int_{-\infty}^{\infty} \frac{dt}{2\pi} c_l(t) e^{i\omega t}, \quad (2.25)$$

and substitute this in Eq. (2.14) to get

$$[\Pi(\omega)]_{lm} \tilde{c}_m(\omega) - K_{lm} \tilde{c}_m^\dagger(-\omega) = \tilde{\eta}_l^L(\omega) + \tilde{\eta}_l^R(\omega), \quad (2.26)$$

where

$$\Pi(\omega) = \omega - H^W - \Sigma_L^+(\omega) - \Sigma_R^+(\omega), \quad (2.27)$$

$$\Sigma_L^+(\omega) = V^L g_L^+(\omega) V^{L\dagger}, \quad \Sigma_R^+(\omega) = V^R g_R^+(\omega) V^{R\dagger}. \quad (2.28)$$

With some algebra one can also show:

$$\Gamma_L(\omega) = \frac{1}{2\pi i} [\Sigma_L^-(\omega) - \Sigma_L^+(\omega)], \quad (2.29)$$

$$\Gamma_R(\omega) = \frac{1}{2\pi i} [\Sigma_R^-(\omega) - \Sigma_R^+(\omega)], \quad (2.30)$$

where $\Sigma_L^- = [\Sigma_L^+]^\dagger$ and $\Sigma_R^- = [\Sigma_R^+]^\dagger$. We now write Eq. (2.26) in matrix form as:

$$\Pi(\omega) \tilde{C}(\omega) - K \tilde{C}^\dagger(-\omega) = \tilde{\eta}^L(\omega) + \tilde{\eta}^R(\omega), \quad (2.31)$$

where $\tilde{C}(\omega)$, $\tilde{C}^\dagger(\omega)$ and $\tilde{\eta}^{L/R}(\omega)$ are column matrices with components $\tilde{c}_m(\omega)$, $\tilde{c}_m^\dagger(\omega)$ and $\tilde{\eta}_l^{L/R}(\omega)$ respectively. A complex conjugation of Eq. (2.26) and transforming $\omega \rightarrow -\omega$ gives us the following matrix equation:

$$\Pi^*(-\omega) \tilde{C}^\dagger(-\omega) - K^* \tilde{C}(\omega) = \eta^{L\dagger}(-\omega) + \eta^{R\dagger}(-\omega) \quad (2.32)$$

Using Eq. (2.32) and Eq. (2.31) we finally obtain the following expression for $\tilde{c}_m(\omega)$:

$$\tilde{c}_m(\omega) = [G_1^+(\omega)]_{ml} [\tilde{\eta}_l^L(\omega) + \tilde{\eta}_l^R(\omega)] + [G_2^+(\omega)]_{ml} [\tilde{\eta}_l^{L\dagger}(-\omega) + \tilde{\eta}_l^{R\dagger}(-\omega)], \quad (2.33)$$

where

$$G_1^+(\omega) = \frac{1}{\Pi(\omega) + K[\Pi^*(-\omega)]^{-1}K^\dagger}, \quad (2.34)$$

$$G_2^+(\omega) = G_1^+(\omega)K[\Pi^*(-\omega)]^{-1}. \quad (2.35)$$

Thus we have obtained the steady state solution in terms of these two nonequilibrium Green's functions.

2.3 Nonequilibrium steady state properties

Using the solution for $\tilde{c}_m(\omega)$ and the noise properties obtained in the previous section, we now proceed to compute expectation values of various physical observables which are along quadratic functions of the fermionic operators.

2.3.1 Steady state particle and energy currents

We first define the particle current in the wire. Clearly, the rate of change of total number of particles in the left bath, $N_L = \sum_\alpha c_\alpha^\dagger c_\alpha$, gives the particle current, J_L , entering the wire from the left reservoir. A straightforward calculation then gives

$$J_L = 2 \sum_{m\alpha} \text{Im}[V_{m\alpha}^L \langle c_m^\dagger(t)c_\alpha(t) \rangle] \quad (2.36)$$

$$= 2 \text{Im} \left[\sum_m \int_{-\infty}^{\infty} \int_{-\infty}^{\infty} d\omega d\omega' e^{i(\omega-\omega')t} \left\langle c_m^\dagger(\omega) \sum_\alpha V_{m\alpha}^L c_\alpha(\omega') \right\rangle \right] \quad (2.37)$$

From the Fourier transform of Eq. (2.8) we have

$$\sum_\alpha V_{m\alpha}^L \tilde{c}_\alpha(\omega') = \eta_m^L(\omega') + [\Sigma_L^+(\omega')]_{ml} \tilde{c}_l(\omega'). \quad (2.38)$$

Using Eqs. (2.29,2.30,2.33) and the correlation properties of the noise terms we finally obtain the following expression for current in the units where $e = h = 1$:

$$J_L = \int_{-\infty}^{\infty} d\omega \left(T_1(\omega)(f_L^e(\omega) - f_R^e(\omega)) + T_2(\omega)(f_L^e(\omega) - f_R^h(\omega)) + T_3(\omega)(f_L^e(\omega) - f_L^h(\omega)) \right),$$

where $G_1^-(\omega) = [G_1^+(\omega)]^\dagger$, $G_2^-(\omega) = [G_2^+(\omega)]^\dagger$ and

$$T_1(\omega) = 4\pi^2 \text{Tr} [G_1^+(\omega)\Gamma_R(\omega)G_1^-(\omega)\Gamma_L(\omega)], \quad (2.39)$$

$$T_2(\omega) = 4\pi^2 \text{Tr} [G_2^+(\omega)\Gamma_R^T(-\omega)G_2^-(\omega)\Gamma_L(\omega)] \text{ and} \quad (2.40)$$

$$T_3(\omega) = 4\pi^2 \text{Tr} [G_2^+(\omega)\Gamma_L^T(-\omega)G_2^-(\omega)\Gamma_L(\omega)]. \quad (2.41)$$

We have introduced electron and hole occupation numbers as $f_x^e(\omega) = f(\omega, \mu_x, T_x)$ and $f_x^h(\omega) = f(\omega, -\mu_x, T_x)$, ($x = L, R$). The details of the calculation are presented in the appendix 7.1. A similar expression can be obtained for J_R which we define as the current from the right reservoir into the system.

For $\Delta = 0$ case, it is straightforward to see that Eq. (2.39) agrees with the expression for the current obtained in Ref. [33]. Also, for $\mu_L = -\mu_R = \mu$ and $T_L = T_R = T$ it reduces to

$$J_L = \int_{-\infty}^{\infty} d\omega [T_1(\omega) + T_3(\omega)](f^e(\omega) - f^h(\omega)),$$

This form agrees with the current expression derived in Ref. [15] for a 1-D Kitaev chain with nearest neighbour interactions.

From Eq. (2.39) we see that for $T_L = T_R, \mu_L = \mu_R$, $J_L, J_R \neq 0$ whenever $\Delta \neq 0$ and, in general, the current at the left end and the right end are different, *i.e.* $J_L \neq -J_R$. This result initially appears to be surprising, but is basically due to the fact that the superconducting pairing matrix Δ_{lm} in the Kitaev wire is not calculated self-consistently but is taken as a fixed parameter of the wire Hamiltonian. This becomes clear if we consider the equation for

the total number operator of the wire:

$$\frac{d}{dt} \left(\sum_l \langle c_l^\dagger(t) c_l(t) \rangle \right) = J_S + J_L + J_R, \quad (2.42)$$

where $J_S = \sum_{l,m} 2 \text{Im} \{ K_{lm} \langle c_l^\dagger c_m^\dagger \rangle \}$ is the extra contribution from the superconducting terms of the wire Hamiltonian. In the steady state the left hand side vanishes and the fact that $J_L + J_R \neq 0$ can be understood in terms of the extra pairing current J_S . Physically our set-up corresponds to a wire that is in contact with a superconducting wire and the so-called proximity effect induces superconductivity in the wire. The superconducting substrate acts as an electron reservoir [53, 54, 55] and acts like a ground for the wire. Thus current can enter the wire through the left and right reservoirs and flow into the superconductor. Also, J_S need not vanish even when the baths are initially at the same chemical potentials and temperatures and hence, J_L and J_R may take non-zero values. Note that imposing the self-consistency condition, namely

$$K_{lm} = \langle c_m c_l \rangle = \langle c_l^\dagger c_m^\dagger \rangle^*, \quad (2.43)$$

for all l, m , would give $J_S = 0$ and in that case we would get the expected charge conservation condition $J_L = -J_R$.

We comment on the physical interpretation of the three different parts in Eq. (2.39): the first term corresponds to normal electrons being transmitted from the left to the right bath (normal transmission), the second term corresponds to the process of an electron from the left bath being scattered as a hole into the right bath (Andreev transmission) while the third term corresponds to the electron from the left bath scattered back as a hole into the left bath again (Andreev reflection). The probability of these three processes are then given respectively by $T_1(\omega)$, $T_2(\omega)$ and $T_3(\omega)$. Defining the conductance at the left end (in units of e^2/h) by

$$G_L(T_L, \mu_L) = \frac{\partial J_L}{\partial \mu_L}, \quad (2.44)$$

we get at zero temperature ($T_L = T_R = 0$):

$$G_L = T_1(\mu_L) + T_2(\mu_L) + T_3(\mu_L) + T_3(-\mu_L). \quad (2.45)$$

Due to the particle-hole symmetry of the Hamiltonian, we expect $T_2(\omega)$ and $T_3(\omega)$ to be even functions of ω . Therefore, $T_3(\omega)$ contributes twice to the conductance which represents the fact that in Andreev reflection, a total of two electrons are transferred across the junction as a single cooper pair.

We now turn to the computation of the energy current, which is readily obtained using our formalism. The energy current coming into the wire from the left end can be obtained by the rate of change of left bath Hamiltonian, \mathcal{H}_L . So, we consider $\frac{d}{dt} \langle \mathcal{H}^L \rangle$ and then use the Heisenberg equations of motion for the left reservoirs operators to obtain:

$$J_L^H = -\frac{d}{dt} \langle \mathcal{H}^L \rangle = 2 \sum_{l\nu} \text{Im} \left\{ [V^L H^L]_{l\nu} \langle c_l^\dagger c_\nu \rangle \right\}, \quad (2.46)$$

where J_L^H is the energy current flowing into the wire. This can be simplified by using Eq. 2.8 to obtain,

$$J_L^H = -2 \text{Im} \left[\sum_m \int_{-\infty}^{\infty} \int_{-\infty}^{\infty} d\omega d\omega' e^{i(\omega-\omega')t} \omega' \left\langle c_m^\dagger(\omega) \sum_\alpha V_{m\alpha}^L c_\alpha(\omega') \right\rangle \right]. \quad (2.47)$$

Comparing this with the expression for particle current in Eq. (2.37), it can be seen that this would yield the same expression with an extra factor of ω in the integral. After some simplification this then gives:

$$J_L^H = \int_{-\infty}^{\infty} d\omega \omega [T_1(\omega) + T_2(\omega)] (f_L^e(\omega) - f_R^e(\omega)). \quad (2.48)$$

The low temperature thermal conductance is given by

$$G_L^H = \frac{dJ_L^H}{dT_L} = \frac{k_B^2 \pi^2 T_L}{6} G_T(\mu_L), \quad (2.49)$$

where, $G_T(\mu_L) = 2(T_1(\mu_L) + T_2(\mu_L))$ and is of similar form as obtained in Ref. [56]. Therefore, only two processes contribute to the heat current the normal transmission and the Andreev transmission. The Andreev reflection term does not contribute to the energy current since the particle and hole each carry a unit of energy and so no net energy is transferred across the junction. Note also that, unlike the electron current, the energy current is the same at both ends of the wire and indeed anywhere inside the wire since energy is conserved.

The general expressions for particle current and energy current in Eqs. (2.39,2.48) are two of our main results. These expressions provide compact formulas for thermal and particle conductances and may be used to study these physical quantities in systems defined on arbitrary lattices with interactions between arbitrary sites.

2.3.2 Two point correlations

We now compute the full two-point correlation matrices $\langle c_l^\dagger c_m \rangle$, $\langle c_l c_m \rangle$, $\langle c_l^\dagger c_m^\dagger \rangle$ in the NESS. These would allow one to obtain the local particle densities, $\langle c_l^\dagger c_l \rangle$, and local currents (normal and superconducting) anywhere in the system. We start by writing the steady state correlations in the Fourier representation:

$$N_{lm}^{SS} = \langle c_m^\dagger(t) c_n(t) \rangle = \int \int d\omega d\omega' e^{i(\omega' - \omega)t} \langle c_m^\dagger(\omega) c_n(\omega') \rangle. \quad (2.50)$$

Then using the solution in Eq. (2.33) and the noise properties a straightforward computation gives:

$$N_{lm}^{SS} = \sum_{x=L,R} \int d\omega \left[[G_1^+(\omega) \Gamma_x(\omega) G_1^-(\omega)]_{nm} f_x^e(\omega) + [G_2^+(\omega) \Gamma_x^T(-\omega) G_2^-(\omega)]_{nm} f_x^h(\omega) \right]. \quad (2.51)$$

A similar computation gives

$$\begin{aligned} M_{lm}^{SS} &= \langle c_i(t) c_j(t) \rangle \\ &= \sum_{x=L,R} \int d\omega [Q_x(\omega)]_{ij} + [Q_x^T(\omega) - Q_x(\omega)]_{ij} f_x(\omega), \end{aligned} \quad (2.52)$$

where $Q_{L/R}(\omega) = G_1^+(\omega)\Gamma_{L/R}(\omega)G_2^{+T}(-\omega)$. Substituting this in the expression for $J_S = \sum_{l,m} 2 \text{Im}\{K_{lm}\langle c_l^\dagger c_m^\dagger \rangle\}$, we get its steady state value,

$$J_S = 2 \int d\omega \text{Im}\left\{\text{Tr}\left[Q_L^\dagger(\omega)K\right]\right\}(2f_L(\omega) - 1) + \text{Im}\left\{\text{Tr}\left[Q_R^\dagger(\omega)K\right]\right\}(2f_R(\omega) - 1)$$

From Eq. (2.52), it also follows that $\langle\{c_i(t), c_j(t)\}\rangle = \int d\omega[Q_L(\omega) + Q_L^T(\omega) + Q_R(\omega) + Q_R^T(\omega)]_{ij} = I_{ij}$. It turns out that these integrals do not always vanish. This is at first surprising since we expect that the usual anti-commutation properties of the fermionic operators should hold. The underlying reason is that the results presented so far assume the existence of a steady state. However this is true only if there are no bound states in the system (wire+baths). In case there are bound states present in the system, then their contributions to the expressions of the correlations have to be added separately. For the case of Eq. (2.52), the contribution from the bound state would ensure the vanishing of $\langle\{c_i(t), c_j(t)\}\rangle$. To calculate the contributions of the bound states requires one to use an approach involving the diagonalization of the full Hamiltonian of the two baths and wire and identification of the bound states. We describe this in the next section where we present the contributions of the bound states to the correlations. We relegate the details of the calculation to an appendix 7.2. In Sec. 2.5, we will demonstrate numerically that these contributions ensure that the commutation relations hold and also show their effect on the density correlations.

2.4 An exact numerical approach for computing correlations in finite systems and the bound state contribution to the two point correlators

The fact that our system is described by a quadratic Hamiltonian means that the exact diagonalization of the system becomes a much simpler problem [57, 58]. Let N_S be the total number of lattice sites in the entire system of wire and the two reservoirs. Then instead of diagonalizing a $2^{N_S} \times 2^{N_S}$ matrix, the problem reduces to the diagonalization of a $2N_S \times 2N_S$

matrix. To see this we define a $2N_S$ -component column vector:

$$\chi = \begin{pmatrix} C \\ C^\dagger \end{pmatrix}, \text{ where } C = \begin{pmatrix} C_W \\ C_L \\ C_R \end{pmatrix}, \quad (2.53)$$

and C_W , C_L and C_R are column vectors containing the wire, left bath and the right bath operators respectively. Note that $\chi_{N_S+i}^\dagger = \chi_i$, for $i = 1, 2, \dots, N_S$. We can then write the Hamiltonian in Eq. (2.1) in the form

$$\mathcal{H} = \frac{1}{2}\chi^\dagger \mathcal{Z} \chi + \frac{1}{2} \text{Tr}[H_S], \quad (2.54)$$

where \mathcal{Z} is a $2N_S \times 2N_S$ matrix defined as

$$\mathcal{Z} = \begin{pmatrix} H_S & K_S \\ K_S^\dagger & -H_S^* \end{pmatrix}, \quad (2.55)$$

with

$$H_S = \begin{pmatrix} H_W & V_L & V_R \\ V_L^\dagger & H_L & 0 \\ V_R^\dagger & 0 & H_R \end{pmatrix} \text{ and } K_S = \begin{pmatrix} K & 0 & 0 \\ 0 & 0 & 0 \\ 0 & 0 & 0 \end{pmatrix}. \quad (2.56)$$

As can be easily verified, the $2N_S$ eigenvectors of the matrix \mathcal{Z} occur in pairs of the form

$$\psi_i = \begin{pmatrix} u_1(\epsilon_i) \\ u_2(\epsilon_i) \\ \cdot \\ \cdot \\ u_{N_S}(\epsilon_i) \\ v_1(\epsilon_i) \\ \cdot \\ \cdot \\ v_{N_S}(\epsilon_i) \end{pmatrix} \quad \phi_i = \begin{pmatrix} v_1^*(\epsilon_i) \\ v_2^*(\epsilon_i) \\ \cdot \\ \cdot \\ v_{N_S}^*(\epsilon_i) \\ u_1^*(\epsilon_i) \\ \cdot \\ \cdot \\ u_{N_S}^*(\epsilon_i) \end{pmatrix}, \quad i = 1, 2, \dots, N_S, \quad (2.57)$$

where the eigenvectors ψ_i and ϕ_i correspond respectively to eigenvalues ϵ_i and $-\epsilon_i$. Let us define the $N_S \times N_S$ matrices U , V and E with matrix elements $U_{si} = u_s(\epsilon_i)$, $V_{si} = v_s(\epsilon_i)$ and $E_{ij} = \epsilon_i \delta_{ij}$, respectively. Then we see that the matrix W which diagonalizes \mathcal{Z} has the structure

$$W = \begin{pmatrix} U & V^* \\ V & U^* \end{pmatrix}, \quad (2.58)$$

so that

$$W^\dagger \mathcal{Z} W = \begin{pmatrix} E & 0 \\ 0 & -E \end{pmatrix}. \quad (2.59)$$

We define new fermionic variables $\zeta = W^\dagger \chi$ and note that due to the structure in Eq. (2.58), $\zeta_{N_S+i} = \zeta_i^\dagger$, for $i = 1, 2, \dots, N_S$. Note that this transformation mixes the operators corresponding to different sites of the wire and the bath, and the index i does not refer to any lattice site. The ζ_i correspond to the ‘‘normal modes’’ of the system. In this basis the Hamiltonian then takes the form

$$\mathcal{H} = \sum_{i=1}^{N_S} \epsilon_i \left(\zeta_i^\dagger(t) \zeta_i(t) - \frac{1}{2} \right) + \frac{1}{2} \text{Tr}[H_S]. \quad (2.60)$$

The evolution of the ζ operators is simply given by $\zeta_j(t) = e^{-i\epsilon_j t} \zeta_j(0)$. Therefore, a two point correlator of the original operators at any time t can be expressed in terms of ζ operators at

$t = 0$ via the transformation W . For the correlator $\langle c_p^\dagger(t)c_q(t) \rangle$, where p, q denotes any site on the entire system, we thus obtain:

$$\begin{aligned} \langle c_p^\dagger(t)c_q(t) \rangle = & \sum_{l,m=1}^{N_S} \left[\mathcal{T}_{N_S+p,q}^{N_S+l,N_S+m} e^{i(\epsilon_l+\epsilon_m)t} \langle \zeta_l^\dagger \zeta_m^\dagger \rangle \right. \\ & + \mathcal{T}_{N_S+p,q}^{lm} e^{-i(\epsilon_l+\epsilon_m)t} \langle \zeta_l \zeta_m \rangle + \mathcal{T}_{N_S+p,q}^{N_S+l,m} e^{-i(-\epsilon_l+\epsilon_m)t} \langle \zeta_l^\dagger \zeta_m \rangle \\ & \left. + \mathcal{T}_{N_S+p,q}^{l,N_S+m} e^{-i(\epsilon_l-\epsilon_m)t} \langle \zeta_l \zeta_m^\dagger \rangle \right], \end{aligned} \quad (2.61)$$

where $\mathcal{T}_{pq}^{lm} = W_{pl}W_{qm}$ and ζ_i in the above equation denotes $\zeta_i(0)$. Using the transformation $\zeta = W^\dagger \chi$, the two point correlations of the ζ operators at $t = 0$ can be determined from the two point correlations of c_p and c_p^\dagger at $t = 0$, which are known once the initial state of the system is specified. In particular we know these correlations for the product initial state used in the previous section, where the reservoirs are described by thermal states with specified temperatures and chemical potentials, while the system is in an arbitrary initial state.

The numerical approach thus consists of finding the eigenspectrum of the matrix \mathcal{Z} and then computing the time evolution of any two-point correlator using Eq. (2.61). Our interest will be in looking at correlations in the wire. For a finite bath we expect to see steady state behaviour of the wire correlations in a time window, which is after some initial transients and before the finite bath effects show up. Thus the correlations would first show some initial evolution, then show a long plateau before finite size effects show up. The steady state properties can be extracted from the plateau region. We will use this procedure in the next section to directly verify the steady state results given by the analytic expressions in the previous section.

2.4.1 Bound states

As discussed earlier we can look for the existence of bound states by examining the spectrum of the matrix \mathcal{Z} . The bound state corresponds to states which lie outside the band width of the baths and the corresponding eigenvector would be spatially localized. The existence

of such bound states in general cause persistent oscillations and steady state properties can become periodic in time. We are in fact now in a position to write down the bound state contributions to Eq. 2.51 and Eq. 2.52 respectively. Let us write the eigenvector of the matrix \mathcal{Z} corresponding to a bound state with eigenvalue E in the form $\begin{pmatrix} \Psi_E \\ \Phi_E \end{pmatrix}$ where $\Psi_E(q) = u_q(E)$ and $\Phi_E(q) = v_q(E)$ (q runs from 1 to N_S). Following Ref. [33], we then see that the contribution of the bound states to Eq. 2.51 and Eq. 2.52 are given by

$$N_{lm}^{BS}(t) = \sum_{i,j,E_b,E_{b'},x=L,R} e^{i(E_{b'}-E_b)t} \left[\Psi_{E_b}(l)\Psi_{E_b}^*(j)\Psi_{E_{b'}}(i)\Psi_{E_{b'}}^*(m) \int d\omega \frac{[\Gamma_x(\omega)]_{ji}f_x(\omega)}{(\omega-E_b)(\omega-E_{b'})} \right. \\ \left. + \Psi_{E_b}(l)\Phi_{E_b}^*(j)\Phi_{E_{b'}}(i)\Psi_{E_{b'}}^*(m) \int d\omega \frac{[\Gamma_x^T(\omega)]_{ji}(1-f_x(\omega))}{(\omega+E_b)(\omega+E_{b'})} + \Psi_{E_b}(l)\Phi_{E_b}^*(j)\Phi_{E_{b'}}(i)\Psi_{E_{b'}}^*(m)\delta_{ij} \right], \quad \text{and} \quad (2.62)$$

$$M_{lm}^{BS}(t) = \sum_{i,j,E_b,E_{b'},x=L,R} e^{-i(E_{b'}+E_b)t} \left[\Psi_{E_b}(l)\Psi_{E_b}^*(j)\Phi_{E_{b'}}(i)\Psi_{E_{b'}}^*(m) \int d\omega \frac{[\Gamma_x(\omega)]_{ji}f_x(\omega)}{(\omega-E_b)(\omega+E_{b'})} \right. \\ \left. + \Psi_{E_b}(l)\Phi_{E_b}^*(j)\Psi_{E_{b'}}(i)\Psi_{E_{b'}}^*(m) \int d\omega \frac{[\Gamma_x^T(\omega)]_{ji}(1-f_x(\omega))}{(\omega+E_b)(\omega-E_{b'})} + \Psi_{E_b}(l)\Psi_{E_b}^*(j)\Phi_{E_{b'}}(i)\Psi_{E_{b'}}^*(m)\delta_{ij} \right] \quad (2.63)$$

respectively. The sum in these expressions runs over all bound state eigenvectors of \mathcal{Z} with positive as well as negative eigenvalues. These are identified from the spectrum of \mathcal{Z} as eigenvectors corresponding to eigenvalues which lie outside the band. In the next section, we demonstrate numerically the fact that the addition of these two corrections to the steady state values gives us the exact long time behaviour of the correlators of the wire. As is clear from these expressions, the bound state contribution would in general cause persistent oscillations in two point correlations of the wire and hence, in all the steady state properties of the wire. The frequencies of these oscillations would be the sum and differences of the energies of the corresponding high energy bound states.

2.5 Numerical verification of QLE-NEGF results and the bound state contributions in a nearest neighbour Kitaev chain

We apply the numerical approach of the previous section on the one-dimensional Kitaev chain to verify the analytical results in Sec. (2.3). We consider a one-dimensional system with N sites on the wire and N_b on each of the two baths and so $N_S = N + 2N_b$. The full system Hamiltonian is given by:

$$\begin{aligned}
\mathcal{H} &= \mathcal{H}_W + \mathcal{H}_L + \mathcal{H}_{WL} + \mathcal{H}_R + \mathcal{H}_{WR} \\
&= \sum_{j=1}^{N-1} \left[-\mu_w a_j^\dagger a_j + (-\eta_w a_j^\dagger a_{j+1} + \Delta a_j a_{j+1} + \text{c.c.}) \right] \\
&\quad + \sum_{\alpha=1}^{N_b-1} \left[-\eta_b (b_\alpha^{L\dagger} b_{\alpha+1}^L + b_{\alpha+1}^{L\dagger} b_\alpha^L) \right] - V_L (a_1^\dagger b_1^L + b_1^{L\dagger} a_1) \\
&\quad + \sum_{\alpha'=1}^{N_b-1} \left[-\eta_b (b_{\alpha'}^{R\dagger} b_{\alpha'+1}^R + b_{\alpha'+1}^{R\dagger} b_{\alpha'}^R) \right] - V_R (a_N^\dagger b_1^R + b_1^{R\dagger} a_N), \tag{2.64}
\end{aligned}$$

where $\{a_j, a_j^\dagger\}$, $\{b_\alpha^R, b_\alpha^{R\dagger}\}$, $\{b_{\alpha'}^L, b_{\alpha'}^{L\dagger}\}$ are annihilation and creation operators on the wire, right and left bath sites respectively. As in Sec. (2.2), we start from the initial state:

$$\rho = \frac{e^{-\beta_L(\mathcal{H}_L - \mu_L \mathcal{N}_L)}}{Z_L} \otimes |0\rangle\langle 0| \otimes \frac{e^{-\beta_R(\mathcal{H}_R - \mu_R \mathcal{N}_R)}}{Z_R}, \tag{2.65}$$

where $\mathcal{N}_{L,R}$ are the number operators in the baths, $Z_x = \text{Tr}(e^{-\beta_x(\mathcal{H}_x - \mu_x \mathcal{N}_x)})$, $x = L, R$, the partition functions of the baths and $|0\rangle\langle 0|$ refers to the wire being initially completely empty. With this choice of the initial state, we can compute all the $t = 0$ correlations required in Eq. (2.61). The eigenvalues and eigenfunctions of the matrix \mathcal{Z} defined in the previous section, corresponding to the Hamiltonian Eq.(2.64), can be easily computed numerically for chains of finite length N_S . For our numerical example we take $N = 2$, $N_b = 100$, and use Eq. (2.61) in the previous section to calculate the time evolution, at any finite time, of the currents $J_L(t) = -2V_L \text{Im}[\langle a_1^\dagger(t) b_1^L(t) \rangle]$, $J_R(t) = -2V_R \text{Im}[\langle a_N^\dagger(t) b_1^R(t) \rangle]$ at the two boundaries

and the densities $N_1(t) = \langle a_1^\dagger(t)a_1(t) \rangle$, $N_2(t) = \langle a_2^\dagger(t)a_2(t) \rangle$.

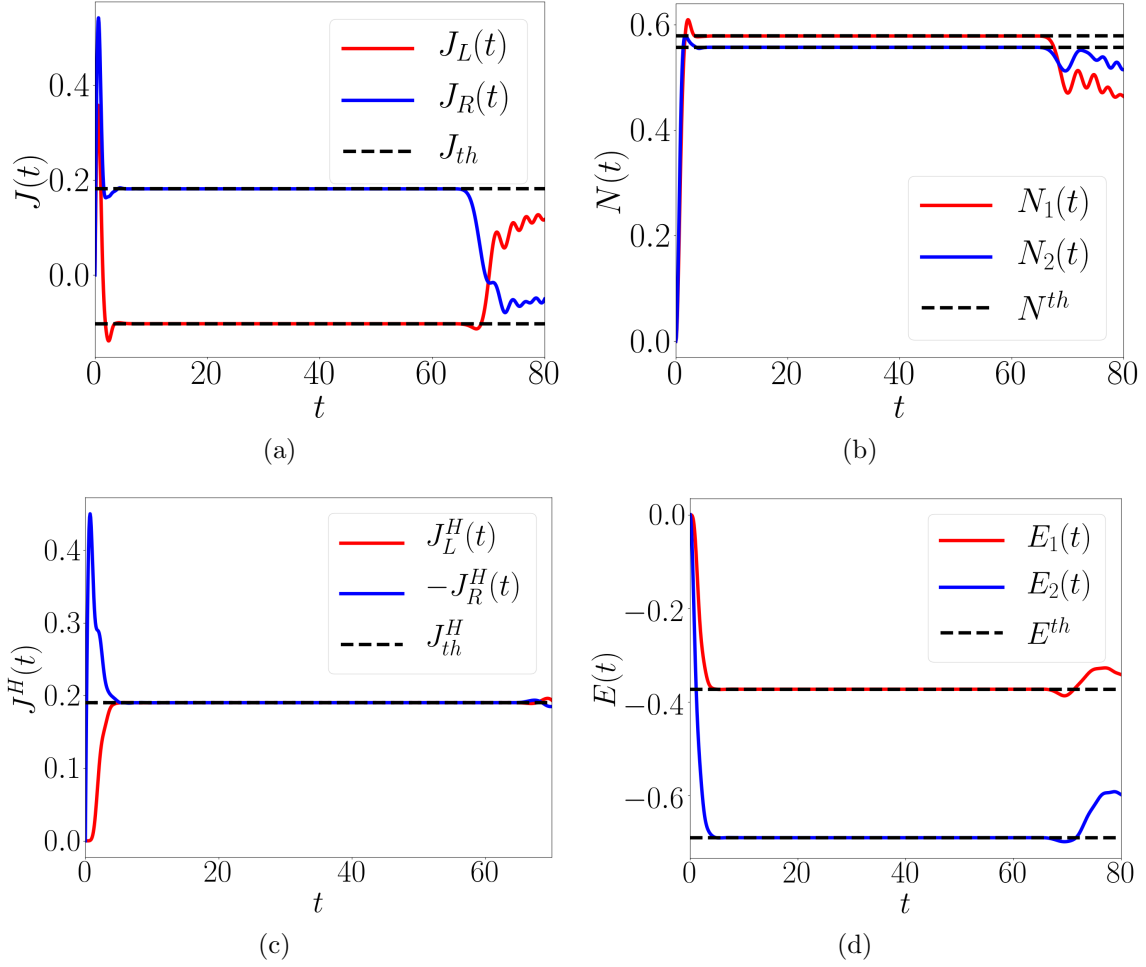


Figure 2.1: Comparison of numerical time-evolution and analytical steady state results: Parameter values — $N = 2$, $N_b = 100$, $\mu_R = 1$, $\beta_R = 10$, $\mu_L = 0$, $\beta_L = 0$, $V_L = V_R = \eta_w = 1$, $\mu_w = 0$, $\eta_b = 1.5$ and $\Delta = 0.40$. (a) Comparison of the numerically calculated particle current at the left, $J_L(t)$, and the right, $J_R(t)$, end of the wire with the corresponding value, J_{th} , given by the expression in Eq. (2.39). (b) Comparison of the numerically calculated densities, $N_1(t) = \langle a_1^\dagger(t)a_1(t) \rangle$ and $N_2(t) = \langle a_2^\dagger(t)a_2(t) \rangle$, on the two sites of the wire with the corresponding value, N_{th} , given by the expression in Eq. (2.51). Similarly, (c) and (d) show the comparison of the energy current and the energy density from direct numerics with the values obtained from steady state expressions. Note that the left and the right heat currents have the same magnitude unlike the particle currents. The initial oscillations seen in the plots correspond to the transient phase, while the behaviour near $t = 60$ is due to the finite size of the baths. In the intermediate region we see perfect agreement between the numerical solution and the steady state value.

The general analytic expressions for the steady state properties of the wire are in terms of the

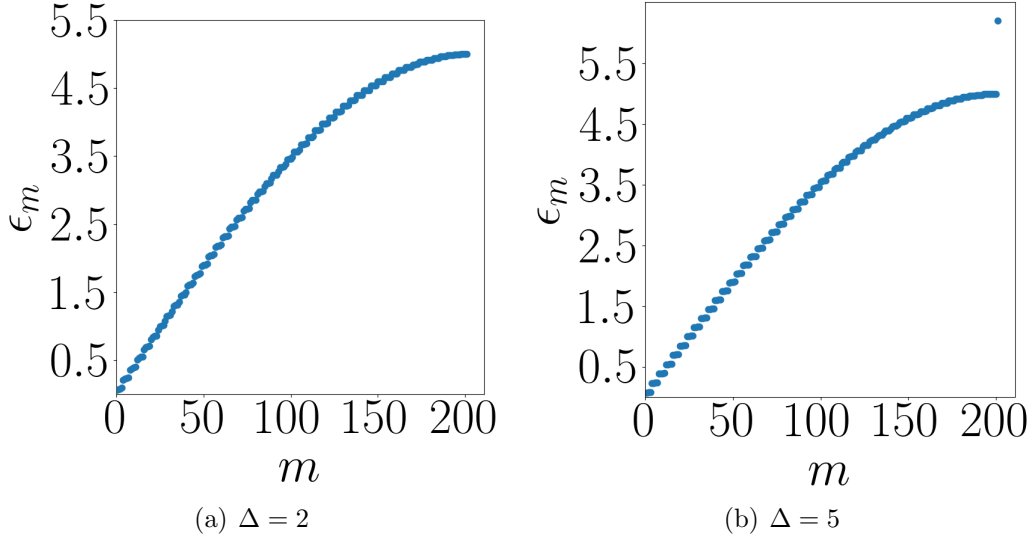


Figure 2.2: Spectrum of the entire system at parameter values $N = 2$, $N_b = 100$, $V^L = V^R = \eta_w = 1$, $\mu_w = 0$ and $\eta_b = 2.5$ for two values of Δ . In (a) we do not see any discrete energy level while in (b) a discrete energy level outside the main band can be seen. As discussed in the text, the non-existence of a steady state, indicated in a non-vanishing I_{ij} , is related to the existence of the discrete level which corresponds to a bound state (see Fig. (2.3)).

two Green's functions $G_1^+(\omega)$ and $G_2^+(\omega)$ defined in Eq. (2.34) and Eq. (2.35) respectively. For the Hamiltonian given in Eq. (2.64), the various matrices involved in them take simpler forms and one finds [33]:

$$K_{ij} = \Delta(\delta_{i,j+1} - \delta_{i,j-1}), \quad (2.66)$$

$$[\Sigma_L^+(\omega)]_{ij} = V_L^2 g(\omega) \delta_{i1} \delta_{j1}, \quad (2.67)$$

$$\pi[\Gamma_L(\omega)]_{ij} = V_L^2 \text{Im}\{g(\omega)\} \delta_{i1} \delta_{j1}, \quad (2.68)$$

$$[\Sigma_R^+(\omega)]_{ij} = V_R^2 g(\omega) \delta_{iN} \delta_{jN}, \quad (2.69)$$

$$\pi[\Gamma_R(\omega)]_{ij} = V_R^2 \text{Im}\{g(\omega)\} \delta_{iN} \delta_{jN}, \quad (2.70)$$

$$\begin{aligned} [\Pi(\omega)]_{ij} &= \omega \delta_{ij} + \eta_s (\delta_{i,j+1} + \delta_{i,j-1}), \\ &\quad - V_L^2 g(\omega) \delta_{i1} \delta_{j1} - V_R^2 g(\omega) \delta_{iN} \delta_{jN}, \end{aligned} \quad (2.71)$$

where $g(\omega) = [g_L^+(\omega)]_{11}$. Since $g_L^+(\omega)$ is the inverse of a tri-diagonal matrix, it can be shown

that [33]

$$g(\omega) = \begin{cases} \frac{1}{\eta_b} \left(\frac{\omega}{2\eta_b} - \sqrt{\frac{\omega^2}{4\eta_b^2} - 1} \right), & \text{if } \omega > 2\eta_b \\ \frac{1}{\eta_b} \left(\frac{\omega}{2\eta_b} + \sqrt{\frac{\omega^2}{4\eta_b^2} - 1} \right), & \text{if } \omega < -2\eta_b \\ \frac{1}{\eta_b} \left(\frac{\omega}{2\eta_b} - i\sqrt{1 - \frac{\omega^2}{4\eta_b^2}} \right), & \text{if } |\omega| < 2\eta_b. \end{cases} \quad (2.72)$$

Using Eqs. (2.66- 2.72) we can compute the steady state value of the current and densities by direct substitution of these expressions in Eq. (2.39) and Eq. (2.51). The integrations over ω in the resulting expressions are carried out numerically. In Fig. (2.1) we show the comparison between the values for the steady state currents (particle and heat) and densities obtained from Eqs. (2.39,2.48,2.51) with the corresponding values obtained from the direct time evolution.

In general we find that, for the parameter regimes over which there exists a steady state, Eq. (2.39) gives the value of the steady state current. We also verified that this expression reproduces the results given in Ref. [15]. As discussed in the end of Sec. (2.3), the non-vanishing of I_{ij} in fact indicates the presence of bound states which leads to the break-down of the NESS assumption. In Figs. (2.2a,2.2b) we show the full energy spectrum of the system for the parameter values $N = 2$, $N_b = 100$, $V^L = V^R = \eta_s = 1$, $\eta_b = 2.5$ and for two values of Δ . We see the appearance of a discrete energy level, indicating a bound state, for the parameter value $\Delta = 5$. In Fig. (2.3a) we show the variation, with Δ , of the quantity $\sum_{i,j} |I_{ij}|^2$ for different parameter regimes of the Hamiltonian in Eq. (2.64) with $N = 2$. We see that the bound state contribution, for any fixed η_b , only kicks in after some critical value of Δ . In Fig. (2.3b) we show the variation of the energy gap, between the bound state level and the band edge, over the same parameter regimes as in Fig. (2.3a). For any fixed η_b , we see that the bound state appears at the same value of Δ as that where I_{ij} in Fig. (2.3a) becomes non-vanishing. In Fig. (2.3c) we plot the real and imaginary parts of the two point correlator $M_{12} = \langle a_1(t)a_2(t) \rangle$, in the presence of bound states, and compare the values obtained from the numerical simulations ($Y(t)$) with the analytic results [$M_{12}^{SS} + M_{12}^{BS}$, using Eqs. (2.52,2.63)]. In the long time limit, the observed agreement requires that we add

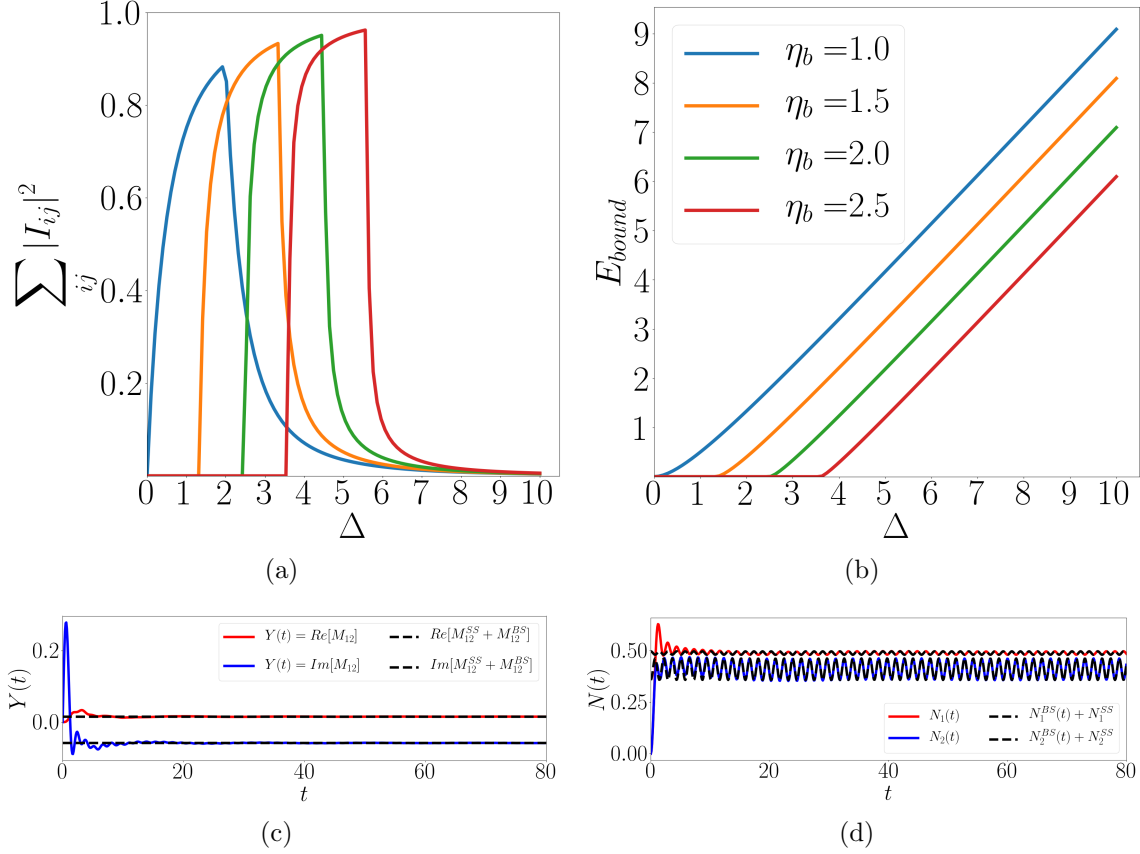


Figure 2.3: (a) The variation of $\sum_{ij} |I_{ij}|^2$ over different parameters of the Hamiltonian in Eq. (2.64) with $\eta_s = V_L = V_R = 1$ and $N = 2$. Physically this quantity should identically vanish. We see that this happens only for certain parameter regimes of the Hamiltonian. In (b) we verify that the non-zero values are associated to the presence of high energy bound states in the spectrum of the full system seen in Fig. (2.2). This plot shows the gap between the bound state energy and the edge of the band, E_{bound} , for the same parameters as in (a). We see that the value of Δ at which the bound state appears is exactly the same value where the corresponding curves in (a) start taking non-zero values. (c) and (d) demonstrate that the numerical simulation for the two-point correlators agrees with the analytic results obtained by adding the bound state contributions to the steady-state values. While (c) shows that the commutation relations are satisfied when we add the bound state contribution (d) on the other hand depicts the persistent oscillations in the particle densities due to the bound states. Parameter values for these two plots are $N = 2$ for (c) and $N = 3$ for (d), $N_b = 100$, $\mu_R = 1$, $\beta_R = 10$, $\mu_L = 0$, $\beta_L = 0$, $V_L = V_R = \eta_w = 1$, $\mu_w = 0$, $\eta_b = 1$ and $\Delta = 0.80$.

the bound state contributions and we recover the correct anti-commutation relations. The bound state contribution leads to persistent oscillations in properties such as densities and this can be seen in Fig. (2.3d) where we compare the analytic result from Eq. 2.62) with the numerical simulation.

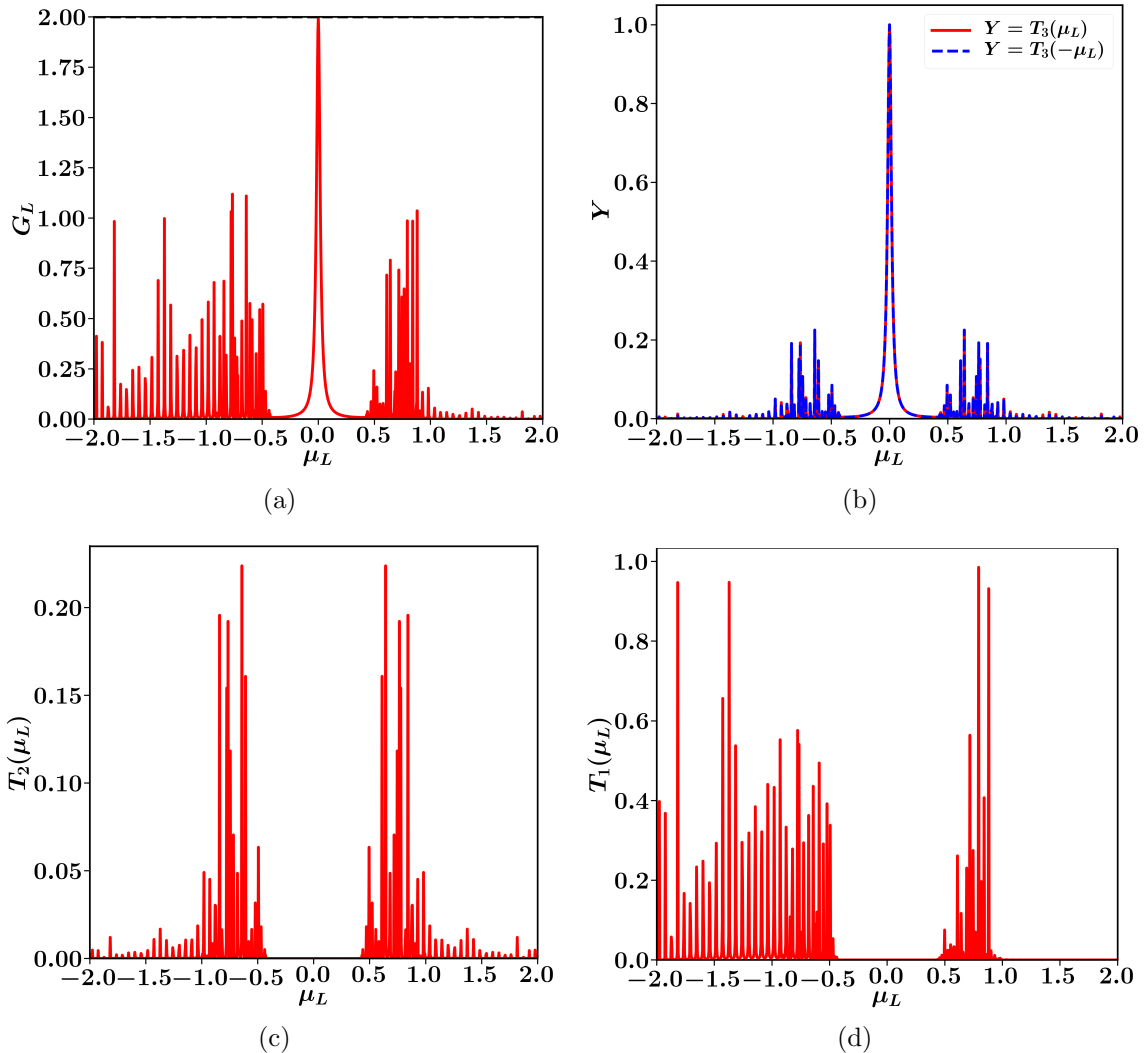


Figure 2.4: Variation of zero temperature conductance and the terms contributing to it with the left bath chemical potential, μ_L . Parameter values– $N = 100$, $V_L = V_R = 0.2$, $\eta_w = \mu_w = 1$, $\eta_b = 1$ and $\Delta = 0.25$.

So far we have discussed short wires and highlighted the role of bound states and how the steady state description needs to be modified in their presence. We now briefly discuss the case of long Kitaev wires where we expect topological phases with Majorana bound states. These zero-energy bound states lie inside the bath band widths and so do not lead to problems in the steady state. The conductance of the Kitaev chain is given by Eq. (3.12) and here we provide a numerical demonstration of the interpretation of the three transmission terms in this equation (see discussions after Eq. (3.12)). For a long wire, Fig. (2.4a) shows the conductance result which reveals the well known zero bias peak of strength 2 in the

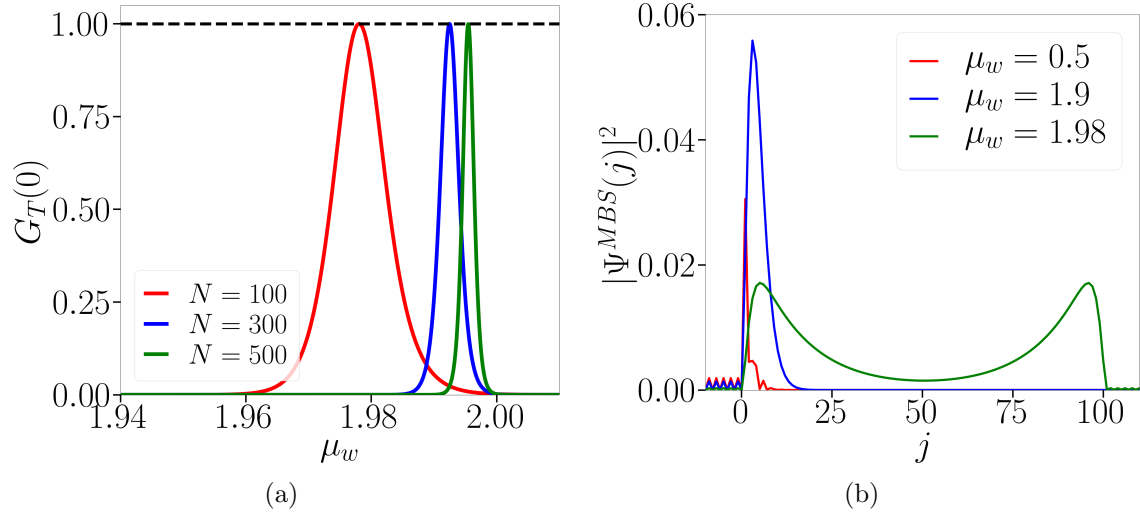


Figure 2.5: (a) Variation of thermal conductance at $\mu_L = 0$ in units of $\pi^2 k_B^2 T_L / 6$ with the chemical potential, μ_w , on the wire for different wire sizes. (b) shows the wave function of the Majorana zero mode at μ_w far away and close to the topological phase transition point for $N = 100$. The extended nature of the Majorana wave functions spreading across the wire can be clearly seen when μ_w is close to the phase transition point. Other Parameter values— $V_L = V_R = 0.25$, $\eta_w = \eta_b = 1$ and $\Delta = 0.3$.

topologically non trivial parameter regime, $|\mu_w| < 2|\eta_w|$, of the wire Hamiltonian. This peak is due to the existence of the zero energy Majorana bound states in this parameter regime. In Figs. (2.4b,2.4c,2.4d) we show the variation of the three terms which contribute to the conductance. As is clear from these plots, the peak is due to the perfect Andreev reflection at zero bias owing to the Majorana bound state. Within the superconducting gap, we also find $T_1(\mu_L) = T_2(\mu_L) = 0$ for long wires which is consistent with their physical interpretation as normal and Andreev transmission amplitudes. The transmission from left to right bath for long wires (long enough so that the Majorana modes are isolated) can only occur via excitation of quasiparticles within the wire which is not possible if μ_L lies within the superconducting gap.

We now consider the thermal conductance at the left end at zero bias ($\mu_L = 0$). This is given by Eq. (2.49) and we see that it is proportional to the net transmission, $T_1(0) + T_2(0)$. As we just discussed, if the wire is long enough so that the Majorana modes have no overlap within the wire, the net transmission and hence the zero bias thermal conductance would be zero. However, for a fixed finite size of the wire as we move closer to the topological phase transition

point, $\mu_w = 2\eta_w$, the spread of the Majorana zero modes in the wire increases and as we approach the phase transition point, these modes hybridize to form two extended modes. This can be seen in Fig. (2.5b) where we plot the MBS wavefunctions for a few different μ_w values. This would then result in non-zero transmission probabilities at zero bias. As a result the thermal conductance for a finite sized wire will take finite values sufficiently close to the transition point. In Fig. (2.5a) we show the variation of thermal conductance at zero bias with μ_w while keeping other parameters fixed. We see that for a fixed N the thermal conductance peaks to a strength 1 (in units of the thermal conductance) at a μ_w value close to the infinite size phase transition point. Note that this means that Andreev reflection is now suppressed and so the electrical conductance peak at zero bias would reduce from the value 2. We also see that with increasing system size, the the peak becomes narrower and moves closer to the phase transition point. This peak has been noted recently [56] and we point out here that there are strong finite size effects and in particular the vanishing width with increasing wire size would make this difficult to observe experimentally.

2.6 Next nearest neighbour Kitaev chain

Finally in this section, as an application of our very general formalism, we discuss the transport properties of an open Kitaev chain with interaction couplings that extend beyond nearest neighbours. In particular we consider a wire Hamiltonian with next nearest neighbour couplings:

$$\mathcal{H}^W = \sum_{j=1}^N \left[-\mu_w a_j^\dagger a_j - \eta_1 (a_j^\dagger a_{j+1} + a_j a_{j+1} + \text{c.c.}) - \eta_2 (a_j^\dagger a_{j+2} + e^{i\theta} a_j a_{j+2} + \text{c.c.}) \right]. \quad (2.73)$$

The other parts of the total Hamiltonian (bath and wire-bath coupling) are taken to be the same as the Hamiltonian in Eq. 2.64. Such models have been discussed for the closed system and follow from Jordan Wigner transformation of a 1-D transverse Ising model with three spin interactions. The phase diagram of such a model reveals very interesting features [59].

For $\theta = 0$, one has two different topologically non-trivial phases, phase-1 and phase-2, apart from the topologically trivial phase (phase-0). Phase-1 and phase-2 contain one and two zero modes localized at each end respectively. However, for $\theta \neq 0$ the energy of the localized modes of phase-2 is lifted from zero to a finite value. These facts can be seen in the spectrum of the isolated wire Hamiltonian in the three phases for the case of zero and non-zero θ and we show this in Fig. (2.6a) and Fig. (2.6b). The different values of $\eta_2 = -1.5, 0.5$, and 1 in these spectral plots lie in the parameter regimes of phase-2, phase-0 and phase-1 respectively. The topological edge modes can be seen between the superconducting gap near zero energy.

In Fig. (2.6c) and Fig. (2.6d) we show the conductance results of this model obtained from Eq. 2.45, evaluated with the Hamiltonian in Eq. (2.73), for the parameter regimes of the three phases at zero and non-zero θ respectively. We see that for $\theta = 0$ there is a single zero bias peak as all topological edge modes in the three phases are of zero energy. However, for $\theta \neq 0$ we see two distinct peaks of strength 2 for the case of phase-2 at the same energy as the energy of the topological edge mode. Thus phase-2 is accompanied by two perfect Andreev reflections at energies of the edge modes and the degeneracy of the modes localized at the two ends is broken. Phase-1 on the other hand has a single peak at zero energy for θ being zero or non-zero representing the fact that the degeneracy of the zero modes at the two ends is not lifted. Phase-0 as usual has no such peak since there are no edge modes. The splitting of the conductance peak seen in Fig. (2.6d) has recently been observed in a ladder system of two coupled chains with long range interactions (power-law form) within each chain [60].

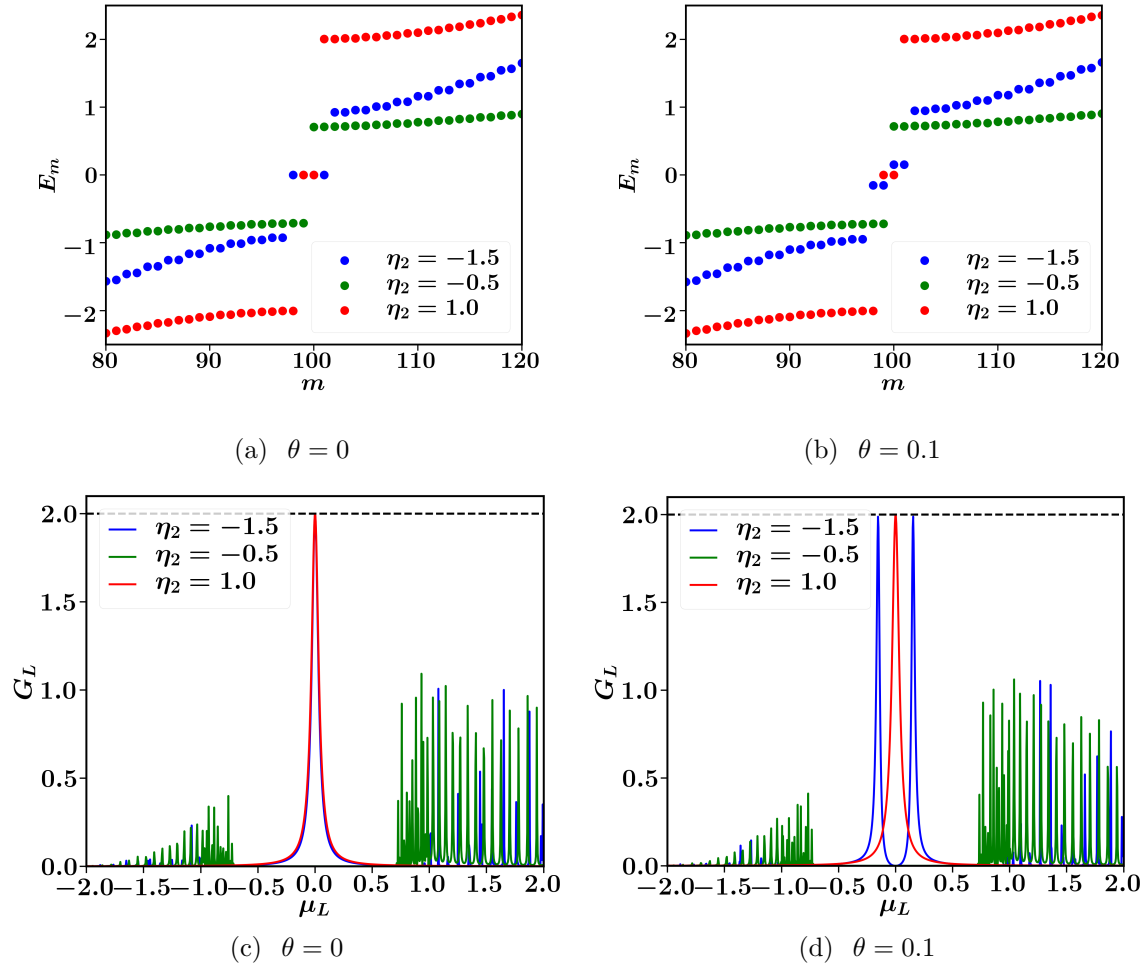


Figure 2.6: (a) and (b) show the spectrum of an isolated next nearest neighbour Kitaev chain at the parameter values $\eta_1 = 1$, $\mu_w = -2$, $N = 100$, $V_L = V_R = 0.3$ and $\eta_b = 1.5$ at zero and non-zero values of θ and for the values of $\eta_2 = -1.5$, -0.5 and 1 corresponding to phase-2, phase-0 and phase-1 respectively. The topological edge modes can be seen in the spectral plots in between the superconducting gap. The corresponding conductance results obtained from Eq. 2.45 are shown in (c) and (d). The conductance plots for $\theta = 0$ show a single zero bias peak for the two topologically non-trivial phases while they show two distinct peaks for a non-zero θ value for phase-2.

2.7 Conclusion

In conclusion, we considered transport in a wire that is modelled by a spinless superconductor with a mean-field pairing form for the interaction term, so that it is effectively described by a general quadratic Hamiltonian. We investigated transport in the wire for the so-called N-S-N geometry where the superconductor is placed between normal leads. Thus, in our set-up, the

wire is attached to free electron baths at different temperatures and chemical potentials and we investigated particle and energy transport, using the open system framework of quantum Langevin equations (QLE) and nonequilibrium Green's function (NEGF).

Our main results are the exact analytic expressions for the particle current, energy current, other two-point correlations in the nonequilibrium steady state and high energy bound state corrections to them. These have the same structure as NEGF expressions for free electrons, but now involve two sets of Green's functions. We show that current expressions generically involve three types of terms which can be physically interpreted in terms of normal and Andreev processes. We also derive the Landauer formula for the heat current and show that the Andreev reflection process does not contribute to this leading to absence of a zero bias peak in the thermal conductance for parameter regimes far away from the topological phase transition point. However, for fixed wire sizes the zero bias thermal conductance shows a peak as one moves sufficiently close the transition point. To derive these expressions one has to assume the existence of a nonequilibrium steady state and we relate this to the existence of bound states (discrete energy levels) in the spectrum of the entire coupled system of the superconducting wire and the baths. The role of bound states on the existence of steady states is known for normal systems [33, 61, 62, 63] and has recently been investigated numerically for the case of superconductors in Ref. [58]. In the present work, we examined this issue analytically for a general spinless superconductor and obtained explicit expressions for the bound state contributions to the two point correlators.

Next, by performing an exact numerical diagonalization of the full quadratic Hamiltonian of wire and baths, we computed the time evolution of the current and local densities, starting from the same initial density matrix as used in the steady state calculations. We then showed that the results from this approach agree perfectly with the analytic expressions, both for the case where there are no high energy bound states and also in the presence of such states after we add the additional correction terms to the usual steady state results. We verify from the numerics that these correction terms are crucial in ensuring that the fermionic anti-commutation relations are satisfied. Our analytic results for the bound states also reproduce the persistent temporal oscillations observed in the steady state.

Finally, as an application of our general formalism, we investigated the conductance results of long wires for a Kitaev chain with next neighbour interactions. In particular it is known that several interesting topological phases are obtained if one adds a phase difference between the superconducting pairings of the nearest neighbour and next neighbour terms. We found that the conductance peak of strength 2 exists whenever the system is in a topologically non-trivial phase. However, in the topologically non-trivial phase-3 the presence of the phase difference leads to a lifting of the degeneracy of the topological edge modes and consequently the conductance results showed two distinct peaks at the new energies of the edge modes. Our general formalism can be readily applied to other physically interesting set-ups such as those studied in Refs. [64, 65].

Chapter 3

Equivalence of Scattering and QLE-NEGF in 1-D Kitaev Chain

Multiple scattering processes lead to transport of particles and energy in a Kitaev chain as we discussed in the previous chapter. These include the normal transmission, normal reflection, Andreev's transmission and reflection. In the previous chapter, we argued that these scattering processes show up in the expression for the particle current as different NEGF-transmission functions namely $T_1(\omega)$, $T_2(\omega)$ and $T_3(\omega)$. In this chapter, we analytically demonstrate the physical interpretation of these terms as the normal transmission, Andreev's transmission and reflection respectively.

We start in Sec. 3.1, where we quickly reintroduce the Kitaev model connected to metallic leads with a slightly different notation and state the main results of chapter 2. We also qualitatively discuss the scattering approach and its expected equivalence with the QLE-NEGF method. In Sec. 3.2 we provide explicit details of the calculation involved in scattering approach and also discuss the zero mode Majorana bound state(MBS) in this system. The analytical proof for the equivalence of the two approaches is given in Sec. 3.3. We conclude in Sec. 3.4.

3.1 The model and the equivalence of the two approaches

In this section, we introduce the model for the Kitaev chain connected to reservoirs at its two ends and then summarize the results obtained by applying the QLE-NEGF approach and the scattering approach to this model. After that, we qualitatively discuss the equivalence of the two approaches which is later proven analytically in Sec. 3.3. As mentioned in the previous chapter, the Hamiltonian of the Kitaev chain(1-D wire), \mathcal{H}_W , is given by normal tight binding Hamiltonian with mean field BCS-type coupling between its neighbouring sites. We once again take the reservoirs are taken to be semi-infinite chains with nearest neighbour tight binding Hamiltonians, \mathcal{H}_L and \mathcal{H}_R . L and R refer to the left and the right reservoir respectively. The finite ends of the reservoirs are placed at ends of the wire and its extremal sites are coupled to the nearest reservoir sites via tight binding Hamiltonians, \mathcal{H}_{WL} and \mathcal{H}_{WR} . The creation and annihilation operators, satisfying usual fermionic anti-commutation relations, for the wire, the left bath and the right bath are denoted as $\{c_j^\dagger, c_j\}$, $\{c_\alpha^\dagger, c_\alpha\}$ and $\{c_{\alpha'}^\dagger, c_{\alpha'}\}$ respectively. The Latin indices $j, k, ..$ are taken to label the sites on the wire. These take values from $1, 2, \dots, N$, N being the number of sites on the wire. Similarly, Greek indices $\alpha, \nu, ..$ taking values from $-\infty, \dots, -1, 0$ and primed Greek indices $\alpha', \nu', ..$ taking values from $N + 1, N + 2, \dots, \infty$ label the left reservoir and right reservoir sites respectively. The full

Hamiltonian is thus given by,

$$\mathcal{H} = \mathcal{H}_W + \mathcal{H}_{WL} + \mathcal{H}_{WR} + \mathcal{H}_L + \mathcal{H}_R, \quad (3.1)$$

$$\text{where } \mathcal{H}_W = \sum_{j=1}^{N-1} \left[-\mu_w c_j^\dagger c_j - \eta_w (c_j^\dagger c_{j+1} + c_{j+1}^\dagger c_j) + \Delta (c_j c_{j+1} + c_{j+1}^\dagger c_j^\dagger) \right], \quad (3.2)$$

$$\mathcal{H}_{WL} = -\eta_c (c_1^\dagger c_0 + c_0^\dagger c_1), \quad (3.3)$$

$$\mathcal{H}_{WR} = -\eta_c (c_N^\dagger c_{N+1} + c_{N+1}^\dagger c_N), \quad (3.4)$$

$$\mathcal{H}_L = -\eta_b \sum_{\alpha=-\infty}^0 c_\alpha^\dagger c_{\alpha+1} + c_{\alpha+1}^\dagger c_\alpha, \quad (3.5)$$

$$\mathcal{H}_R = -\eta_b \sum_{\alpha'=N+1}^{\infty} c_{\alpha'}^\dagger c_{\alpha'+1} + c_{\alpha'+1}^\dagger c_{\alpha'}, \quad (3.6)$$

where Δ , η_w , μ_w are respectively the superconducting pairing strength, hopping amplitude and the chemical potential on the sites of the wire, η_c is the coupling strength between the wire and the reservoirs, and the hopping amplitude in the reservoirs is given by η_b . For simplicity, all of these parameters are taken to be real. The reservoirs are initially described by grand canonical ensembles at temperatures, T_L, T_R and chemical potentials, μ_L, μ_R and, as we will see, this determines the correlation properties of the noise terms in the final Langevin equations.

In the previous chapter, we showed that the current entering the wire from the left reservoir is given by,

$$J_L = \int_{-\infty}^{\infty} \frac{d\omega}{2\pi} \left(T_1(\omega) (f_L^e(\omega) - f_R^e(\omega)) + T_2(\omega) (f_L^e(\omega) - f_R^h(\omega)) + T_3(\omega) (f_L^e(\omega) - f_L^h(\omega)) \right), \quad (3.7)$$

where $f_X^e(\omega) = f(\omega, \mu_X, T_X)$, $f_X^h(\omega) = f(\omega, -\mu_X, T_X)$, ($X = L, R$) are the electron and hole

occupation numbers and

$$T_1(\omega) = 4\pi^2 \text{Tr} [G_1^+(\omega)\Gamma_R(\omega)G_1^-(\omega)\Gamma_L(\omega)], \quad (3.8)$$

$$T_2(\omega) = 4\pi^2 \text{Tr} [G_2^+(\omega)\Gamma_R^T(-\omega)G_2^-(\omega)\Gamma_L(\omega)], \quad (3.9)$$

$$T_3(\omega) = 4\pi^2 \text{Tr} [G_2^+(\omega)\Gamma_L^T(-\omega)G_2^-(\omega)\Gamma_L(\omega)]. \quad (3.10)$$

From the expression for current we can obtain the conductance at the left end and, in units of e^2/h , is found to be:

$$G_L(T_L, \mu_L) = 2\pi \frac{\partial J_L}{\partial \mu_L}, \quad (3.11)$$

which at, $T_L = T_R = 0$, gives:

$$G_L = T_1(\mu_L) + T_2(\mu_L) + T_3(\mu_L) + T_3(-\mu_L). \quad (3.12)$$

The transmission functions involve the two Green's functions $G_1^+(\omega)$ and $G_2^+(\omega)$ given by Eq. (2.34) and Eq. (2.35) respectively. The various matrices which are present in their expression have simple forms and are given by:

$$[\Sigma_L^+(\omega)]_{ij} = \eta_c^2 \Sigma(\omega) \delta_{i1} \delta_{j1}, \quad (3.13)$$

$$[\Gamma_L(\omega)]_{ij} = \frac{\eta_c^2}{\pi} g(\omega) \delta_{i1} \delta_{j1}, \quad (3.14)$$

$$[\Sigma_R^+(\omega)]_{ij} = \eta_c^2 \Sigma(\omega) \delta_{iN} \delta_{jN}, \quad (3.15)$$

$$[\Gamma_R(\omega)]_{ij} = \frac{\eta_c^2}{\pi} g(\omega) \delta_{iN} \delta_{jN}, \quad (3.16)$$

$$\begin{aligned} [\Pi(\omega)]_{ij} &= (\omega + \mu_w) \delta_{ij} + \eta_w (\delta_{i,j+1} + \delta_{i,j-1}) \\ &\quad - \eta_c^2 \Sigma(\omega) \delta_{i1} \delta_{j1} - \eta_c^2 \Sigma(\omega) \delta_{iN} \delta_{jN}, \end{aligned} \quad (3.17)$$

where $g(\omega) = \text{Im}[\Sigma(\omega)]$, and is given by

$$\Sigma(\omega) = \begin{cases} \frac{1}{\eta_b} \left(\frac{\omega}{2\eta_b} - \sqrt{\frac{\omega^2}{4\eta_b^2} - 1} \right), & \text{if } \omega > 2\eta_b \\ \frac{1}{\eta_b} \left(\frac{\omega}{2\eta_b} + \sqrt{\frac{\omega^2}{4\eta_b^2} - 1} \right), & \text{if } \omega < -2\eta_b \\ \frac{1}{\eta_b} \left(\frac{\omega}{2\eta_b} - i\sqrt{1 - \frac{\omega^2}{4\eta_b^2}} \right), & \text{if } |\omega| < 2\eta_b. \end{cases} \quad (3.18)$$

Using these results, the terms involved in the NEGF-expression for conductance become

$$T_1(\omega) = 4\eta_c^4 g^2(\omega) |[G_1^+(\omega)]_{1N}|^2, \quad (3.19)$$

$$T_2(\omega) = 4\eta_c^4 g^2(\omega) |[G_2^+(\omega)]_{1N}|^2, \quad (3.20)$$

$$T_3(\omega) = 4\eta_c^4 g^2(\omega) |[G_2^+(\omega)]_{11}|^2. \quad (3.21)$$

We will use these expressions for the analytical proof of the equivalence of the two methods in Sec. 3.3.

We want to compare these results with the results from the scattering approach to the same problem. Here we present a qualitative discussion of the scattering formalism and relegate the details of the calculation to Sec. (3.2). The first step in the scattering approach would be to identify the different scattering processes that could take place in the system. Let us consider a plane wave incident on the wire from the left reservoir and then, considering the wire as a scatterer, we note that there are a total of four processes that can take place. Two of these processes are — (i) an electron from the left reservoir being reflected back into the left reservoir and (ii) an electron from the left reservoir being transmitted across the wire into the right reservoir. We will refer to these as normal reflection and normal transmission processes respectively. However, in a superconductor the electron and hole wavefunctions are intertwined and therefore an electron may get scattered as a hole also. This results in the two additional scattering process in which an electron from the left reservoir can (iii) get reflected back as a hole into the left reservoir or (iv) get transmitted across the wire as a hole into the right reservoir. We refer to these as Andreev reflection and transmission respectively. During these two processes, charge conservation is ensured by the formation of

a cooper pair in the wire.

Having identified the scattering processes, the next step would be to write down a stationary state wavefunction, at some energy E , in the three regions of the system (the wire, left bath, right bath) with appropriate scattering amplitudes and wavefunctions so that all the scattering processes are captured. In the left reservoir, we thus have the incoming plane wave and the outgoing plane waves for the reflected electron and hole corresponding to the normal and Andreev reflection respectively. The reflected electron and hole plane waves are multiplied by some scattering amplitudes which we take to be r_n and r_a respectively. Similarly, in the right reservoir we will have the transmitted electron and hole plane waves from the normal transmission and the Andreev transmission respectively and we take the scattering amplitudes for these to be t_n and t_a respectively. In the wire, the wavefunction will be a superposition of quasi particles of the wire at energy E which are defined in terms of the diagonalization of the bulk wire Hamiltonian. The normal and Andreev scattering amplitudes are obtained by implementing the boundary conditions and then the conductance at the left junction, in units of e^2/h , is given by the net probability of an electron to be transmitted across the left junction which is

$$G_L^S = |t_n|^2 + |t_a|^2 + 2|r_a|^2 = 1 - |r_n|^2 + |r_a|^2. \quad (3.22)$$

The last step follows from the probability conservation, $|r_n|^2 + |r_a|^2 + |t_n|^2 + |t_a|^2 = 1$. The factor 2 in Eq. (3.22) with $|r_a|^2$ is due to the fact that in the Andreev reflection process, two electrons are transmitted across the junction as a single cooper pair.

Now in order to compare these two independent approaches note that the NEGF expression for the current, Eq. (3.7), has contribution from three terms. On comparison of these three terms with the usual Landauer formulas for current one may expect the following: the first term has electrons as incoming and outgoing particles and therefore this must be the contribution of the electron from the left bath being scattered as an electron into the right bath (normal transmission), the second term having electrons and holes in the opposite baths as the incoming and outgoing particles respectively should correspond to the process of an

electron from the left bath being scattered as a hole into the right bath (Andreev transmission). Finally, the third term which also has electrons and holes as incoming and outgoing particles respectively but in the same bath would therefore correspond to the electron from the left bath scattered back as a hole into left bath again (Andreev reflection). The traces in the three terms should then be proportional to the probability of these three processes respectively. Therefore, the first two terms of the conductance expression in Eq. (3.12) calculated at energy E , $T_1(E)$ and $T_2(E)$ should be equal to the probabilities from the scattering amplitudes t_n and t_a at the same energy respectively and the sum of the last two terms, $T_3(E)$ and $T_3(-E)$, both of which follow from the third term of the current expression in Eq. (3.7) should then be equal to $2|r_a|^2$. This would make the two conductance expressions, in Eq. (3.12) and Eq. (3.22), from the two approaches exactly the same. In Sec. 3.3 we present an exact proof of this result but for now we proceed to Sec. (3.2) where we present the details of the calculations involved in the scattering approach.

3.2 Scattering approach

In this section, we first find out the stationary states of energy E inside the left reservoir, the wire and the right reservoir. This would enable us to write down the scattering wavefunction as discussed in Sec. 3.1 in the three regions and after implementing the boundary conditions, at the reservoir-wire junctions, we would obtain a set of linear equations for the normal and Andreev scattering amplitudes. The conductance could then be obtained via Eq. (3.22). Afterwards, we discuss the case of $E = 0$ separately and find the wavefunctions and the parameter regime of existence of the MBS.

Consider for the moment the case where the wire has N sites while the left and right reservoirs have N_L and N_R number of sites respectively so that the total number of sites is $N_S = N + N_L + N_R$. Let us define a column vector $\chi_p = \begin{pmatrix} c_p \\ c_p^\dagger \end{pmatrix}$, where the index p refers to any

We choose $\Psi_W(j) = \begin{pmatrix} U \\ V \end{pmatrix} z^j$ and fix z such that the Eq. (3.27) is satisfied. On substitution of $\Psi_W(j)$ in Eq. (3.27), we arrive at the following equation,

$$\begin{pmatrix} \eta_w(z + \frac{1}{z}) + \mu_w + E & \Delta(z - \frac{1}{z}) \\ \Delta(z - \frac{1}{z}) & \eta_w(z + \frac{1}{z}) + \mu_w - E \end{pmatrix} \begin{pmatrix} U \\ V \end{pmatrix} = 0, \quad (3.28)$$

which means that z must be fixed such that

$$\begin{vmatrix} \eta_w(z + \frac{1}{z}) + \mu_w + E & \Delta(z - \frac{1}{z}) \\ \Delta(z - \frac{1}{z}) & \eta_w(z + \frac{1}{z}) + \mu_w - E \end{vmatrix} = 0. \quad (3.29)$$

Clearly, there are four possible solutions for z as this determinant on expansion will give a fourth order equation in z . However, we can make things a bit simpler by choosing $z = e^x$ so that the above determinant on expansion gives a quadratic equation in $\cosh x$ rather than a fourth order equation in z . The quadratic equation thus obtained is the following:

$$(\cosh x)^2 - \frac{\mu\eta_w}{\Delta^2 - \eta_w^2} \cosh x + \frac{E^2 - \mu^2 - 4\Delta^2}{4(\Delta^2 - \eta_w^2)} = 0 \quad (3.30)$$

with its two solutions given by

$$\cosh x_{\pm} = \frac{\mu_w\eta_w \pm \sqrt{(\eta_w^2 - \Delta^2)(E^2 - 4\Delta^2) + \Delta^2\mu_w^2}}{2(\Delta^2 - \eta_w^2)}. \quad (3.31)$$

Therefore, the four possible solutions to z , which are obtained from the two quadratic equations $z^2 - 2 \cosh x_{\pm} z + 1 = 0$, are given by

$$z_1 = e^{-x_+}, \quad z_2 = e^{-x_-}, \quad z_3 = e^{x_+}, \quad z_4 = e^{x_-}. \quad (3.32)$$

From Eq. (3.28), we see that U and V for the corresponding solutions for z could be chosen

in the following form:

$$U_s = -\Delta(z_s^2 - 1) \quad (3.33)$$

$$V_s = \eta_w(z_s^2 + 1) + z_s(\mu_w + E) \quad (3.34)$$

where $s = 1, 2, 3, 4$ for the four solutions of z . Therefore, we have the required stationary states inside the wire. Now, the stationary states of energy E inside the baths can be obtained from the wire solution via the transformation, $\mu_w \rightarrow 0$, $\Delta \rightarrow 0$ and $\eta_w \rightarrow \eta_b$. We get the solutions to be two left travelling plane waves and two right travelling plane waves of the following forms:

$$\begin{pmatrix} 1 \\ 0 \end{pmatrix} e^{iqx}, \quad \begin{pmatrix} 1 \\ 0 \end{pmatrix} e^{-iqx}, \quad (3.35)$$

$$\begin{pmatrix} 0 \\ 1 \end{pmatrix} e^{iq'x}, \quad \begin{pmatrix} 0 \\ 1 \end{pmatrix} e^{-iq'x}, \quad (3.36)$$

where q and q' are given by $\cos^{-1}\left(-\frac{E}{2\eta_b}\right)$ and $\cos^{-1}\left(-\frac{E}{2\eta_b}\right) - \pi$ respectively. Physically, the first two solutions, Eq. (3.35), correspond to an electron travelling right and left respectively while the last two solutions, Eq. (3.36), correspond to a hole travelling to the right and left respectively.

We are now in a position to write the explicit form of the scattering wavefunction in the three regions for a plane wave of energy E incident from the left reservoir. This will be of the form:

$$\Psi_L(\alpha) = \begin{pmatrix} 1 \\ 0 \end{pmatrix} e^{iq\alpha} + r_n \begin{pmatrix} 1 \\ 0 \end{pmatrix} e^{-iq\alpha} + r_a \begin{pmatrix} 0 \\ 1 \end{pmatrix} e^{-iq'\alpha} \quad (3.37)$$

$$\Psi_W(j) = \sum_{s=1}^4 a_s \begin{pmatrix} U_s \\ V_s \end{pmatrix} z_s^{j-1} \quad (3.38)$$

$$\Psi_R(\alpha') = t_n \begin{pmatrix} 1 \\ 0 \end{pmatrix} e^{iq(\alpha'-N-1)} + t_a \begin{pmatrix} 0 \\ 1 \end{pmatrix} e^{iq'(\alpha'-N-1)} \quad (3.39)$$

with $\alpha = -\infty, \dots, -1, 0$, $j = 1, 2, \dots, N$ and $\alpha' = N + 1, N + 2, \dots, \infty$. As already discussed in Sec. (3.1), r_n is the probability amplitude for the electron to be reflected back at the left junction as an electron. Therefore, this corresponds to the normal reflection. r_a is the probability amplitude for the Andreev reflection. Similarly, t_n and t_a are the normal and the Andreev transmission amplitudes respectively. The solution inside the wire represents a superposition, with amplitudes a_1, a_2, a_3 and a_4 , of the quasi-particles with energy E in the wire travelling to the left and right respectively. These scattering amplitudes are obtained by implementing the boundary conditions. We note that we have eight scattering amplitudes and two boundaries, one at the left end and the other at the right end of the wire. Each site on either side of each boundary gives two equations. Therefore, a single boundary gives four equations in total and we have exactly eight equations from the two boundaries, sufficient to determine the eight scattering amplitudes. These eight boundary equations are given by

$$A_L \Psi_L(-1) + A_C \Psi_W(1) = E \Psi_L(0), \quad (3.40)$$

$$A_C \Psi_L(0) + A \Psi_W(1) + A_W \Psi_W(2) = E \Psi_W(1), \quad (3.41)$$

$$A_W^T \Psi_W(N-1) + A \Psi_W(N) + A_C \Psi_R(N+1) = E \Psi_W(N), \quad (3.42)$$

$$A_C^T \Psi_W(N) + A_R \Psi_R(N+2) = E \Psi_R(N+1). \quad (3.43)$$

After substituting the solution from Eqs. (3.37, 3.38, 3.39), the eight linear equations for the scattering amplitudes can be expressed in matrix form as

$$\begin{pmatrix} \eta_b e^{iq} + E & 0 & \eta_c U_1 & \eta_c U_2 & \eta_c U_3 & \eta_c U_4 & 0 & 0 \\ 0 & \eta_b e^{iq'} - E & \eta_c V_1 & \eta_c V_2 & \eta_c V_3 & \eta_c V_4 & 0 & 0 \\ \eta_c & 0 & f_1 & f_2 & f_3 & f_4 & 0 & 0 \\ 0 & \eta_c & f'_1 & f'_2 & f'_3 & f'_4 & 0 & 0 \\ 0 & 0 & g_1 & g_2 & g_3 & g_4 & \eta_c & 0 \\ 0 & 0 & g'_1 & g'_2 & g'_3 & g'_4 & 0 & \eta_c \\ 0 & 0 & \eta_c z_1^{N-1} U_1 & \eta_c z_2^{N-1} U_2 & \eta_c z_3^{N-1} U_3 & \eta_c z_4^{N-1} U_4 & \eta_b e^{iq} + E & 0 \\ 0 & 0 & \eta_c z_1^{N-1} V_1 & \eta_c z_2^{N-1} V_2 & \eta_c z_3^{N-1} V_3 & \eta_c z_4^{N-1} V_4 & 0 & \eta_b e^{iq'} - E \end{pmatrix} \begin{pmatrix} r_n \\ r_a \\ a_1 \\ a_2 \\ a_3 \\ a_4 \\ t_n \\ t_a \end{pmatrix} = \begin{pmatrix} -\eta_b e^{-iq} - E \\ 0 \\ -\eta_c \\ 0 \\ 0 \\ 0 \\ 0 \\ 0 \end{pmatrix}, \quad (3.44)$$

where for $s = 1, 2, 3, 4$ the f_s , f'_s , g_s and g'_s are given by

$$f_s = (\mu_w + E)U_s + z_s(\eta_w U_s + \Delta V_s), \quad (3.45)$$

$$f'_s = (\mu_w - E)V_s + z_s(\eta_w V_s + \Delta U_s), \quad (3.46)$$

$$g_s = (\mu_w + E)U_s z_s^{N-1} + (\eta_w U_s - \Delta V_s)z_s^{N-2}, \quad (3.47)$$

$$g'_s = (\mu_w - E)V_s z_s^{N-1} + (\eta_w V_s - \Delta U_s)z_s^{N-2}. \quad (3.48)$$

Solving Eqs. (3.44) gives us the required expressions for r_n , r_a , t_n and t_a , and from these we can obtain the conductance using the scattering approach.

We now look for the special solution corresponding to the zero energy MBS in this open wire system. We expect that for long enough wires there are two MBS each localized at edges of the wire. Let us consider a zero energy eigenstate localized at the left end ($j = 1$), therefore for this we must have $t_n = 0$, $t_a = 0$ and $a_s = 0$ if $|z_s| \geq 1$ in the wavefunction given by Eq. (3.37, 3.38, 3.39) with $E = 0$. Out of the four roots, z_1 , z_2 , z_3 and z_4 , it is clear that two of them always have absolute values greater than 1 while the other two are always less than 1. Let us choose, by relabelling, z_1 and z_2 to be the ones with absolute values less than 1, therefore we set a_3 and a_4 to be zero. We also note from Eq. (3.28) that for $E = 0$, $U = \pm V$. Therefore, depending on whether $z_1(z_2)$ satisfies $U_1 = V_1(U_2 = V_2)$ or $U_1 = -V_1(U_2 = -V_2)$ we choose $U_1(U_2)$ and $V_1(V_2)$ accordingly. This choice could be made by noting that $U = V$ is satisfied by

$$z_{\pm} = \frac{-\mu_w \pm \sqrt{\mu_w^2 - 4\eta_w^2 + 4\Delta^2}}{2(\eta_w + \Delta)}, \quad (3.49)$$

while $U = -V$ is satisfied by

$$z'_{\pm} = \frac{-\mu_w \pm \sqrt{\mu_w^2 - 4\eta_w^2 + 4\Delta^2}}{2(\eta_w - \Delta)}. \quad (3.50)$$

Thus z_1 and z_2 have to be equal to two of these four roots which have absolute values less

than 1. Fixing $\Delta > 0$, we find that for $|\mu_w| < 2|\eta_w|$, $|z_{\pm}| < 1$ and $|z'_{\pm}| > 1$ while for $|\mu_w| > 2|\eta_w|$, the absolute value one of the roots among z_{\pm} and z'_{\pm} is greater than 1 while the other is less than 1. This implies that for $\Delta > 0$ and $|\mu_w| < 2|\eta_w|$, we need to set $U_1 = V_1$ and $U_2 = V_2$, while for $\Delta > 0$ and $|\mu_w| > 2|\eta_w|$, we have $U_1 = V_1$ and $U_2 = -V_2$.

We first take the case with $\Delta > 0$ and $|\mu_w| < 2|\eta_w|$. For this we have $t_n = t_a = a_3 = a_4 = 0$, $E = 0$, $U_2 = V_1$ and $U_2 = V_2$, which simplify Eq. (3.44) to the set of four equations:

$$i\eta_b r_n + \eta_c U_1 a_1 + \eta_c U_2 a_2 = i\eta_b, \quad (3.51)$$

$$-i\eta_b r_a + \eta_c U_1 a_1 + \eta_c U_2 a_2 = 0, \quad (3.52)$$

$$\eta_c r_n + \kappa_1 U_1 a_1 + \kappa_2 U_2 a_2 = -\eta_c, \quad (3.53)$$

$$\eta_c r_a + \kappa_1 U_1 a_1 + \kappa_2 U_2 a_2 = 0, \quad (3.54)$$

where $\kappa_s = \mu_w + z_s(\eta_w + \Delta)$. These equations can be solved to give $r_n = 0$, $r_a = 1$,

$$U_1 a_1 = \frac{(i\eta_b \kappa_2 + \eta_c^2)}{\eta_c(\kappa_2 - \kappa_1)} \text{ and } U_2 a_2 = -\frac{(i\eta_b \kappa_1 + \eta_c^2)}{\eta_c(\kappa_2 - \kappa_1)}. \quad (3.55)$$

These equations then give the wavefunction of the zero mode that is localized at the left end and can be written as

$$\Psi_L^{MBS}(\alpha) = \begin{pmatrix} 1 \\ 1 \end{pmatrix} \sin \frac{\pi\alpha}{2} \text{ and } \Psi_R^{MBS}(\alpha') = 0, \quad (3.56)$$

$$\Psi_W^{MBS}(j) = \begin{pmatrix} 1 \\ 1 \end{pmatrix} \text{Im} \left[\frac{(i\eta_b \kappa_2 + \eta_c^2) z_1^{j-1} - (i\eta_b \kappa_1 + \eta_c^2) z_2^{j-1}}{\eta_c(\kappa_2 - \kappa_1)} \right]. \quad (3.57)$$

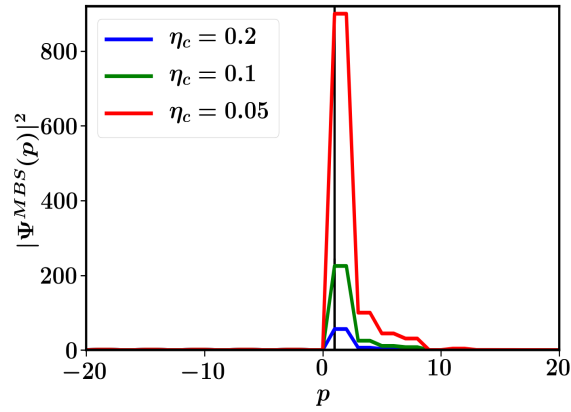
Also, due to the perfect Andreev reflection ($r_a = 1$), we get $G_L(E = 0) = 2$ which marks the zero bias peak found in systems which host MBS[15, 24]. Thus the zero mode found is the wavefunction of the zero energy MBS found to be present in the parameter regime $|\mu_w| < 2|\eta_w|$. Due to the left-right symmetry of the Hamiltonian, the wavefunction of the

MBS localized at the other end of the wire can directly be written as:

$$\Phi_R^{MBS}(\alpha') = \begin{pmatrix} 1 \\ 1 \end{pmatrix} \sin \frac{\pi(N - \alpha')}{2} \text{ and } \Phi_L^{MBS}(\alpha) = 0, \quad (3.58)$$

$$\Phi_W^{MBS}(j) = \begin{pmatrix} 1 \\ 1 \end{pmatrix} \text{Im} \left[\frac{(i\eta_b\kappa_2 + \eta_c^2)z_1^{N-j} - (i\eta_b\kappa_1 + \eta_c^2)z_2^{N-j}}{\eta_c(\kappa_2 - \kappa_1)} \right]. \quad (3.59)$$

The absolute value of the height of the peak in the MBS wavefunction is given by $|\frac{\eta_b}{\eta_c}|$.



(a)

Figure 3.1: Plot of the MBS wavefunction for different couplings with the reservoir at parameter values– $\eta_b = 1.5$, $\mu_w = 0.5$, $\Delta = 0.5$, $\eta_w = 1$. The normalization of these wavefunctions is the same as in Eq. (3.56-3.57) and the vertical black line marks the left end of the wire. Note that the lead wavefunctions are not visible on this scale.

Therefore, the height of the peak decreases as coupling with the bath increases which makes sense since one expects the wavefunction to leak into the reservoir more as the coupling with reservoirs increases. This can be seen in Fig. 3.1 where we plot the MBS wavefunction for a few different couplings with the reservoirs. Also, increasing η_b increases the bandwidth of the system which decreases the density of the states around $E = 0$ and therefore the MBS of the isolated wire hybridizes less with the reservoir wavefunctions as the energy difference between them increases. Note that if the height of the peak in the MBS goes down, the weight of the MBS in the reservoirs increases and vice-versa. We will see later that this wavefunction helps in explaining the behaviour of the zero bias peak with different parameters of the Hamiltonian.

Let us consider the case with $\Delta > 0$ and $|\mu_w| > 2|\eta_w|$. For this we have

$$i\eta_b r_n + \eta_c U_1 a_1 + \eta_c U_2 a_2 = i\eta_b, \quad (3.60)$$

$$-i\eta_b r_a + \eta_c U_1 a_1 - \eta_c U_2 a_2 = 0, \quad (3.61)$$

$$\eta_c r_n + \kappa_1 U_1 a_1 + \kappa_1 U_2 a_2 = -\eta_c, \quad (3.62)$$

$$\eta_c r_a + \kappa_1 U_1 a_1 - \kappa_1 U_2 a_2 = 0. \quad (3.63)$$

These equations can be solved for r_n , r_a , U_1 and U_2 with which we can then construct the zero mode present in this parameter regime. However, these equations give $r_a = 0$ and therefore there is no perfect Andreev reflection ($r_a = 1$). Thus the zero mode constructed out of them would not be the MBS. They would merely be the zero energy states of the left reservoir leaking into the wire. We therefore conclude that only the zero energy states present in the parameter regime $|\mu_w| < 2|\eta_w|$ give rise to the perfect Andreev reflection and are the states representing the MBS of this system. Similar arguments can be repeated for the case $\Delta < 0$.

3.3 Analytical proof of the equivalence of QLE-NEGF and scattering approaches

In this section we will show analytically the equivalence between the two approaches by deriving the following equalities,

$$T_1(E) = |t_n|^2, T_2(E) = |t_a|^2 \quad (3.64)$$

$$\text{and } T_3(E) = T_3(-E) = |r_a|^2 \quad (3.65)$$

where, $T_1(E)$, $T_2(E)$ and $T_3(E)$ are given Eq. (3.19), Eq. (3.20) and Eq. (3.21) respectively with μ_L replaced by E . This would then straight forwardly imply the equivalence of the two conductance expression. To proceed, we first need to find a set of equations relating the transmission amplitudes, t_n and t_a , to the reflection amplitudes, r_n and r_a directly, which is

possible by relating $\begin{pmatrix} \Psi_L(-1) \\ \Psi_L(0) \end{pmatrix}$ directly to $\begin{pmatrix} \Psi_R(N+1) \\ \Psi_R(N+2) \end{pmatrix}$ via transfer matrices. We start by considering the equation for the stationary state of energy E inside the wire

$$A_W^T \Psi_W(j-1) + A \Psi_W(j) + A_W \Psi_W(j+1) = E \Psi_W(j) \quad (3.66)$$

which we re-write in the following recursive form:

$$\begin{pmatrix} A_W^T \Psi_W(j-1) \\ \Psi_W(j) \end{pmatrix} = \Omega_W \begin{pmatrix} A_W^T \Psi_W(j) \\ \Psi_W(j+1) \end{pmatrix}, \quad (3.67)$$

where

$$\Omega_W = \begin{pmatrix} (E-A)A_W^{-T} & -A_W \\ A_W^{-T} & 0 \end{pmatrix}. \quad (3.68)$$

Using the boundary conditions at the left junction, Eq. (3.40) and Eq. (3.41), we can write

$$\begin{pmatrix} \Psi_L(-1) \\ \Psi_L(0) \end{pmatrix} = \Omega_{L1} \Omega_{L2} \begin{pmatrix} A_W^T \Psi_W(1) \\ \Psi_W(2) \end{pmatrix}, \quad (3.69)$$

where

$$\Omega_{L1} = \begin{pmatrix} A_L^{-1} E A_C^{-1} & -A_L^{-1} A_C \\ A_C^{-1} & 0 \end{pmatrix}, \quad (3.70)$$

$$\Omega_{L2} = \Omega_W = \begin{pmatrix} (E-A)A_W^{-T} & -A_W \\ A_W^{-T} & 0 \end{pmatrix}. \quad (3.71)$$

Using Eq. (3.67) repeatedly in Eq. (3.69) we have the following equation:

$$\begin{pmatrix} \Psi_L(-1) \\ \Psi_L(0) \end{pmatrix} = \Omega_{L1} \Omega_{L2} \Omega_W^{N-2} \begin{pmatrix} A_W^T \Psi_W(N-1) \\ \Psi_W(N) \end{pmatrix}. \quad (3.72)$$

Finally, we use the boundary conditions at the right junction, Eq. (3.42) and Eq. (3.43), to obtain the desired equation

$$\begin{pmatrix} \Psi_L(-1) \\ \Psi_L(0) \end{pmatrix} = \Omega_{L1} \Omega_{L2} \Omega_W^{N-2} \Omega_{R2} \Omega_{R1} \begin{pmatrix} \Psi_R(N+1) \\ \Psi_R(N+2) \end{pmatrix} \quad (3.73)$$

$$= \Omega_{L1} \Omega \Omega_{R1} \begin{pmatrix} \Psi_R(N+1) \\ \Psi_R(N+2) \end{pmatrix}, \quad (3.74)$$

where

$$\Omega_{R2} = \begin{pmatrix} E - A & -I \\ I & 0 \end{pmatrix}, \quad (3.75)$$

$$\Omega_{R1} = \begin{pmatrix} A_C^{-T} E & -A_C^{-T} A_R \\ A_C & 0 \end{pmatrix}, \quad (3.76)$$

$$\Omega = \Omega_{L2} \Omega_W^{N-2} \Omega_{R2}, \quad (3.77)$$

and I denotes a 2×2 unit matrix. We now have Eq. (3.74) which relates $\begin{pmatrix} \Psi_L(-1) \\ \Psi_L(0) \end{pmatrix}$ directly to $\begin{pmatrix} \Psi_R(N+1) \\ \Psi_R(N+2) \end{pmatrix}$ via the transfer matrix, $\Omega_{L1} \Omega \Omega_{R1}$. This equation will furnish a set of four equations for r_n , r_a , t_n and t_a after using the forms of $\Psi_L(\alpha)$ and $\Psi_R(\alpha')$ from Eq. (3.37) and Eq. (3.39) respectively. However, we could make things much more simpler by using the forms of the matrices A_C , A_L and A_R to write

$$\Omega_{L1} = \frac{1}{\eta_b \eta_c} \begin{pmatrix} E & -\eta_c^2 \\ -\eta_b \sigma^z & 0 \end{pmatrix}, \quad (3.78)$$

$$\Omega_{L1}^{-1} = \frac{1}{\eta_c} \begin{pmatrix} 0 & -\eta_c^2 \sigma^z \\ -\eta_b & -E \sigma^z \end{pmatrix}, \quad (3.79)$$

$$\text{and } \Omega_{R1} = \frac{1}{\eta_c} \begin{pmatrix} -E \sigma^z & -\eta_b \\ -\eta_c^2 \sigma^z & 0 \end{pmatrix}, \quad (3.80)$$

where $\sigma^z = \begin{pmatrix} 1 & 0 \\ 0 & -1 \end{pmatrix}$. Now, from Eq. (3.74) we have

$$\Omega_{L1}^{-1} \begin{pmatrix} \Psi_L(-1) \\ \Psi_L(0) \end{pmatrix} = \Omega \Omega_{R1} \begin{pmatrix} \Psi_R(N+1) \\ \Psi_R(N+2) \end{pmatrix}, \quad (3.81)$$

which then gives the following two matrix equations:

$$\begin{aligned} \eta_c^2 \sigma^z \Psi_L(0) &= \bar{\Omega}_{11} [E \sigma^z \Psi_R(N+1) + \eta_b \Psi_R(N+2)] \\ &\quad + \bar{\Omega}_{12} \eta_c^2 \sigma^z \Psi_R(N+1), \end{aligned} \quad (3.82)$$

$$\begin{aligned} \eta_b \Psi_L(-1) + E \sigma^z \Psi_L(0) &= \bar{\Omega}_{21} E \sigma^z \Psi_R(N+1) \\ &\quad + \bar{\Omega}_{21} \eta_b \Psi_R(N+2) + \bar{\Omega}_{22} \eta_c^2 \sigma^z \Psi_R(N+1), \end{aligned} \quad (3.83)$$

where $\bar{\Omega}_{ij}$ are 2×2 matrices that form blocks of the matrix Ω , *i.e.*

$$\Omega = \begin{pmatrix} \bar{\Omega}_{11} & \bar{\Omega}_{12} \\ \bar{\Omega}_{21} & \bar{\Omega}_{22} \end{pmatrix}. \quad (3.84)$$

Using the forms of $\Psi_L(\alpha)$ and $\Psi_R(\alpha')$ from Eq. (3.37) and Eq. (3.39) respectively, Eq. (3.82) and Eq. (3.83) can be written as

$$\begin{aligned} \eta_c^2(|+\rangle + r_n|+\rangle - r_a|-\rangle) = \\ [-\eta_b e^{-iq} \bar{\Omega}_{11} + \eta_c^2 \bar{\Omega}_{12}] [t_n|+\rangle - t_a|-\rangle], \end{aligned} \quad (3.85)$$

$$\begin{aligned} -\eta_b(e^{iq}|+\rangle + e^{-iq}r_n|+\rangle - e^{-iq}r_a|-\rangle) = \\ [-\eta_b e^{-iq} \bar{\Omega}_{21} + \eta_c^2 \bar{\Omega}_{22}] [t_n|+\rangle - t_a|-\rangle], \end{aligned} \quad (3.86)$$

where we substituted $q - \pi$ for q' , $|\pm\rangle$ is the eigenvector of σ^z with eigenvalue ± 1 . We can simultaneously get rid of r_n and r_a by subtracting Eq. (3.85) and Eq. (3.86) after multiplication with appropriate factors. Thus, one finds:

$$-2ie^{iq} \sin q |+\rangle = \frac{\eta_b}{\eta_c^2} \mathcal{O} [t_n|+\rangle - t_a|-\rangle], \quad (3.87)$$

where

$$\mathcal{O} = \left[-e^{-2iq} \bar{\Omega}_{11} + \frac{\eta_c^2}{\eta_b} e^{-iq} \bar{\Omega}_{12} - \frac{\eta_c^2}{\eta_b} e^{-iq} \bar{\Omega}_{21} + \frac{\eta_c^4}{\eta_b^2} \bar{\Omega}_{22} \right]. \quad (3.88)$$

From Eq. (3.87) we can write down the two equations for t_n and t_a :

$$1 = -\frac{t_n}{2i \frac{\eta_c^2}{\eta_b} \sin q} \langle + | \mathcal{O} | + \rangle + \frac{t_a}{2i \frac{\eta_c^2}{\eta_b} \sin q} \langle + | \mathcal{O} | - \rangle, \quad (3.89)$$

$$0 = -\frac{t_n}{2i \frac{\eta_c^2}{\eta_b} \sin q} \langle - | \mathcal{O} | + \rangle + \frac{t_a}{2i \frac{\eta_c^2}{\eta_b} \sin q} \langle - | \mathcal{O} | - \rangle. \quad (3.90)$$

Also, from Eq. (3.86) we directly get an expression of r_a in terms of t_n and t_a :

$$\begin{aligned} r_a = & \left[-\langle - | \bar{\Omega}_{21} | + \rangle + e^{iq} \frac{\eta_c^2}{\eta_b} \langle - | \bar{\Omega}_{22} | + \rangle \right] t_n \\ & - \left[-\langle - | \bar{\Omega}_{21} | - \rangle + e^{iq} \frac{\eta_c^2}{\eta_b} \langle - | \bar{\Omega}_{22} | - \rangle \right] t_a. \end{aligned} \quad (3.91)$$

For the moment we leave this here and turn our attention to the terms in the NEGF-expression for conductance. From Eq. (3.19-3.21) we see that $T_1(E)$, $T_2(E)$ and $T_3(E)$ are essentially given by the elements $[G_1^+(E)]_{1N}$, $[G_2^+(E)]_{1N}$ and $[G_2^+(E)]_{11}$ of the two Green's

functions. We note that given the forms of the Green's functions $G_1^+(\omega)$ and $G_2^+(\omega)$, it is not easy to obtain these elements. Therefore, we have to re-write these Green's functions in some other form so that these elements could be obtained analytically. For that, we consider the Fourier transformed Langevin equations of motion for the wire, Eq. (2.26), and write its solution in a slightly different form involving a single $2N \times 2N$ Greens function. We start with the equations

$$[\Pi(\omega)]_{lm}\tilde{c}_m(\omega) - K_{lm}\tilde{c}_m^\dagger(-\omega) = \tilde{\eta}_l^L(\omega) + \tilde{\eta}_l^R(\omega), \quad (3.92)$$

$$[\Pi(-\omega)]_{lm}^*\tilde{c}_m^\dagger(-\omega) - K_{lm}^*\tilde{c}_m(\omega) = \tilde{\eta}_l^{L\dagger}(-\omega) + \tilde{\eta}_l^{R\dagger}(-\omega). \quad (3.93)$$

Defining the two component vectors

$$C_i(\omega) = \begin{pmatrix} \tilde{c}_i(\omega) \\ \tilde{c}_i^\dagger(-\omega) \end{pmatrix} \text{ and } \xi_i(\omega) = \begin{pmatrix} -\tilde{\eta}_i^L(\omega) - \tilde{\eta}_i^R(\omega) \\ \tilde{\eta}_i^{L\dagger}(-\omega) + \tilde{\eta}_i^{R\dagger}(-\omega) \end{pmatrix},$$

we write Eq. (3.92) and Eq. (3.93) together as $[\mathcal{G}^{-1}(\omega)]_{lm}C_m(\omega) = \xi_l(\omega)$ which has the solution:

$$C_l(\omega) = [\mathcal{G}(\omega)]_{lm}\xi_m(\omega), \quad (3.94)$$

with $\mathcal{G}^{-1}(\omega)$ being a $2N \times 2N$ matrix whose lm -th 2×2 matrix block element is given by

$$[\mathcal{G}^{-1}(\omega)]_{lm} = \begin{pmatrix} -[\Pi(\omega)]_{lm} & K_{lm} \\ -K_{lm}^* & [\Pi(-\omega)]_{lm}^* \end{pmatrix} \quad (3.95)$$

Comparing Eq. (3.94) with Eq. (2.33) for the $\tilde{c}_m(\omega)$ we see that

$$[\mathcal{G}(\omega)]_{lm} = \begin{pmatrix} -[G_1^+(\omega)]_{lm} & [G_2^+(\omega)]_{lm} \\ -[G_2^+(-\omega)]_{lm}^* & [G_1^+(-\omega)]_{lm}^* \end{pmatrix}. \quad (3.96)$$

Now, from Eq. (3.17) and Eq. (3.95) we find that the matrix $\mathcal{G}(E)$ has the following structure:

$$\mathcal{G}(E) = \left(\begin{array}{cccccccc} -E + A - A_\Sigma & A_W & 0 & 0 & \dots & 0 & 0 & \\ A_W^T & -E + A & A_W & 0 & \dots & 0 & 0 & \\ 0 & A_W^T & -E + A & A_W & \dots & 0 & 0 & \\ \vdots & \vdots & \vdots & \ddots & & \vdots & \vdots & \\ \vdots & \vdots & \vdots & & \ddots & \vdots & \vdots & \\ \vdots & \vdots & \vdots & \dots & A_W^T & -E + A & A_W & \\ 0 & 0 & 0 & \dots & \dots & A_W^T & -E + A - A_\Sigma & \end{array} \right)^{-1} \quad (3.97)$$

where $A_\Sigma = \begin{pmatrix} -\eta_c^2 \Sigma(E) & 0 \\ 0 & \eta_c^2 \Sigma^*(-E) \end{pmatrix}$, $\Sigma(E)$ being given by Eq. (3.18) with μ_L replaced by E , and the matrices A , A_W defined as in Eq. (3.26). We note that for $|E| < 2\eta_b$, $-\eta_b \Sigma(E) = \eta_b \Sigma^*(-E) = e^{iq}$. This then simplifies A_Σ to be $\frac{\eta_c^2}{\eta_b} e^{iq} I_2$ with I_2 being a 2×2 identity matrix. We work in the regime of $|E| < 2\eta_b$ as outside of it the conductance is zero. Note that $\mathcal{G}(E) = \mathcal{G}^T(E)$ and therefore, we have

$$[G_1^+(E)]^T = G_1^+(E) \quad (3.98)$$

$$G_2^-(-E) = -G_2^+(E). \quad (3.99)$$

These relations would be useful later on. The block tri-diagonal structure of $\mathcal{G}(E)$ in Eq. (3.97) allows us to find the required elements of $\mathcal{G}(E)$, which are \mathcal{G}_{N1} and \mathcal{G}_{11} , for obtaining the terms in NEGF-expression for conductance. Thus, we define I_{2N} to be a $2N \times 2N$ identity matrix so that, using the first column of equations from the identity $\mathcal{G}^{-1}(E)\mathcal{G}(E) = I_{2N}$, we can write

$$(-E + A - A_\Sigma)\mathcal{G}_{11} + A_W\mathcal{G}_{21} = I_2 \quad (3.100)$$

$$A_W^T\mathcal{G}_{i-1,1} + (-E + A)\mathcal{G}_{i1} + A_W\mathcal{G}_{i+1,1} = 0 \text{ for } 1 < i < N \quad (3.101)$$

$$A_W^T\mathcal{G}_{N-1,1} + (-E + A - A_\Sigma)\mathcal{G}_{N1} = 0 \quad (3.102)$$

We rewrite these equations as a recursion relation, following similar steps as we did for

Eq. (3.74), to obtain

$$\begin{pmatrix} -I_2 \\ \mathcal{G}_{11} \end{pmatrix} = \Omega_1 \Omega_W^{N-2} \Omega_2 \begin{pmatrix} \mathcal{G}_{N1} \\ 0 \end{pmatrix} \quad (3.103)$$

with Ω_W given by Eq. (3.68),

$$\Omega_1 = \begin{pmatrix} (E - A + A_\Sigma) A_W^{-T} & -A_W \\ A_W^{-T} & 0 \end{pmatrix} = \begin{pmatrix} 1 & A_\Sigma \\ 0 & 1 \end{pmatrix} \Omega_{L2}, \quad (3.104)$$

$$\Omega_2 = \begin{pmatrix} E - A + A_\Sigma & 1 \\ 1 & 0 \end{pmatrix} = \Omega_{R2} \begin{pmatrix} 1 & 0 \\ -A_\Sigma & -1 \end{pmatrix}, \quad (3.105)$$

where Ω_{L2} and Ω_{R2} are the same matrices defined in the scattering calculation by Eq. (3.71) and Eq. (3.75) respectively. Using Eq. (3.104), Eq. (3.105) and substituting $A_\Sigma = \frac{\eta_c^2}{\eta_b} e^{iq} I_2$, one can express Eq. (3.103) as

$$\begin{pmatrix} I_2 \\ \mathcal{G}_{11} \end{pmatrix} = \begin{pmatrix} e^{2iq} \mathcal{O} & \bar{\Omega}_{12} + \frac{\eta_b}{\eta_c^2} e^{iq} \bar{\Omega}_{22} \\ \bar{\Omega}_{21} - \frac{\eta_b}{\eta_c^2} e^{iq} \bar{\Omega}_{22} & -\bar{\Omega}_{22} \end{pmatrix} \begin{pmatrix} \mathcal{G}_{N1} \\ 0 \end{pmatrix}, \quad (3.106)$$

where \mathcal{O} is given by Eq. (3.88). From the upper block of Eq. (3.106), we obtain the following matrix equation for $[G^+(E)]_{N1}$ and $[G_2^+(-E)]_{N1}^*$:

$$|+\rangle = -e^{2iq} \mathcal{O} \left[[G_1^+(E)]_{N1} |+\rangle + [G_2^+(-E)]_{N1}^* |-\rangle \right]. \quad (3.107)$$

which gives two linear equations for $[G^+(E)]_{N1}$ and $[G_2^+(-E)]_{N1}^*$:

$$1 = -e^{2iq} [G_1^+(E)]_{N1} \langle + | \mathcal{O} | + \rangle - e^{2iq} [G_2^+(-E)]_{N1}^* \langle + | \mathcal{O} | - \rangle \quad (3.108)$$

$$0 = -e^{2iq} [G_1^+(E)]_{N1} \langle - | \mathcal{O} | + \rangle - e^{2iq} [G_2^+(-E)]_{N1}^* \langle - | \mathcal{O} | - \rangle. \quad (3.109)$$

Comparing these with Eq. (3.89 and 3.90) and noticing that $\sin q = \eta_b g(E)$ we have

$$2i\eta_c^2 g(E) [G_1^+(E)]_{N1} = e^{-2iq} t_n, \quad (3.110)$$

$$2i\eta_c^2 g(E) [G_2^+(-E)]_{N1}^* = -e^{-2iq} t_a. \quad (3.111)$$

These equations, along with Eq. (3.98 and 3.99) imply that

$$T_1(E) = 4\eta_c^4 g^2(E) |[G_1^+(E)]_{1N}|^2 = |t_n|^2, \quad (3.112)$$

$$T_2(E) = 4\eta_c^4 g^2(E) |[G_2^+(E)]_{1N}|^2 = |t_a|^2, \quad (3.113)$$

which are the required relations. If we consider the lower block equations of Eq. (3.106), then one of the component equation reads

$$\begin{aligned} [G_2^+(-E)]_{11}^* &= \left[\langle - | \bar{\Omega}_{21} | + \rangle - e^{iq} \frac{\eta_c^2}{\eta_b} \langle - | \bar{\Omega}_{22} | + \rangle \right] [G_1^+(E)]_{N1} \\ &+ \left[\langle - | \bar{\Omega}_{21} | - \rangle - e^{iq} \frac{\eta_c^2}{\eta_b} \langle - | \bar{\Omega}_{22} | - \rangle \right] [G_2^+(-E)]_{N1}^*. \end{aligned} \quad (3.114)$$

We replace $[G_1^+(E)]_{N1}$ and $[G_2^+(-E)]_{N1}^*$ for t_n and t_a in this equation with the help of Eq. (3.110, 3.111). Comparing the resulting equation with Eq. (3.91) and using Eq. (3.99), we finally obtain

$$T_3(E) = T_3(-E) = 4\eta_c^4 g^2(E) |[G_2^+(E)]_{11}|^2 = |r_a|^2. \quad (3.115)$$

This completes the analytic proof for the equivalence.

3.4 Conclusion

In conclusion, we provided an analytical proof of the equivalence of the QLE-NEGF approach and the scattering approach to electron transport in a 1-D superconducting wire. In both cases we start from the same microscopic model of a Kitaev wire connected to one-dimensional leads (baths) containing free fermions in equilibrium. In the former method one starts with the Heisenberg equations of motion of the full system and eliminates the bath degrees of freedom to obtain effective quantum Langevin equations of motion. The steady state solution of these leads to the NEGF formula for the conductance in terms of a set of nonequilibrium Green's functions. In the second approach one considers the wire

as a scatterer of plane waves from the leads and writes down the corresponding scattering solutions for the energy eigenstates. These solutions involve scattering amplitudes that are obtained using the boundary conditions at the wire-leads junctions. The conductance at the junction is then given by the net probability of transmission of particles across the junction.

We summarize here our some of the main results:

- We obtained the complete solution of the scattering states in the Kitaev chain, including closed form expressions for the scattering amplitudes t_a, t_n, r_n, r_a .
- We obtained the special zero energy solution corresponding to the MBS state of the isolated open Kitaev chain. We showed that this state exists in the same parameter regime as for the isolated wire.
- The conductance of the wire from the QLE-NEGF method and the scattering approach are given respectively by Eq. (3.12) and Eq. (3.22). We showed analytically that the terms in the NEGF conductance expression, $T_1(E)$, $T_2(E)$ and $T_3(E)$, can be related to the scattering amplitudes t_n, t_a and r_a respectively. This leads us to proving the complete equivalence of the two formulas for conductance and hence of the two approaches.
- We have demonstrated clearly and explicitly the physical interpretation— from our derivation we see that the expression for current, Eq. (5.46), is exactly in Landauer’s form with each of the baths playing the role of a ”double reservoir”, of electrons and holes. The wire acts as a scatterer and scatters the incoming electrons as holes or electrons into the two baths. Therefore, an electron from say the left bath may end up being scattered as a hole or an electron into the left bath only. These two processes are the normal reflection and Andreev reflection processes respectively. The electron may also end up being scattered into the right reservoir, therefore transmitted across the wire, as an electron or a hole. Out of the four possibilities of the future of an electron from the left bath, all excepting the normal reflection lead to particles being transmitted across the left junction. Therefore, only these three actually contribute to

the conductance of the wire. This is the reason behind the NEGF current expression having three distinct terms with the probabilities of these processes multiplied with the corresponding difference of thermal occupations of the incoming electrons and outgoing electron or holes as one typically finds in Landauer expressions.

Chapter 4

Quantized two-terminal longitudinal conductance and edge states in an open geometry 2-dimensional Chern insulator

Consider a strip of an insulator with non-trivial topology connected to metallic leads at two opposite edges, with a voltage difference V applied across the leads. An interesting question is regarding the quantization of the longitudinal two-terminal conductance, G . The presence of the perfectly conducting edge modes suggests the possibility of quantization, but this is not so obvious when one considers that the contacts with the leads need not be perfect and there could be scattering of incident waves. A proof (similar to TKNN) [29] of the quantization of the longitudinal conductance in the open system setup would be desirable but, to the best of our knowledge, remains an open problem. The quantization of the longitudinal conductance can be argued to be the same as the transverse conductance in a four-probe measurement setup based on the Landauer-Buttiker formalism, assuming perfect transmission via edge modes and quantized conductance, e^2/h , of the point contacts [8, 66, 67]. Under this assumption, in the four-probe measurement setup, the longitudinal voltage

drop is equal to the transverse voltage drop. This makes the transverse conductance the same as the longitudinal conductance and therefore quantized. However, it is not very clear as to what is required to achieve perfect point contacts. It is not obvious that the assumption of perfect transmission can be seen to hold in a more microscopic approach such as the non-equilibrium Green's function (NEGF) formalism, where the transmission is explicitly related to the details of the reservoir model and its coupling with the system. An interesting question is whether the details of the reservoir and the coupling become irrelevant as one takes the thermodynamic limit and one always sees a perfect transmission. In fact, a few numerical studies based on the NEGF formalism have considered aperiodic 2D topological insulators sandwiched between two metallic leads and find the longitudinal conductance to be quantized [17, 18, 19].

In this chapter, we attempt to arrive at a better understanding of the two-terminal longitudinal conductance in the open system by use of the NEGF formalism. We consider the spinless BHZ (SBHZ) model [47], a Chern insulator, placed in contact with two normal metallic leads. Apart from measuring the conductance obtained from NEGF, we use this formalism to also extract information on the scattering states formed by the edge modes *in the presence of the leads*. The strip geometry makes this a highly non-trivial problem. In particular, for the scattering states, we obtain the current and charge density profiles inside the insulating region as well as in the metallic leads.

In Sec. 4.1, we define the model of the SBHZ wire in contact with semi-infinite metallic leads. We also discuss briefly the isolated SBHZ model and discuss some of its features. We conclude this section by discussing the conductance, current density, and the charge density in the open system geometry within the NEGF formalism. In Sec. 4.2, we present our numerical results on the conductance, current density, and the charge density of the edge modes. We conclude in Sec. 4.3.

4.1 The model and the NEGF results for Conductance, charge and current density

4.1.1 The open system setup

The SBHZ model is a simple 2D topological insulator given by a nearest neighbor tight-binding Hamiltonian on a square lattice. Each site has two fermionic degrees of freedom. Let us call the creation and annihilation operators of these degrees of freedom as $\psi_1(x, y)$, $\psi_1^\dagger(x, y)$ and $\psi_2(x, y)$, $\psi_2^\dagger(x, y)$ respectively. The integers $x = 1, 2, \dots, N_x$ and $y = 1, 2, \dots, N_y$ label the position of the sites on a $N_x \times N_y$ rectangular lattice. The operators $\psi_1(x, y)$ and $\psi_2(x, y)$ follow the usual fermionic anti-commutation relation. We consider the system in contact with two external reservoirs at the two opposite edges at $x = 1$ and $x = N_x$. The two reservoirs are taken to be metallic leads that are semi-infinite in the x -direction and of width N_y in the y -direction and modeled as 2D tight-binding Hamiltonians which we refer to as \mathcal{H}_L and \mathcal{H}_R . We take two fermionic degrees of freedom on each site in the two reservoirs as well. We label the corresponding annihilation operators as $\psi_{1,L/R}(x_{L/R}, y)$ and $\psi_{2,L/R}(x_{L/R}, y)$, where L and R label the left and the right lead, respectively. The integers x_L and x_R label the x coordinates of the sites on the left and the right reservoirs, respectively. These take integer values that run from $-\infty$ to 0 and $N_x + 1$ to ∞ , respectively. The y coordinate here takes the same integer values as in the wire (SBHZ insulator) i.e. from 1 to N_y . Free boundary conditions are imposed at the edges of the reservoir and the system at $y = 1$ and $y = N_y$ respectively. The contacts are themselves modelled as tight-binding Hamiltonians, \mathcal{H}_{WL} and \mathcal{H}_{WR} . The full Hamiltonian of the system and baths is therefore given by:

$$\mathcal{H} = \mathcal{H}_L + \mathcal{H}_{WL} + \mathcal{H}_W + \mathcal{H}_{WR} + \mathcal{H}_R, \quad (4.1)$$

where \mathcal{H}_W is the Hamiltonian of the SBHZ-model and

$$\mathcal{H}_W = \sum_{x,x'=1}^{N_x} \sum_{y,y'=1}^{N_y} \Psi^\dagger(x, y) H_W[x, y; x', y'] \Psi(x', y'), \quad (4.2a)$$

$$\mathcal{H}_L = \sum_{x_L, x'_L=-\infty}^0 \sum_{y, y'=1}^{N_y} \Psi_L^\dagger(x_L, y) H_L[x_L, y; x'_L, y'] \Psi_L(x'_L, y'), \quad (4.2b)$$

$$\mathcal{H}_R = \sum_{x_R, x'_R=N_x+1}^{\infty} \sum_{y, y'=1}^{N_y} \Psi_R^\dagger(x_R, y) H_R[x_R, y; x'_R, y'] \Psi_R(x'_R, y'), \quad (4.2c)$$

$$\mathcal{H}_{WL} = \sum_{x_L=-\infty, x=1}^{0, N_x} \sum_{y, y'=1}^{N_y} \Psi_L^\dagger(x_L, y) V_L[x_L, y; x, y'] \Psi(x, y') + h.c., \quad (4.2d)$$

$$\mathcal{H}_{WR} = \sum_{x_R=N_x+1, x=1}^{\infty, N_x} \sum_{y, y'=1}^{N_y} \Psi_R^\dagger(x_R, y) V_R[x_R, y; x, y'] \Psi(x, y') + h.c.. \quad (4.2e)$$

Here we have defined the two-vectors $\Psi(x, y) = \begin{pmatrix} \psi_1(x, y) & \psi_2(x, y) \end{pmatrix}^T$ and $\Psi_{L/R}(x, y) = \begin{pmatrix} \psi_{1,L/R}(x, y) & \psi_{2,L/R}(x, y) \end{pmatrix}^T$. The 2×2 matrices, $H_W[x, y; x', y']$, $H_{L/R}[x_{L/R}, y; x'_{L/R}, y']$, $V_{L/R}[x, y; x', y']$ are given by:

$$H_W[x, y; x', y'] = \mu_w I_2 \delta_{xx'} \delta_{yy'} + \frac{\sigma_z - i\sigma_x}{2} \delta_{x, x'+1} \delta_{yy'} \theta(x' < N_x) + \frac{\sigma_z + i\sigma_x}{2} \delta_{x+1, x'} \delta_{yy'} \theta(x < N_x) \\ + \frac{\sigma_z - i\sigma_y}{2} \delta_{y, y'+1} \delta_{xx'} \theta(y' < N_y) + \frac{\sigma_z + i\sigma_y}{2} \delta_{y+1, y'} \delta_{xx'} \theta(y < N_y), \quad (4.3a)$$

$$H_L[x_L, y; x'_L, y'] = \eta_b I_2 (\delta_{x_L-1, x'_L} \delta_{yy'} + \delta_{x_L, x'_L-1} \delta_{yy'} + \delta_{y, y'+1} \delta_{x_L x'_L} \theta(y' < N_y) + \delta_{y+1, y'} \delta_{x_L x'_L} \theta(y < N_y)), \quad (4.3b)$$

$$H_R[x_R, y; x'_R, y'] = \eta_b I_2 (\delta_{x_R, x'_R+1} \delta_{yy'} + \delta_{x_R+1, x'_R} \delta_{yy'} + \delta_{y, y'+1} \delta_{x_R x'_R} \theta(y' < N_y) + \delta_{y+1, y'} \delta_{x_R x'_R} \theta(y < N_y)), \quad (4.3c)$$

$$V_L[x_L, y; x, y'] = \eta_c I_2 \delta_{x_L, 0} \delta_{x, 1} \delta_{yy'} \quad \text{and} \quad V_R[x_R, y; x, y'] = \eta_c I_2 \delta_{x_R, N_x+1} \delta_{x, N_x} \delta_{yy'}, \quad (4.3d)$$

where $\theta(m < n)$ is an indicator function which is 1 if $m < n$ and zero otherwise. These functions impose free boundary conditions at the edges of the SBHZ wires and the reservoirs. We have taken σ_z , σ_x and σ_y to be the usual Pauli matrices while I_2 is a 2×2

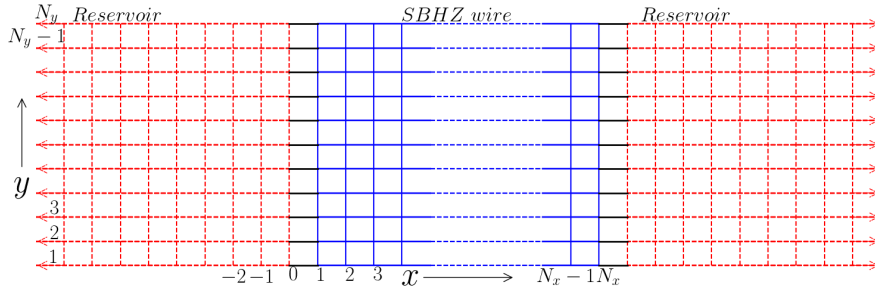


Figure 4.1: Schematic of the SBHZ wire connected to metallic leads

identity matrix. The elements in the above equations can be represented in the form of matrices, H_W , $H_{L/R}$ and $V_{L/R}$, of size $2N_x \times N_y$ and components given by $H_W[x, y, a; x', y', b]$, $H_{L/R}[x_{L/R}, y, a; x'_{L/R}, y', b]$ and $V_{L/R}[x_{L/R}, y, a; x, y', b]$ respectively. The indices a, b take values 1, 2 referring to the two degrees of freedom on each site. A schematic representing the SBHZ wire in the open system geometry is given in Fig (4.1).

We now proceed to discuss some of the features of the eigenspectrum and eigenstates in the isolated SBHZ wire before discussing, in Sec. 4.1.3, the NEGF results for the conductance and profiles of current and density in the open geometry.

4.1.2 Isolated SBHZ wire

The bulk spectrum, for the infinite SBHZ system, can be computed by a simple Fourier transform. In Fourier space, the Hamiltonian is given by

$$H(k_x, k_y) = \sigma_x \sin k_x + \sigma_y \sin k_y + \sigma_z (\mu_w - \cos k_x - \cos k_y), \quad (4.4)$$

where k_x and k_y are wave numbers in x and y direction respectively. Therefore, the spectrum and the corresponding eigenstates are given by

$$\epsilon(k_x, k_y) = \pm \sqrt{\sin^2 k_x + \sin^2 k_y + (\mu_w - \cos k_x - \cos k_y)^2}, \quad (4.5)$$

$$\Psi(x, y) = \frac{1}{4\pi^2} \int_{-\pi}^{\pi} \int_{-\pi}^{\pi} dk_x dk_y \tilde{\Psi}(k_x, k_y) e^{i(k_x x + k_y y)}, \quad (4.6)$$

where $\tilde{\Psi}(k_x, k_y)$ is a two-vector such that $H(k_x, k_y)\tilde{\Psi}(k_x, k_y) = \epsilon(k_x, k_y)\tilde{\Psi}(k_x, k_y)$. From the bulk spectrum and the eigenstates, the Chern number can be computed, and it turns out to be 1 for $-2 < \mu_w < 0$, -1 for $0 < \mu_w < 2$ and zero otherwise [47]. We also consider the spectrum of the model with finite size and free boundary conditions at the edges. This spectrum is obtained by numerically diagonalizing the matrix, H_W . For the non-zero Chern number parameter regimes, the finite-size system will host mid-gap modes localized at the edges of the model. This can be seen from Fig. (4.2a) and Fig. (4.2b) where we plot the bulk and the finite size spectrum at different values of μ_w respectively. We see that the gap is filled with states in the finite size spectrum, shown in blue, in the topologically non-trivial regime, $-2 < \mu_w < 2$. These are the edge modes, some of which we plot in Fig (4.2c).

4.1.3 NEGF results for the non-equilibrium steady state

The SBHZ model is a tight-binding model without the superconducting pairing. We can therefore use the results of Sec. 2.3 with the superconducting pairing set to zero. Therefore the effective Green's function for the wire is given by,

$$G_1^+(\omega) = \mathcal{G}^+(\omega) = \frac{1}{\omega - H_W - \Sigma_L(\omega) - \Sigma_R(\omega)}, \text{ and } G_2^+(\omega) = 0 \quad (4.7)$$

where

$$\Sigma_{L/R}(\omega) = V_{L/R}^\dagger \frac{1}{\omega - H_{L/R}} V_{L/R}. \quad (4.8)$$

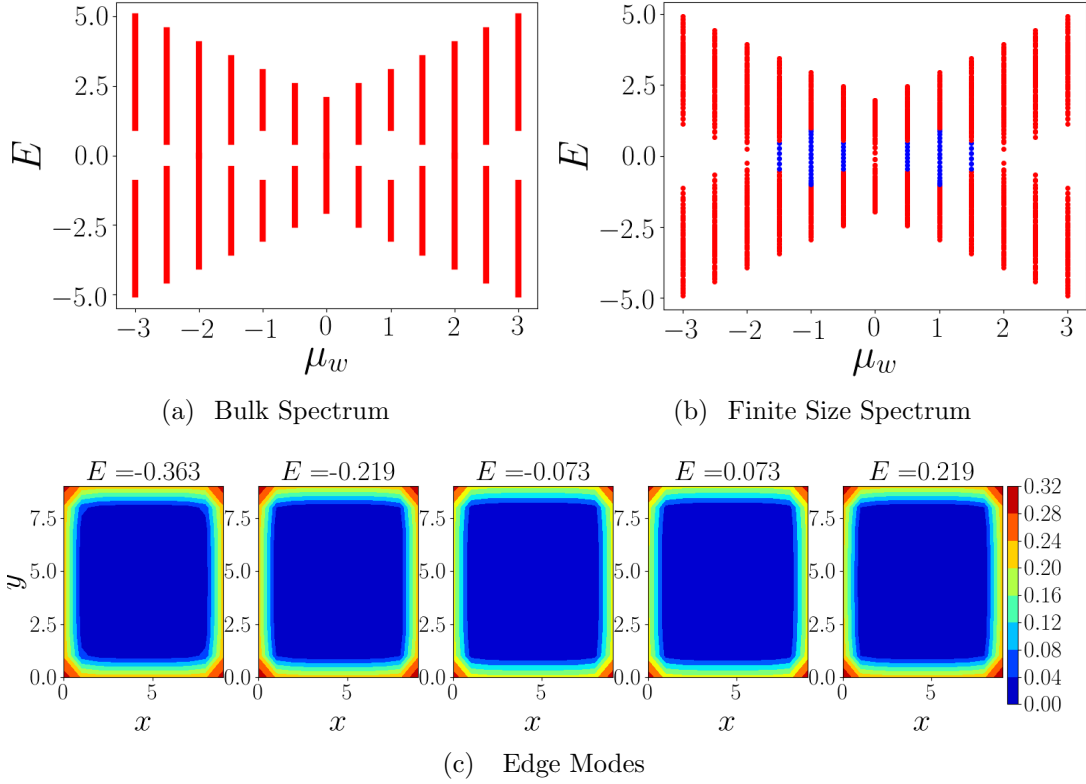


Figure 4.2: (a) and (b) Bulk Spectrum and finite size ($N_x = N_y = 10$) spectrum, with free boundary conditions at the edges, of the BHZ model at different μ_w respectively. (c) is a contour plot of some of the edge states that appear of the finite size spectrum with $\mu_w = 1$ where the Chern number is known to be -1 . The energy values of the states are printed on the top of each sub-panel in (c).

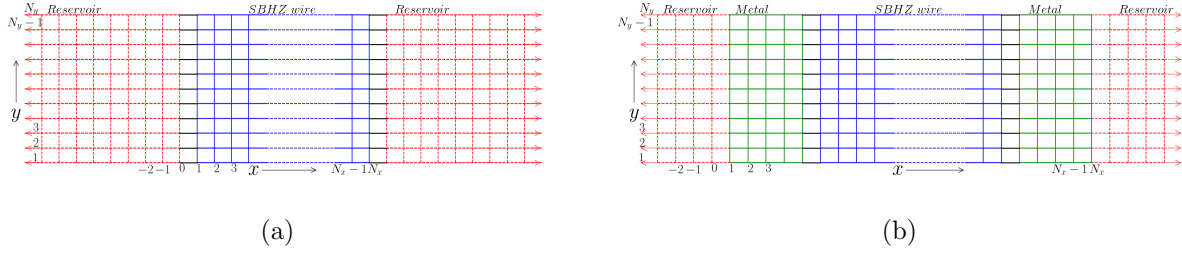


Figure 4.3: Schematic of two geometries used for the calculation of the current density in the SBHZ wire and the reservoirs. The red regions are the reservoirs. The green region is the normal metallic region with a Hamiltonian identical to the reservoirs. The blue region is the SBHZ wire.

Two terminal conductance

The current entering the wire from the left lead, in units with $e = h = 1$,

$$J_L = \int d\omega G(\omega) [f(\omega, \mu_L, T_L) - f(\omega, \mu_R, T_R)], \quad (4.9)$$

where $f(\omega, \mu, T)$ is the Fermi distribution function and

$$G(\omega) = 4\pi^2 \text{Tr} [\mathcal{G}^+(\omega) \Gamma_R(\omega) \mathcal{G}^-(\omega) \Gamma_L(\omega)]. \quad (4.10)$$

$G(\omega)$ is the transmission function and can be interpreted as the scattering amplitude of the scattering process where an electron from the left reservoir is transmitted into the right reservoir. Setting $T_L = T_R = 0$, $\mu_L = \mu + \Delta\mu/2$ and $\mu_R = \mu - \Delta\mu/2$, this current expression reduces to, $J_L = G(\mu)\Delta\mu$. Therefore, $G(\mu)$ directly gives the conductance of the reservoir at energy, μ .

Charge and current density

The charge density and the current density can be computed from the correlation matrix, C with components given by,

$$C[x, y, a; x', y', b] = \langle \psi_a^\dagger(x, y) \psi_b(x', y') \rangle; \quad a, b = 1, 2, \quad (4.11)$$

where the expectation value is taken in the non-equilibrium steady state. From Sec 2.3, this is given by

$$C = \int_{-\infty}^{\infty} d\omega [C_L(\omega)f(\omega, \mu_L, T_L) + C_R(\omega)f(\omega, \mu_R, T_R)], \quad (4.12)$$

where $C_L(\omega)$ and $C_R(\omega)$ are given by,

$$C_{L/R}(\omega) = \mathcal{G}^+(\omega)\Gamma_{L/R}(\omega)\mathcal{G}^-(\omega). \quad (4.13)$$

The charge density and the current density are given in terms of C as follows:

$$\rho_a(x, y) = C[x, y, a; x, y, a], \quad (4.14)$$

$$\mathcal{J}[x, y; x', y'] = 4\pi \sum_{a,b=1}^2 \text{Im} \left[H_W[x, y, a; x', y', b]C[x, y, a; x', y', b] \right]. \quad (4.15)$$

$\mathcal{J}[x, y; x', y']$ is the net particle current on the bond between the lattice point (x, y) and (x', y') . Clearly, it is zero if the two are not nearest neighbors on the square lattice.

We note that while Eq. (4.15) gives us the current density inside the system, it is slightly more non-trivial to obtain the current density in the reservoirs. However, with a simple modification of the geometry of the system, the NEGF formalism can still be used to compute the current density in the reservoirs. The main point to note is that in the NESS of the full system and reservoirs, the state inside the reservoirs has also evolved and in fact contains information about the scattering states (plane waves incident from either reservoir onto the scattering region formed by the insulator). To see the steady state profile inside the reservoirs, we simply consider a setup that consists of the insulator sandwiched between finite metallic segments, which are in turn connected to the reservoirs (again formed by metals). In Fig (4.3), we show a schematic, of the original and of the modified setups, where the red regions correspond to the left and right reservoirs, green regions are normal metallic regions and the blue region is the Chern insulator. However, in the new setup, we can now use NEGF to compute current everywhere inside the system, including the metallic sites. The current density in the normal metallic region would be identical to that in the reservoirs

in the original setup because of the uniqueness of the NESS.

For $T_L = T_R = 0$, $\mu_L = \mu + \Delta\mu_L$ and $\mu_R = \mu + \Delta\mu_R$ with $\Delta\mu_L, \Delta\mu_R \ll \mu$, the expressions for the current density can be further simplified. We can write the current density as

$$\mathcal{J} = \mathcal{J}_L + \mathcal{J}_R, \quad (4.16)$$

where \mathcal{J}_L and \mathcal{J}_R are contributions of the left and right reservoirs, respectively. These are given by,

$$\mathcal{J}_{L/R}(x, y; x', y') = \sum_{a,b=1}^2 \int_{-\infty}^{\mu+\Delta\mu_{L/R}} d\omega \operatorname{Im} \left[H_W[x, y, a; x', y', b] C_{L/R}[x, y, a; x', y', b](\omega) \right]. \quad (4.17)$$

If $\Delta\mu_{L/R}$ are small, then this equation could be expressed as,

$$\mathcal{J}_{L/R}[x, y; x', y'] = \mathcal{J}_{L/R}^{eq}[x, y; x', y'] + \bar{\mathcal{J}}_{L/R}[x, y; x', y'], \quad (4.18)$$

where $\mathcal{J}_{L/R}^{eq}$ and $\bar{\mathcal{J}}_{L/R}$ is the equilibrium and the excess part of $\mathcal{J}_{L/R}$, respectively. These are given by,

$$\mathcal{J}_{L/R}^{eq}[x, y; x', y'] = \sum_{a,b=1}^2 \int_{-\infty}^{\mu} d\omega \operatorname{Im} \left(H_W[x, y, a; x', y', b] C_{L/R}[x, y, a; x', y', b](\omega) \right), \quad (4.19)$$

$$\frac{\bar{\mathcal{J}}_{L/R}[x, y; x', y']}{\Delta\mu_{L/R}} = \sum_{a,b=1}^2 \operatorname{Im} \left[H_W[x, y, a; x', y', b] C_{L/R}[x, y, a; x', y', b](\mu) \right]. \quad (4.20)$$

Therefore, the net current density, $\mathcal{J} = \mathcal{J}_L + \mathcal{J}_R$, can also be split into the equilibrium part, $\mathcal{J}^{eq} = \mathcal{J}_L^{eq} + \mathcal{J}_R^{eq}$, and the excess part, $\bar{\mathcal{J}} = \bar{\mathcal{J}}_L + \bar{\mathcal{J}}_R$. Inside the normal metallic region, the equilibrium part of the current density on every bond would vanish. However, since the Chern insulator can support chiral persistent edge currents, \mathcal{J}^{eq} would not be zero on and close to the edges. Note however that if we sum this over all horizontal bonds across any transverse cross-section there will be no net current, as expected in equilibrium. On the other hand, the excess current, $\bar{\mathcal{J}}$, is a relatively small correction over \mathcal{J}^{eq} , and is the

transport current arising due to the chemical potential difference between the reservoirs. Only the total current is expected to respect the chirality of the Chern insulator, not the excess current. As the excess current is proportional to $\Delta\mu_{L/R}$, this implies that the current inside the insulator flips its sign, on changing $\Delta\mu_{L/R}$ to $-\Delta\mu_{L/R}$ and could flow opposite to the chirality of the insulator.

With similar arguments, the excess charge density, $\bar{\rho} = \rho - \rho^{eq}$, where ρ^{eq} is the charge density for $\Delta\mu_L = \Delta\mu_R = 0$, can be expressed in a form similar to \mathcal{J} . We get:

$$\bar{\rho}(x, y) = \sum_{a=1}^2 C_L[x, y, a; x, y, a](\mu)\Delta\mu_L + C_R[x, y, a; x, y, a](\mu)\Delta\mu_R. \quad (4.21)$$

For the SBHZ wire, the edge modes lie within the gap, we therefore always set μ to be within the gap of the insulator. In the next section, we present numerical results for the conductance $G(\mu)$ and the excess charge and current density profiles.

4.2 Numerical results

4.2.1 Conductance

In Fig. (4.4), we plot the conductance as a function of the Fermi level, μ for two system sizes. It is seen that when the Fermi level lies in the gap, the value of the conductance (in units of e^2/h) is quantized to the value 1. This conductance plateau is due to the edge modes present in the gap of the bulk spectrum. In Fig. (4.4b) and Fig. (4.4c) we show the variation of the strength of the plateau at Fermi level $\mu = 0$ with the strength of the coupling with the reservoirs, η_c and width of the insulator, N_y , respectively. From these plots, we see that the conductance strength grows to the quantized value and eventually becomes independent of η_c and N_y , when they are sufficiently large. The growth to the quantized value is oscillatory, with exact quantization being achieved at certain values of η_c and N_y . The inset of Fig. (4.4b) shows that the oscillation period scales as $N_y^{1/2}\eta_c$. The conductance

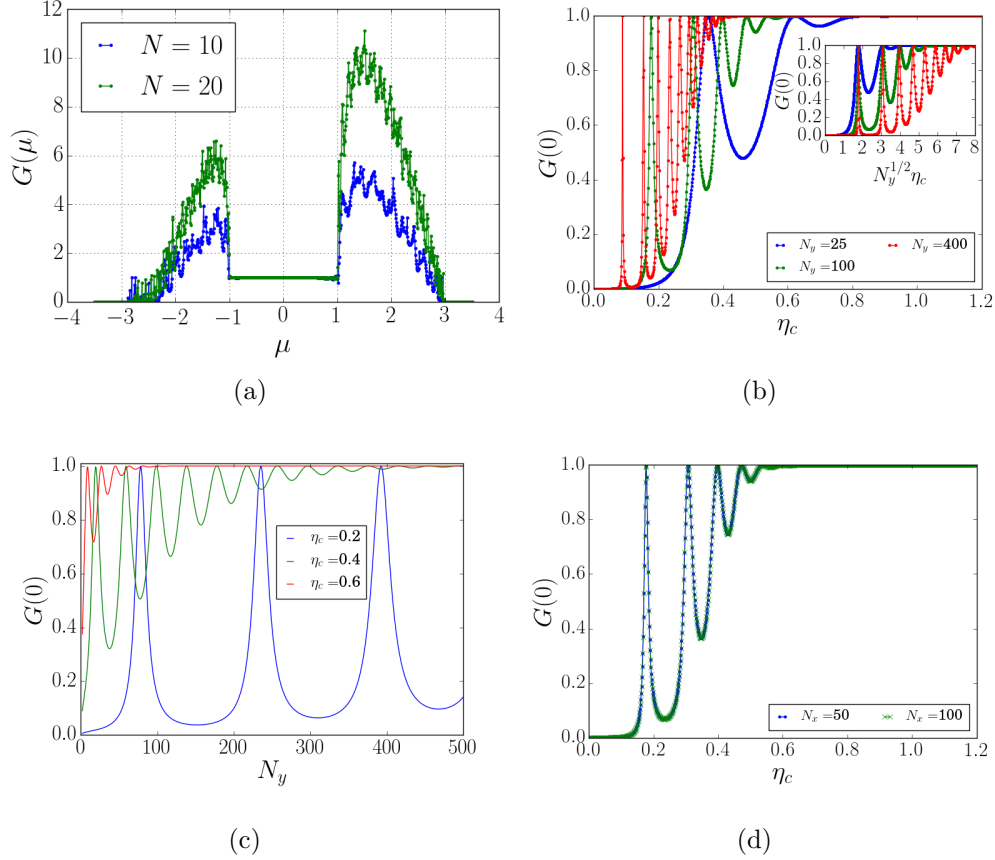


Figure 4.4: In (a) we show the variation of the conductance with the Fermi level, μ . (b) and (c) show the variation of the conductance at the Fermi level, $\mu = 0$, with η_c and N_y , respectively at $N_x = 100$. The inset in (b) shows that, on scaling η_c with $N_y^{1/2}$, the peaks in the oscillations coincide and therefore the period of the oscillations scales as $N_y^{1/2}\eta_c$. (d) shows the variation of the conductance at zero Fermi level with η_c at different N_x with $N_y = 100$. Parameter values; for (a) $N_x = N_y = N$, $\eta_b = 2$, $\mu_w = 1$, $\eta_c = 1.5$ and for (b), (c) and (d) $\eta_b = 2$ and $\mu_w = 1$.

does not depend on changing N_x at fixed N_y . This can be seen from Fig. (4.4d) which shows the variation of the conductance at zero Fermi level with respect to η_c at different values of N_x .

4.2.2 Charge and Current density

We first look at the excess charge and current density inside the Chern insulator, with the Fermi level set at $\mu = 0$. From Fig (4.5), we see that the current flows along the edges of the insulator, and the charge density is also localized along the edges, as expected. The excess charge and current density are sensitive to the choice of $\Delta\mu_L$ and $\Delta\mu_R$. This can be seen by comparing Fig (4.5a) and Fig (4.5b) for the choice $\Delta\mu_R = 0$, with Fig (4.5c) and Fig (4.5d), where we set $\Delta\mu_L = 0$. For these choices, the current flow is according to the chirality of the insulator. However, on changing the signs of $\Delta\mu_{L,R}$, we note that currents everywhere are reversed, which means that the excess currents inside the insulator are of chirality opposite to that of the isolated insulator.

Next, in Fig 4.6, we show the excess current density inside the normal metallic regions. Remarkably, the excess current density is sharply localized even in the normal metallic regions. We see that the current primarily flows along the lines at 45 degrees to the horizontal direction and gets multiply reflected until it reaches the top corner of the SBHZ wire. At this corner, it gets injected into the insulator inside which it flows along the edges and then leaves at the diagonally opposite corner where it enters the normal metallic region on the other end. These features smoothly fade away as we tune the Fermi level of the reservoirs. Thus, we see in Fig. (4.6b) that at $\mu = 0.2$, the localization of the current disappears deep in the metallic region. The fact that the observed localization is sharp at $\mu = 0$ seems to suggest that it is very special to the scattering state formed by the isolated edge modes of the insulator and the reservoir modes present at zero energy. At zero energy, the Fermi surface in the bulk of the reservoirs is a square in momentum space. The localization could arise from a particular superposition of the modes on this surface. As an example, consider the setup in Fig. 4.7 where a current is injected into a semi-infinite metallic strip of width

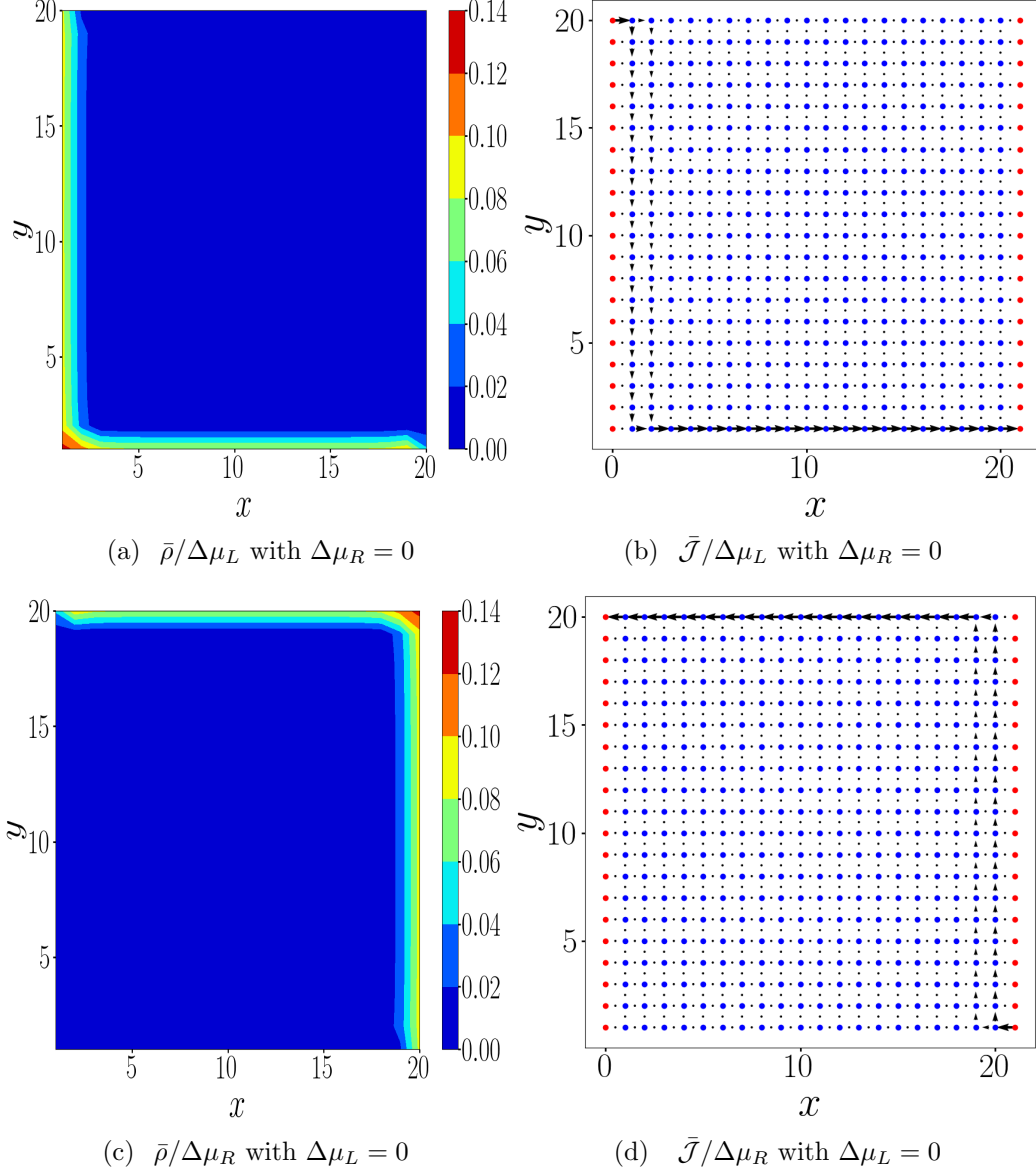
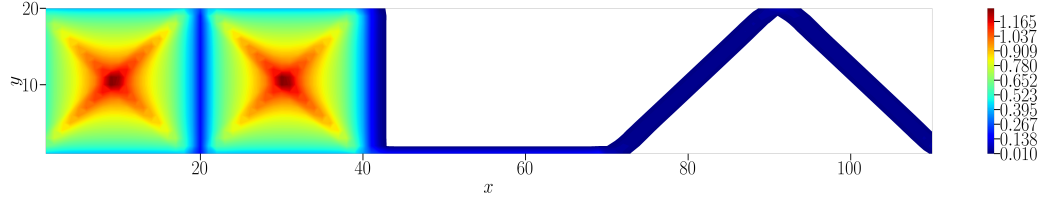
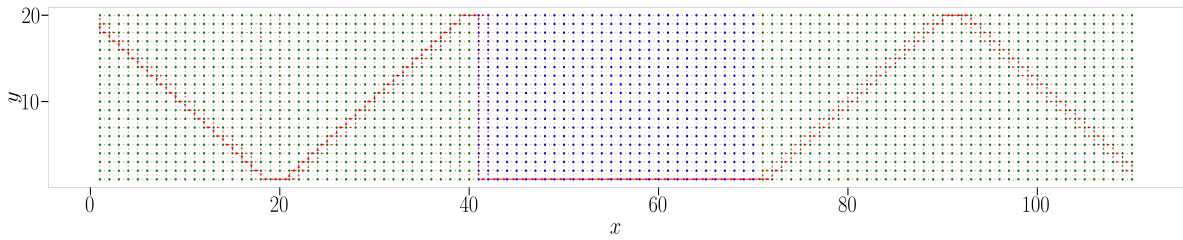


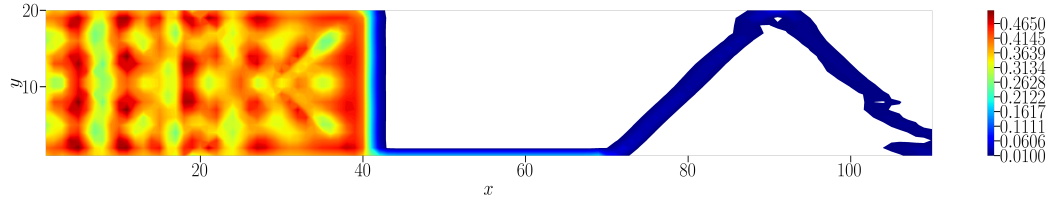
Figure 4.5: Excess charge density and current density inside the Chern insulator at the Fermi level, $\mu = 0$. Deep in the insulator (marked blue) the density has a value less than 10^{-8} . In (b) and (d), the size of the arrows indicate the current strength. Parameter values: $N_x = N_y = 20$ and $\eta_b = 1, \eta_c = 1, \mu_w = 1$.



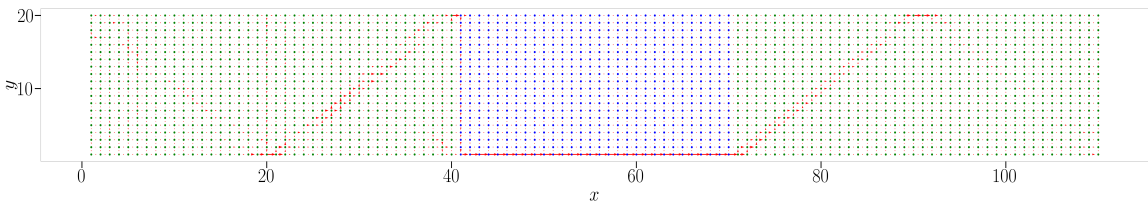
(a) $\bar{\rho}/\Delta\mu_L$ with $\mu = 0$



(b) $\bar{J}/\Delta\mu_L$ with $\mu = 0$



(c) $\bar{\rho}/\Delta\mu_L$ with $\mu = 0.2$



(d) $\bar{J}/\Delta\mu_L$ with $\mu = 0.2$

Figure 4.6: Excess charge and current densities in the reservoirs and the SBHZ wire. Deep inside the insulator (white region), the density has a value less than 10^{-8} . The current in the reservoirs is localized along the lines at 45 degrees to the horizontal directions. Parameter Values–Size of the SBHZ wire (blue region)= 30×20 , $\Delta\mu_R = 0, \eta_b = \eta_c = 1$ and $\mu_w = 1$.

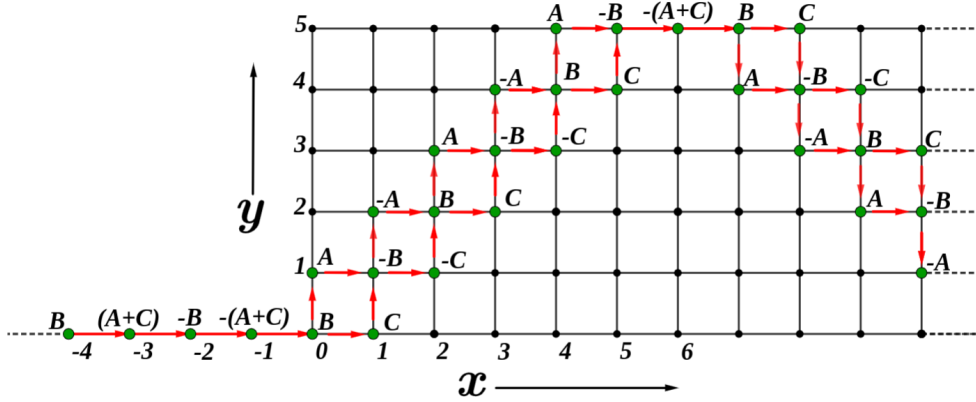
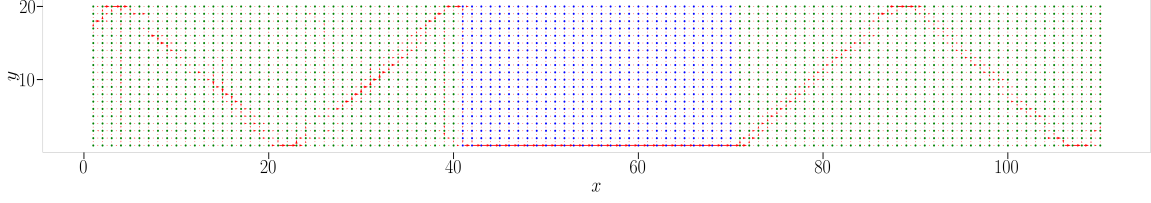


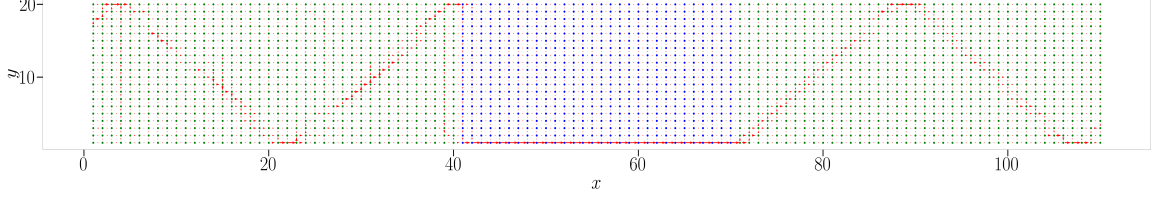
Figure 4.7: A scattering state at zero energy in a 2D metallic strip with injection at the left bottom corner. The wavefunction is non-zero only on the green-marked sites, with the amplitudes indicated by A, B, C and their combinations. The red arrows indicate the currents. If the hopping from the 1D reservoir to the 2D metallic strip is set η_c , then a similar solution for the wavefunction could be constructed by making the replacement $(A + C) \rightarrow (A + C)/\eta_c$ inside the 1D reservoir and $B \rightarrow B/\eta_c$ inside the metallic strip.

W at the left-bottom corner through a point contact with a 1D reservoir. The motivation for considering such a setup comes purely from the numerical observation (in Fig. (4.6)) that the current is injected at the corner into the metallic region. For simplicity, let the Hamiltonian of the 1D reservoir and the metallic strip be the nearest neighbor tight-binding Hamiltonian, with all the hopping parameters, including the hopping for the point contact at the corner, set to 1. Therefore, at any lattice site (x, y) on this setup, the equation for the wave function at zero energy would be that the wave function components at lattice points, that are nearest neighbor to (x, y) , should sum to zero. In Fig 4.7, an ansatz is presented for one such scattering state at zero energy — this displays a similar current localization as we see in our original model. The wave function is non-zero only at the green sites, where $A, B,$ and C are arbitrary complex numbers, and is zero otherwise. As $W \rightarrow \infty$, the ansatz can be written as a simple superposition of states on the square Fermi surface. The existence of such states seems to suggest that the observed localization may be a consequence of the current injection at the corners, which in turn is related to the edge physics of the Chern insulator.

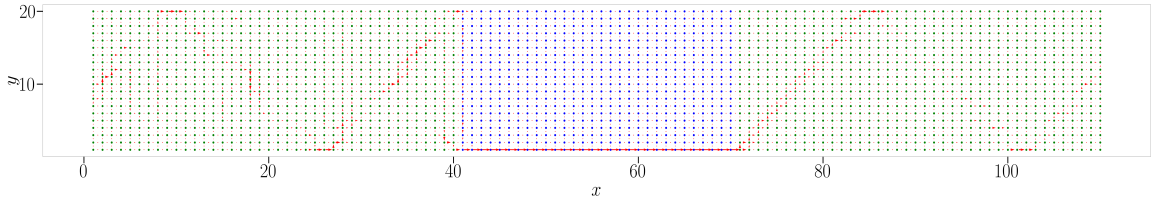
If the Fermi surface is slightly deformed, we expect these features to be retained up to slight perturbations. To check this, we introduce anisotropy in the reservoirs by choosing the



(a) $\bar{\mathcal{J}}/\Delta\mu_L$ with with $\eta_{by} = 1.1$



(b) $\bar{\mathcal{J}}/\Delta\mu_L$ with with $\eta_{by} = 1.2$



(c) $\bar{\mathcal{J}}/\Delta\mu_L$ with with $\eta_{by} = 1.3$

Figure 4.8: Excess current density in the anisotropic reservoirs and the SBHZ wire. The anisotropy is introduced by choosing different hopping, denoted by η_{bx} and η_{by} , in the x and y directions respectively. The current in the reservoirs is localized along the lines at 45 degrees to the horizontal directions. Parameter Values–Size of the SBHZ wire (blue region)= 30×20 , $\Delta\mu_R = 0$, $\eta_{bx} = \eta_c = 1$, $\mu = 0$ and $\mu_w = 1$.

hopping in the x and y directions to be η_{bx} and η_{by} respectively. The results are shown in Fig. (4.8), where we plot the current densities for $\eta_{by} = 1.1$, $\eta_{by} = 1.2$ and $\eta_{by} = 1.3$ with $\eta_{bx} = 1$. We see that the localization feature is indeed retained for small perturbations but slowly gets washed away for increased anisotropy. Interestingly, on changing η_{by} , the angle of the lines with the x -axis also gets changed from 45 degrees.

4.3 Conclusion

In conclusion, we looked at electronic transport properties due to the edge modes of a Chern insulator in the open system geometry and using a microscopic approach based on the NEGF formalism. For arbitrary choices of the coupling between the insulator and leads, we find that, in the topologically non-trivial regime, the conductance is quantized and the transport current and charge densities are localized along the edges of the insulator. This is as is expected from a phenomenological Landauer-Buttiker argument with perfect point contacts. We find several interesting results on finite size effects and properties of the current density inside the reservoirs. We discuss our findings below:

- We have provided numerical evidence, in a specific model, that the two terminal longitudinal conductance of a Chern insulator in an open geometry, namely coupled with metallic leads is quantized. An analytic proof of this for a large class of models is desirable and remains an open problem. The conductance, at Fermi level $\mu = 0$, increases non-monotonically with the coupling of the insulator and the reservoirs. The growth to the quantized value shows oscillations with a period that scales as $N_y^{1/2} \eta_c$.
- Our most interesting finding is that, at zero Fermi level, despite the fact that the CI and the leads are coupled throughout the edge, the current injection into the CI and ejection from the CI occurs only at the corners. Furthermore, the current density in the leads is sharply localized in the metallic leads, at the scale of a few lattice spacing. These features remain roughly true for small perturbations of the geometry of the Fermi surface of the leads.
- The quantized conductance is a topological property. For an open system, it is physically reasonable to define a topological property as one that is independent of the details of the properties of the leads and the coupling of the leads to the INT. On the other hand the patterns of current densities and charge densities, namely the geometry of these observables are dependent on the model. We present numerical evidence that, the geometry of these observables are largely determined by the shape, namely

geometry, of the Fermi surface of the leads. We illustrated this by looking at current densities as the Fermi level is tuned away from zero, and by introducing anisotropy inside the metallic leads.

Chapter 5

Classical harmonic wires in presence of a magnetic field

Heat transport in harmonic wires has been extensively studied. Ordered harmonic wires lead to ballistic transport where the heat current saturates in the thermodynamic limit, on the other hand for disordered harmonic wires the current goes down with system size due to Anderson localization. Typically, due to Anderson localization all the energy modes get localized with a energy dependent localization length and the heat current scales exponentially with system size. However, for special cases of disordered parameter, for example mass disordered harmonic chains, the localization length diverges as the energy of the mode approaches zero. Therefore, low energy modes still contribute to the heat transport and due to this the current scales as a power law with system size. This power law is dependent on the behaviour of the transmission and the localization length at low frequencies. The behaviour of the transmission is dependent on whether the ends of the harmonic chain are free or fixed. Due to this the current power laws also depend on the boundary conditions. For mass disordered harmonic wires, these power laws were found to be $1/N^{1/2}$ and $1/N^{3/2}$ for free and fixed boundary conditions respectively.

Harmonic wires in presence of magnetic fields were recently studied and several interesting results on the behaviour of heat transport were obtained [48, 49, 50]. Particularly, Ref. [48]

studied harmonic wires with magnetic field and stochastic momentum exchange(modelling non-linearities) and showed that the current exponent is completely changed in presence of a magnetic field. This was attributed to the fact that the magnetic field changes the spectrum of the system and the lower band shows a dispersion, $\omega(q) \sim q^2$. In this chapter, we investigate the question of heat transport properties in absence of the stochastic noise but with ordered and disordered magnetic fields.

In Sec. 5.1, we introduce the model and derive the heat current for any spatial configuration of the magnetic field using the NEGF formalism. We discuss briefly the similarity with the 1-D Kitaev chain. We also express the Green's function as product of matrices which is useful to make analytical progress. In Sec. 5.2, we consider the ordered case and derive the expression for the heat current in the thermodynamic limit for two different boundary conditions. From these expressions, we discuss the low frequency behaviour of the heat transmission, and we find that the presence of the magnetic field strongly modifies this behaviour. In Sec. 5.3, we look at the disordered magnetic field case and derive the behaviour of the Lyapunov exponent (inverse of localization length) at low frequencies. Using the results for the transmission and the Lyapunov exponent at low frequencies, we obtain the power laws for the for the current by using heuristic arguments. We also obtain the power laws numerically. On comparison with the theory, we find that for the case where expectation value of the magnetic field is non-zero we see a good agreement. However, for the expectation of the magnetic field to be zero, we don't find a good agreement between the theory and the numerics. We provide an explanation of this disagreement.

5.1 The model and derivation of heat current using NEGF

5.1.1 The model

We consider a chain of N harmonic oscillators each having two transverse degree's of freedom so that every oscillator is free to move in a plane perpendicular to the length of the chain. We choose the plane of motion to be the $x-y$ plane and denote the positions and momenta of the n^{th} oscillator by (x_n, y_n) and (p_n^x, p_n^y) respectively, with $n = 1, 2, \dots, N$. The oscillators are assumed to have masses, m , and each carry a positive charge e . We consider a site-dependent magnetic field $\vec{B}_n = B_n \vec{e}_z$, perpendicular to the plane of motion, which can be obtained from a vector potential $\vec{A}_n = (-B_n y_n, B_n x_n, 0)$ at each lattice site. The Hamiltonian of the chain is given by:

$$H = \sum_{n=1}^N \frac{(p_n^x + eB_n y_n)^2 + (p_n^y - eB_n x_n)^2}{2m} + k \sum_{n=0}^N \frac{(x_{n+1} - x_n)^2 + (y_{n+1} - y_n)^2}{2}$$

where k denotes the inter particle spring constant. We will consider the two different boundary conditions: (i) fixed boundaries with $x_0 = x_{N+1} = 0$ and (ii) free boundaries with $x_0 = x_1$, $x_N = x_{N+1}$. In order to study heat current through this system, we consider the 1st and the N^{th} oscillators to be connected to heat reservoirs at temperatures T_L and T_R respectively. The heat reservoirs are modelled using dissipative and noise terms leading to the following Langevin equations of motion:

$$m\ddot{x}_n = k(x_{n+1} + x_{n-1} - c_n x_n) + eB_n \dot{y}_n + \eta_L^x(t) \delta_{n,1} + \eta_R^x(t) \delta_{n,N} - (\gamma \delta_{n,1} + \gamma \delta_{n,N}) \dot{x}_n, \quad (5.1)$$

$$m\ddot{y}_n = k(y_{n+1} + y_{n-1} - c_n y_n) - eB_n \dot{x}_n + \eta_L^y(t) \delta_{n,1} + \eta_R^y(t) \delta_{n,N} - (\gamma \delta_{n,1} + \gamma \delta_{n,N}) \dot{y}_n. \quad (5.2)$$

for $n = 1, 2, \dots, N$. Here $\eta_L(t) := (\eta_L^x(t), \eta_L^y(t))$ and $\eta_R(t) := (\eta_R^x(t), \eta_R^y(t))$ are Gaussian white noise terms acting on the 1st and N^{th} oscillators respectively. These follow the regular white noise correlations, $\langle \eta_{L/R}(t) \eta_{L/R}(t') \rangle = 2\gamma T_{L/R} \delta(t - t')$ (Boltzmann's constant is fixed

to one to simplify), where γ is the dissipation strength at the reservoirs. The coefficients c_n fix the boundary conditions of the problem. For fixed boundaries $c_n = 2$ for all n , while for free boundary conditions $c_n = 2 - \delta_{n,1} - \delta_{n,N}$.

5.1.2 Heat current using NEGF

For heat current in the setup considered here, we need to obtain the steady state solution of the equations of motion given by Eq. (5.1)-(5.2). Denoting by $\tilde{u}(\omega) = \frac{1}{2\pi} \int_{-\infty}^{\infty} e^{-i\omega t} u(t) dt$ the Fourier transform of any function $u(t)$, we rewrite the Langevin equations in Fourier space as

$$\begin{aligned} (-m\omega^2 + c_n k + i\gamma\omega\delta_{n,1} + i\gamma\omega\delta_{n,N})\tilde{x}_n(\omega) - i\omega e B_n \tilde{y}_n(\omega) \\ - k\tilde{x}_{n+1}(\omega) - k\tilde{x}_{n-1}(\omega) = \tilde{\eta}_L^x(\omega)\delta_{n,1} + \eta_R^x(\omega)\delta_{n,N}, \end{aligned} \quad (5.3)$$

$$\begin{aligned} (-m\omega^2 + c_n k + i\gamma\omega\delta_{n,1} + i\gamma\omega\delta_{n,N})\tilde{y}_n(\omega) + i\omega e B_n \tilde{x}_n(\omega) \\ - k\tilde{y}_{n+1}(\omega) - k\tilde{y}_{n-1}(\omega) = \tilde{\eta}_L^y(\omega)\delta_{n,1} + \eta_R^y(\omega)\delta_{n,N}. \end{aligned} \quad (5.4)$$

The noise correlations in Fourier space now satisfy $\langle \eta_{L/R}(\omega)\eta_{L/R}(\omega') \rangle = (\gamma T_{L/R}/\pi)\delta(\omega + \omega')$.

Let us define the column vectors

$$\tilde{X}(\omega) = \begin{pmatrix} \tilde{x}_1(\omega) \\ \tilde{x}_2(\omega) \\ \vdots \\ \tilde{x}_{N-1}(\omega) \\ \tilde{x}_N(\omega) \end{pmatrix}, \quad \tilde{Y}(\omega) = \begin{pmatrix} \tilde{y}_1(\omega) \\ \tilde{y}_2(\omega) \\ \vdots \\ \tilde{y}_{N-1}(\omega) \\ \tilde{y}_N(\omega) \end{pmatrix}, \quad \tilde{\eta}^{x/y}(\omega) = \begin{pmatrix} \tilde{\eta}_L^{x/y}(\omega) \\ 0 \\ \vdots \\ 0 \\ \tilde{\eta}_R^{x/y}(\omega) \end{pmatrix}$$

to write Eq. (5.3) and Eq. (5.4) jointly in the block-matrix form

$$\tilde{\mathcal{G}}^{-1}(\omega) \begin{pmatrix} \tilde{X}(\omega) \\ \tilde{Y}(\omega) \end{pmatrix} = \begin{pmatrix} \tilde{\eta}^x(\omega) \\ \tilde{\eta}^y(\omega) \end{pmatrix} \quad \text{with} \quad \tilde{\mathcal{G}}^{-1}(\omega) = \begin{pmatrix} \Pi(\omega) & K(\omega) \\ -K(\omega) & \Pi(\omega) \end{pmatrix}, \quad (5.5)$$

where $\Pi(\omega)$ and $K(\omega)$ are square matrices with matrix elements given by

$$[\Pi(\omega)]_{n,\ell} = (-m\omega^2 + c_n k)\delta_{n,\ell} - k(\delta_{n,\ell+1} + \delta_{n,\ell-1}) + i\gamma\omega\delta_{n,1}\delta_{\ell,1} + i\gamma\omega\delta_{n,N}\delta_{\ell,N} ,$$

$$[K(\omega)]_{n,\ell} = -ieB_n\omega\delta_{n,\ell}.$$

From Eq. (5.5), we can write the steady state solution directly by inverting the matrix $\tilde{\mathcal{G}}^{-1}(\omega)$. Therefore we have

$$\tilde{x}_n(\omega) = \sum_{\ell} [G_1^+(\omega)]_{n,\ell} \tilde{\eta}_{\ell}^x(\omega) + \sum_{\ell} [G_2^+(\omega)]_{n,\ell} \tilde{\eta}_{\ell}^y(\omega), \quad (5.6)$$

$$\tilde{y}_n(\omega) = -\sum_{\ell} [G_2^+(\omega)]_{n,\ell} \tilde{\eta}_{\ell}^x(\omega) + \sum_{\ell} [G_1^+(\omega)]_{n,\ell} \tilde{\eta}_{\ell}^y(\omega), \quad (5.7)$$

where

$$G_1^+ = [\Pi + K\Pi^{-1}K]^{-1} \quad \text{and} \quad G_2^+ = -G_1^+K\Pi^{-1}. \quad (5.8)$$

These two last matrices form the 2×2 block structure of the matrix $\tilde{\mathcal{G}}(\omega)$ as

$$\tilde{\mathcal{G}}(\omega) = \begin{pmatrix} G_1^+(\omega) & G_2^+(\omega) \\ -G_2^+(\omega) & G_1^+(\omega) \end{pmatrix}.$$

Defining the square matrices $G_{1/2}^- = [G_{1/2}^+]^\dagger$ and $\Gamma_{n,\ell}(\omega) = [\Pi^\dagger(\omega) - \Pi(\omega)]_{n,\ell} = -2i\omega(\gamma\delta_{n,1}\delta_{\ell,1} + \gamma\delta_{n,N}\delta_{\ell,N})$, one gets from Eq. (5.8) that $[G_1^-]^{-1} - [G_1^+]^{-1} = \Pi^\dagger - \Pi + K\Pi^{\dagger-1}K - K\Pi^{-1}K$. Multiplying this on the left by G_1^+ and on the right by G_1^- we get, after some manipulations, the following relation:

$$G_1^+(\omega) - G_1^-(\omega) = G_1^+\Gamma G_1^- + G_2^+\Gamma G_2^-. \quad (5.9)$$

This will be useful later on to put the heat current in the Landauer or NEGF form.

Having obtained the steady state solution, we now proceed to calculate the average heat current J_N in the steady state. We can compute the current at any point on the chain since the steady state value will be the same everywhere. Let us consider the current from the left reservoir into the system. This is given by taking the steady state average $\langle \cdot \rangle_{\text{ss}}$ of the dot

product of the velocity of the first particle with the force on it from the left reservoir, thus

$$J_N = -\gamma \langle \dot{x}_1^2 + \dot{y}_1^2 \rangle_{\text{ss}} + \langle \eta_L^x(t) \dot{x}_1 \rangle_{\text{ss}} + \langle \eta_L^y(t) \dot{y}_1 \rangle_{\text{ss}}.$$

The first term on simplification gives

$$\begin{aligned} -\gamma \langle \dot{x}_1^2 + \dot{y}_1^2 \rangle_{\text{ss}} = & - \int_{-\infty}^{\infty} \frac{d\omega}{\pi} \left\{ 2\gamma^2 T_L \omega^2 \left(|[G_1^+(\omega)]_{1,1}|^2 + |[G_2^+(\omega)]_{1,1}|^2 \right) \right. \\ & \left. + 2\gamma^2 T_R \omega^2 \left(|[G_1^+(\omega)]_{1,N}|^2 + |[G_2^+(\omega)]_{1,N}|^2 \right) \right\}, \end{aligned} \quad (5.10)$$

and the sum of the other two terms is given by

$$\begin{aligned} \langle \eta_L^x(t) \dot{x}_1 \rangle_{\text{ss}} + \langle \eta_L^y(t) \dot{y}_1 \rangle_{\text{ss}} = & \int_{-\infty}^{\infty} \frac{d\omega}{\pi} \left\{ i\omega [G_1^+(\omega)]_{1,1} \gamma T_L + i\omega [G_1^+(\omega)]_{1,1} \gamma T_L \right\} \quad (5.11) \\ = & 2T_L \int_{-\infty}^{\infty} \frac{d\omega}{\pi} \omega^2 \left\{ \left(|[G_1^+(\omega)]_{1,1}|^2 + |[G_2^+(\omega)]_{1,1}|^2 \right) \gamma^2 + \left(|[G_1^+(\omega)]_{1,N}|^2 + |[G_2^+(\omega)]_{1,N}|^2 \right) \gamma^2 \right\}, \end{aligned} \quad (5.12)$$

where in the last step we used Eq. (5.9). Adding Eq. (5.10) and Eq. (5.12) we finally get

$$J_N = (T_L - T_R) \int_{-\infty}^{\infty} d\omega \mathcal{T}_N(\omega) \quad (5.13)$$

where \mathcal{T}_N is the net transmission amplitude across the harmonic chain defined by

$$\mathcal{T}_N(\omega) = \frac{2\gamma^2}{\pi} \omega^2 \left[|[G_1^+(\omega)]_{1,N}|^2 + |[G_2^+(\omega)]_{1,N}|^2 \right]. \quad (5.14)$$

Note that in the absence of the magnetic field, $B_n = 0$, the Green's function, G_2^+ , vanishes and we recover the current due to two uncoupled oscillator chains [68]. The magnetic field couples the two transverse modes. In fact, we see from Eq. (5.6) that $G_2^+(\omega)$ connects the x -displacements with the y -displacements, and hence, it can be interpreted as the scattering matrix for a x -polarized incident plane wave to be scattered into a y -polarized wave. The term involving $G_1^+(\omega)$ is the normal transmission amplitude which is attributed to scattering of the incoming plane wave without change of polarization. The combination of the two terms leads to the rotation of the polarization of the incoming plane wave.

It is interesting to note that the mathematical structure of the Green's functions obtained here is of the same form as that found for electron transport in superconducting wires discussed in chapter 2. Analogous to the scattering between transverse modes that we see here, in superconducting wires, the superconducting order causes scattering between particle and hole electronic states.

5.1.3 Green's function as product of matrices

We now rewrite the components of the two Green's functions, $[G_1^+(\omega)]_{1,N}$ and $[G_2^+(\omega)]_{1,N}$ defined by Eq. (5.8), as a product of matrices using a transfer matrix approach. This will give us explicit expressions for the two components enabling us to obtain analytic closed-form results in special cases. We start by rewriting the equations of motion in a way such that the $2N \times 2N$ matrix $\tilde{\mathcal{G}}^{-1}(\omega)$ appearing in Eq. (5.5) gets restructured into a 2×2 -block tri-diagonal matrix, $\mathcal{G}(\omega)$. To that end, we define for each $k = 1, \dots, N$ the column vectors

$$\tilde{R}_n(\omega) = \begin{pmatrix} \tilde{x}_n(\omega) \\ \tilde{y}_n(\omega) \end{pmatrix}, \quad \tilde{\eta}_n(\omega) = \begin{pmatrix} \tilde{\eta}_n^x(\omega) \\ \tilde{\eta}_n^y(\omega) \end{pmatrix},$$

and notice that the Eq. (5.3) and Eq. (5.4) can then be written as

$$\sum_{\ell=1}^N [\mathcal{G}^{-1}(\omega)]_{n,\ell} \tilde{R}_\ell(\omega) = \tilde{\eta}_n(\omega), \quad (5.15)$$

where $[\mathcal{G}^{-1}(\omega)]_{k,\ell}$ are 2×2 matrices defined via $\mathcal{G}^{-1}(\omega)$ given by

$$\mathcal{G}^{-1}(\omega) = \begin{pmatrix} A_1(\omega) + i\gamma\omega I_2 & -kI_2 & 0 & 0 & \dots & 0 & 0 \\ -kI_2 & A_2(\omega) & -kI_2 & 0 & \dots & 0 & 0 \\ 0 & -kI_2 & A_3(\omega) & -kI_2 & \dots & 0 & 0 \\ \vdots & \vdots & \vdots & \ddots & & \vdots & \vdots \\ \vdots & \vdots & \vdots & & \ddots & \vdots & \vdots \\ \vdots & \vdots & \vdots & \dots & -kI_2 & A_{N-1}(\omega) & -kI_2 \\ 0 & 0 & 0 & \dots & \dots & -kI_2 & A_N(\omega) + i\gamma\omega I_2 \end{pmatrix}.$$

Here I_n refers to a $n \times n$ identity matrix, while $A_\ell(\omega)$ is the 2×2 matrix defined by

$$A_\ell := A_\ell(\omega) = \begin{pmatrix} -m\omega^2 + c_\ell k & -i\omega e B_\ell \\ i\omega e B_\ell & -m\omega^2 + c_\ell k \end{pmatrix}, \quad \ell = 1, \dots, N.$$

Notice that Eq. (5.15) gives $\tilde{R}_\ell(\omega) = \sum_k [\mathcal{G}(\omega)]_{\ell,k} \tilde{\eta}_k(\omega)$, so on comparison with the solution in Eq. (5.6) and Eq. (5.7) we can write the components of the 2×2 matrix $[\mathcal{G}(\omega)]_{k,\ell}$ to be

$$[\mathcal{G}(\omega)]_{n,\ell} = \begin{pmatrix} [G_1^+(\omega)]_{n,\ell} & [G_2^+(\omega)]_{n,\ell} \\ -[G_2^+(\omega)]_{n,\ell} & [G_1^+(\omega)]_{n,\ell} \end{pmatrix}. \quad (5.16)$$

Thus we now require the 2×2 block $[\mathcal{G}(\omega)]_{1,N}$ to calculate the components $[G_1^+(\omega)]_{1,N}$ and $[G_2^+(\omega)]_{1,N}$. Since the matrix $\mathcal{G}^{-1}(\omega)$ is tri-diagonal, $[\mathcal{G}^+(\omega)]_{1,N}$ can be expressed as products of matrices using a transfer matrix approach. This may be achieved by writing down the first column of equations from the identity $\mathcal{G}(\omega)\mathcal{G}^{-1}(\omega) = I_{2N}$,

$$\mathcal{G}_{1,1}(A_1 + i\gamma\omega I_2) - k\mathcal{G}_{1,2} = I_2, \quad (5.17)$$

$$\mathcal{G}_{1,\ell-1} + \mathcal{G}_{1,\ell+1} - k^{-1}\mathcal{G}_{1,\ell}A_\ell = 0, \quad 1 < \ell < N, \quad (5.18)$$

$$\mathcal{G}_{1,N}(A_N + i\gamma\omega I_2) - k\mathcal{G}_{1,N-1} = 0. \quad (5.19)$$

We now write these equations in the form

$$\begin{pmatrix} I_2 & \mathcal{G}_{11} \end{pmatrix} = \begin{pmatrix} \mathcal{G}_{11} & \mathcal{G}_{12} \end{pmatrix} \begin{pmatrix} A_1 + i\gamma\omega I_2 & I_2 \\ -kI_2 & 0 \end{pmatrix}, \quad (5.20)$$

$$\begin{pmatrix} \mathcal{G}_{1,\ell-1} & \mathcal{G}_{\ell,\ell} \end{pmatrix} = \begin{pmatrix} \mathcal{G}_{1,\ell} & \mathcal{G}_{1,\ell+1} \end{pmatrix} \begin{pmatrix} k^{-1}A_\ell & I_2 \\ -I_2 & 0 \end{pmatrix}, \quad 1 < \ell < N \quad (5.21)$$

$$\begin{pmatrix} \mathcal{G}_{1,N-1} & \mathcal{G}_{1,N} \end{pmatrix} = \begin{pmatrix} \mathcal{G}_{1,N} & 0 \end{pmatrix} \begin{pmatrix} k^{-1}(A_N + i\gamma\omega I_2) & I_2 \\ 0 & 0 \end{pmatrix}. \quad (5.22)$$

We then use Eq. (5.21) in Eq. (5.20) repeatedly and finally use Eq. (5.22) to get,

$$\begin{pmatrix} I_2 & \mathcal{G}_{11} \end{pmatrix} = \begin{pmatrix} \mathcal{G}_{1N} & 0 \end{pmatrix} \Omega_L \Pi_N \Omega_R \quad (5.23)$$

with the the 4×4 matrices $\Omega_L, \Pi_N, \Omega_R$ defined by

$$\begin{aligned} \Omega_L &= \begin{pmatrix} I_2 & -i\frac{\gamma\omega}{k}I_2 \\ 0 & 0 \end{pmatrix}, \quad \Omega_R = \begin{pmatrix} kI_2 & 0 \\ i\gamma\omega I_2 & I_2 \end{pmatrix}, \\ \Pi_N &= \prod_{\ell=1}^N \Omega_\ell = \prod_{\ell=1}^N \begin{pmatrix} k^{-1}A_\ell & I_2 \\ -I_2 & 0 \end{pmatrix} = \prod_{\ell=1}^N \begin{pmatrix} a_\ell I_2 + b_\ell \sigma^y & I_2 \\ -I_2 & 0 \end{pmatrix} \end{aligned} \quad (5.24)$$

where $\sigma^y = \begin{pmatrix} 0 & -i \\ i & 0 \end{pmatrix}$ is the second Pauli's matrix and

$$a_\ell := a_\ell(\omega) = (-m\omega^2 + c_\ell k)/k, \quad b_\ell := b_\ell(\omega) = \omega e B_\ell / k. \quad (5.25)$$

Thus we have expressed the required components of the Green's function as a product of 4×4 matrices Ω_ℓ . This product can further be simplified by making a unitary transformation such that $\sigma^y = U^\dagger \sigma^z U$ with $\sigma^z = \begin{pmatrix} 1 & 0 \\ 0 & -1 \end{pmatrix}$ the third Pauli's matrix, in order to diagonalise

the matrix $a_\ell I_2 + b_\ell \sigma^y$. This makes the product to be

$$\Pi_N = \prod_{\ell=1}^N \begin{pmatrix} a_\ell I_2 + b_\ell \sigma^y & I_2 \\ -I_2 & 0 \end{pmatrix} = \begin{pmatrix} U^\dagger & 0 \\ 0 & U^\dagger \end{pmatrix} \prod_{\ell=1}^N \begin{pmatrix} a_\ell I_2 + b_\ell \sigma^z & I_2 \\ -I_2 & 0 \end{pmatrix} \begin{pmatrix} U & 0 \\ 0 & U \end{pmatrix}.$$

The product in this equation is now composed of 2×2 diagonal blocks and therefore we have that for any $1 \leq n \leq N$,

$$\prod_{\ell=1}^n \begin{pmatrix} a_\ell I_2 + b_\ell \sigma^z & I_2 \\ -I_2 & 0 \end{pmatrix} = \begin{pmatrix} f_n^+ & 0 & g_n^+ & 0 \\ 0 & f_n^- & 0 & g_n^- \\ -f_{n-1}^+ & 0 & -g_{n-1}^+ & 0 \\ 0 & -f_{n-1}^- & 0 & -g_{n-1}^- \end{pmatrix}$$

where the numbers f_n^\pm, g_n^\pm , defined for $n = 0, 1, \dots, N$, follow the same second order recursive equation but with different initial conditions. More exactly we have that for

$$\begin{aligned} f_{n+1}^\pm &= (a_{n+1} \pm b_{n+1})f_n^\pm - f_{n-1}^\pm, & f_0^\pm &= 1, & f_1^\pm &= a_1 \pm b_1, \\ g_{n+1}^\pm &= (a_{n+1} \pm b_{n+1})g_n^\pm - g_{n-1}^\pm, & g_0^\pm &= 0, & g_1^\pm &= 1. \end{aligned} \tag{5.26}$$

Therefore, the 4×4 matrices in the product are effectively reduced to 2×2 matrices. The expressions for f_n^\pm, g_n^\pm could be exactly found for the two boundary conditions. We do this in the next section, for now we conclude this section by expressing required components of the Green's function using the variables f_n^\pm, g_n^\pm . We use $U = \frac{1}{\sqrt{2}} \begin{pmatrix} i & 1 \\ -i & 1 \end{pmatrix}$ to rewrite Π_N as,

$$\Pi_N = \frac{1}{2i} \begin{pmatrix} i(f_N^+ + f_N^-) & (f_N^+ - f_N^-) & i(g_N^+ + g_N^-) & (g_N^+ - g_N^-) \\ -(f_N^+ - f_N^-) & i(f_N^+ + f_N^-) & -(g_N^+ - g_N^-) & i(g_N^+ + g_N^-) \\ -i(f_{N-1}^+ + f_{N-1}^-) & -(f_{N-1}^+ - f_{N-1}^-) & -i(g_{N-1}^+ + g_{N-1}^-) & -(g_{N-1}^+ - g_{N-1}^-) \\ (f_{N-1}^+ - f_{N-1}^-) & -i(f_{N-1}^+ + f_{N-1}^-) & (g_{N-1}^+ - g_{N-1}^-) & -i(g_{N-1}^+ + g_{N-1}^-) \end{pmatrix}. \tag{5.27}$$

We define the matrices P_N and Q_N as follows,

$$P_N = \frac{1}{2i} \begin{pmatrix} i(f_N^+ + f_N^-) & f_N^+ - f_N^- \\ -(f_N^+ - f_N^-) & i(f_N^+ + f_N^-) \end{pmatrix} \quad Q_N = \frac{1}{2i} \begin{pmatrix} i(g_N^+ + g_N^-) & g_N^+ - g_N^- \\ -(g_N^+ - g_N^-) & i(g_N^+ + g_N^-) \end{pmatrix}. \quad (5.28)$$

Then

$$\Pi_N = \begin{pmatrix} P_N & Q_N \\ -P_{N-1} & -Q_{N-1} \end{pmatrix}. \quad (5.29)$$

Substituting Π_N from Eq. (5.27) in Eq. (5.23), we can show that

$$I_2 = \mathcal{G}_{1,N} \left(kP_N + i\gamma\omega(Q_N + P_{N-1}) - \frac{\gamma^2\omega^2}{k}Q_{N-1} \right) = \mathcal{G}_{1,N} \begin{pmatrix} \frac{1}{2}(F_N^+ + F_N^-) & \frac{1}{2i}(F_N^+ - F_N^-) \\ -\frac{1}{2i}(F_N^+ - F_N^-) & \frac{1}{2}(F_N^+ + F_N^-) \end{pmatrix} \quad (5.30)$$

$$\mathcal{G}_{11} = \mathcal{G}_{1,N} \left(Q_N + i\frac{\gamma\omega}{k}Q_{N-1} \right) \quad (5.31)$$

where

$$F_N^\pm := F_N^\pm(\omega) = k \left(f_N^\pm + i\frac{\gamma}{k}\omega(g_N^\pm + f_{N-1}^\pm) - \frac{\gamma^2}{k^2}\omega^2 g_{N-1}^\pm \right). \quad (5.32)$$

Using Eq. (5.16) and inverting Eq. (5.30) gives us the required components of the Green's functions:

$$[G_1^+]_{1,N} = \frac{1}{2} \left(\frac{1}{F_N^+} + \frac{1}{F_N^-} \right) \quad \text{and} \quad [G_2^+]_{1,N} = -\frac{1}{2i} \left(\frac{1}{F_N^+} - \frac{1}{F_N^-} \right).$$

These then give, using Eqs. (5.13)-(5.14), the heat current to be

$$J_N = (T_L - T_R) \frac{\gamma^2}{\pi} \int_{-\infty}^{\infty} d\omega \omega^2 \left[\frac{1}{|F_N^+(\omega)|^2} + \frac{1}{|F_N^-(\omega)|^2} \right]. \quad (5.33)$$

Thus we have now obtained a new expression for the net transmission amplitude $\mathcal{T}_N(\omega)$. In the next section we use this form and, for the case of a uniform magnetic field, derive analytical expressions for the current in the thermodynamic limit. Before that, we take a quick digression to discuss the temperature profile.

Temperature Profile

We can also obtain the temperature profile of the chain, which is defined as $T_\ell = m \langle \dot{x}_\ell^2(t) + \dot{y}_\ell^2(t) \rangle$. Using the steady state expression for $x_\ell(t)$ and $y_\ell(t)$, we can show that this is given by,

$$T_\ell = T_L \Lambda_\ell + T_R (1 - \Lambda_\ell); \quad \Lambda_\ell = \int_{-\infty}^{\infty} \frac{d\omega}{\pi} m \gamma \omega^2 [|G_1^+(\omega)|_{1\ell}^2 + |G_2^+(\omega)|_{1\ell}^2] \quad (5.34)$$

Using Eq. (5.20), Eq. (5.21) and Eq. (5.22), we could obtain the matrix block $\mathcal{G}_{1\ell}$, containing the required components for the temperature profile, to be,

$$\begin{pmatrix} I_2 & \mathcal{G}_{11} \end{pmatrix} = \begin{pmatrix} \mathcal{G}_{1\ell} & \mathcal{G}_{1,\ell+1} \end{pmatrix} \Pi_\ell \Omega_R = \begin{pmatrix} \mathcal{G}_{1\ell} & \mathcal{G}_{1,\ell+1} \end{pmatrix} \begin{pmatrix} kP_\ell + i\gamma\omega Q_\ell & Q_\ell \\ -kP_{\ell-1} - i\gamma\omega Q_{\ell+1} & -Q_{\ell-1} \end{pmatrix} \quad (5.35)$$

where Π_ℓ is defined by Eq. (5.27) with n replaced by ℓ . Using this equation we can write linear equations for $\mathcal{G}_{1\ell}$ and $\mathcal{G}_{1,\ell+1}$ in the block form as,

$$I_2 - i\gamma\omega \mathcal{G}_{11} = \mathcal{G}_{1\ell} kP_\ell - \mathcal{G}_{1,\ell+1} kP_{\ell-1}, \quad (5.36)$$

$$\mathcal{G}_{11} = \mathcal{G}_{1\ell} Q_\ell - \mathcal{G}_{1,\ell+1} Q_{\ell-1}. \quad (5.37)$$

\mathcal{G}_{11} is obtained via Eq. (5.31). This set of equation seems complicated to simplify further but when evaluated numerically, for an ordered chain, we obtain the results given in Fig (5.1). The temperature in the bulk is the same as for zero magnetic field case, $(T_L + T_R)/2$ and the magnetic field mostly effects the profile near the ends of the chain.

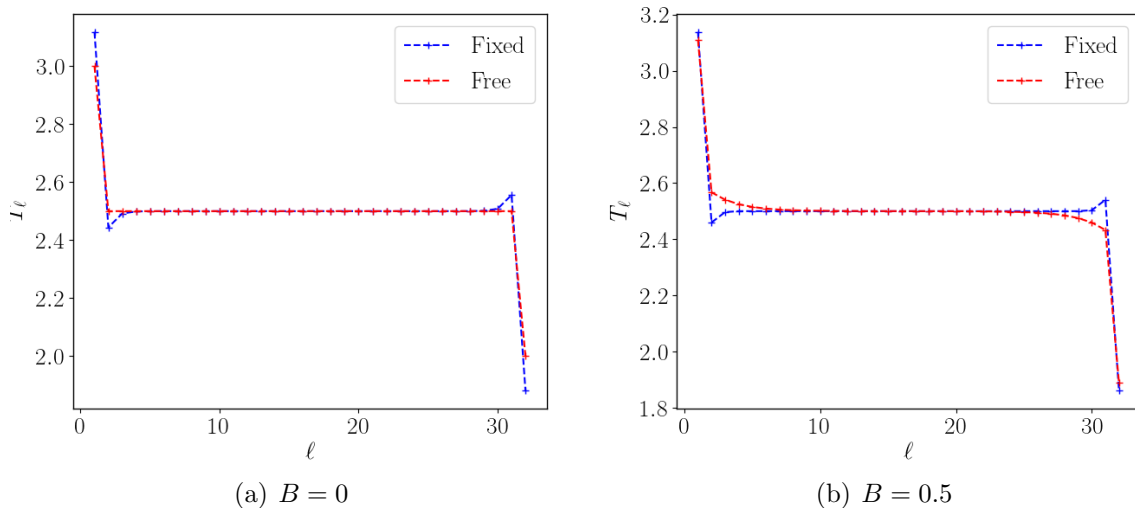


Figure 5.1: Temperature distribution for the ordered chain. Parameter values — $e = m = k = 1, N = 32, T_L = 3.5, T_R = 1.5$.

5.2 Expressions for the current in the thermodynamic limit for the uniform magnetic field case

We consider a uniform chain ($B_n = B$ for all $n = 1, 2, \dots, N$) and derive the expressions for the current in the thermodynamic limit,

$$J_\infty = \lim_{N \rightarrow \infty} J_N,$$

for the cases of fixed boundary conditions and free boundary conditions.

For the infinite system, the phonon spectrum consists of two bands $\{\omega^\pm(q) ; q \in (0, \pi)\}$ where $2m\omega^\pm(q) = \pm eB + \sqrt{(eB)^2 + 8mk(1 - \cos q)}$. The bands are gapped for $eB > \sqrt{2mk}$. In Fig. (5.2a) and Fig. (5.2b) we show the spectrum for $eB < \sqrt{2mk}$ and $eB > \sqrt{2mk}$ respectively. In the former, the bands overlap while in the latter they are gapped. We expect the transmission to be zero outside the bandwidth of the two bands which becomes explicit in the thermodynamic limit. We will show that in the thermodynamic limit, the current expression in Eq. (5.33) is the sum of two terms due to the two frequency bands of the system. Also, in the small ω limit we will find that $\mathcal{T}_\infty(\omega) = \lim_{N \rightarrow \infty} \mathcal{T}_N(\omega)$ is equivalent

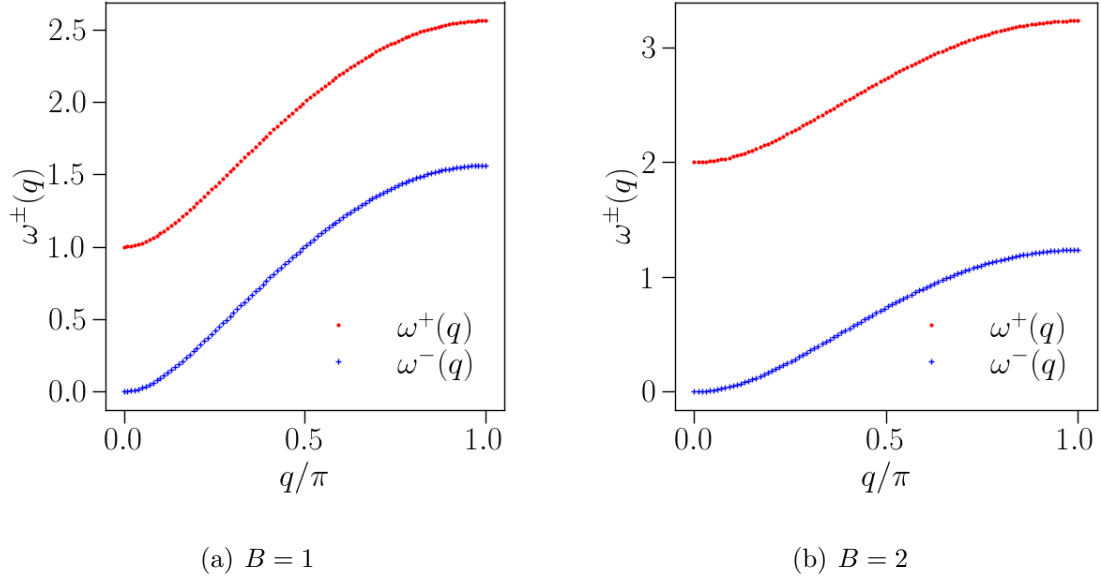


Figure 5.2: Spectrum of the chain in the bulk. Parameter values — $e = m = k = 1$.

to $\omega^{3/2}$ and $\omega^{1/2}$ for free and open boundary conditions respectively. We consider the two boundary conditions separately and set $k = e = 1$ without losing generality.

Fixed boundary conditions:

We have then $c_\ell = 2$ for all $\ell = 1, \dots, N$. The expressions for f_ℓ^\pm for free boundary conditions can be found exactly from Eq. (5.26). Recalling Eq. (5.25) let us denote $q^\pm := q^\pm(\omega) \in \mathbb{C}$ such that

$$2 \cos(q^\pm(\omega)) = a_\ell(\omega) \pm b_\ell(\omega) = 2 - m\omega^2 \pm B\omega. \quad (5.38)$$

We obtain

$$f_\ell^\pm = \frac{\sin[q_\pm(\ell + 1)]}{\sin q_\pm} \quad \text{and} \quad g_\ell^\pm = f_{\ell-1}^\pm \quad (\text{for } \ell \geq 1). \quad (5.39)$$

Recall Eq. (5.33). If ω is not in the frequencies band defined by ω^+ (resp. ω^-) then $q^+(\omega)$ (resp. $q^-(\omega)$) has a non-vanishing imaginary part and $F_N^+(\omega)$ (resp. $F_N^-(\omega)$) becomes exponentially large in N , so that these ω 's will not contribute in the thermodynamic limit

to the heat current.

We therefore obtain in the thermodynamic limit,

$$\begin{aligned} J_\infty &= (T_L - T_R) \frac{\gamma^2}{\pi} \lim_{N \rightarrow \infty} \int_{-\infty}^{\infty} d\omega \omega^2 \left[\frac{1}{|F_N^+(\omega)|^2} + \frac{1}{|F_N^-(\omega)|^2} \right] \\ &= (T_L - T_R) \frac{2\gamma^2}{\pi} \lim_{N \rightarrow \infty} \left\{ \int_0^\pi d\omega^+(q) \frac{[\omega^+(q)]^2}{|F_N^+(\omega^+(q))|^2} + \int_0^\pi d\omega^-(q) \frac{[\omega^-(q)]^2}{|F_N^-(\omega^-(q))|^2} \right\} \end{aligned}$$

where in the second equality, the 2 comes from the fact that by symmetry we restricted us to positive frequencies.

To obtain the limits, we follow the steps given in [68]. By using Eq. (5.32) and Eq. (5.39) we can express $F_N^\pm(\omega^\pm(q))$ as

$$\begin{aligned} F_N^\pm(\omega^\pm(q)) &= \frac{1}{\sin(q)} [\alpha^\pm(q) \sin(qN) + \beta^\pm(q) \cos(qN)], \\ \alpha^\pm(q) &= (1 - \gamma^2[\omega^\pm(q)]^2) \cos(q) + 2i\gamma\omega^\pm(q), \quad \beta^\pm(q) = (1 + \gamma^2[\omega^\pm(q)]^2) \sin(q). \end{aligned} \tag{5.40}$$

We have then to study the limit as $N \rightarrow \infty$ of

$$\int_0^\pi dq \frac{\partial \omega^\pm}{\partial q}(q) \frac{\sin^2(q)[\omega^\pm(q)]^2}{|\alpha^\pm(q) \sin(qN) + \beta^\pm(q) \cos(qN)|^2} = \int_0^\pi dq \frac{H^\pm(q)}{1 + R^\pm(q) \sin(2qN + \varphi^\pm(q))}$$

where

$$H^\pm(q) = \frac{2}{|\alpha^\pm(q)|^2 + |\beta^\pm(q)|^2} \frac{\partial \omega^\pm}{\partial q}(q) \sin^2(q)[\omega^\pm(q)]^2$$

and

$$R^\pm(q) \cos(\varphi^\pm(q)) = \frac{2 \operatorname{Re}(\alpha^\pm(q) \overline{\beta^\pm(q)})}{|\alpha^\pm(q)|^2 + |\beta^\pm(q)|^2}, \quad R^\pm(q) \sin(\varphi^\pm(q)) = \frac{|\alpha^\pm(q)|^2 - |\beta^\pm(q)|^2}{|\alpha^\pm(q)|^2 + |\beta^\pm(q)|^2}.$$

$\overline{\beta^\pm(q)}$ is the complex conjugate of $\beta^\pm(q)$. It can be shown [68, 69, 70] that

$$\lim_{N \rightarrow \infty} \int_0^\pi dq \frac{H^\pm(q)}{1 + R^\pm(q) \sin(2qN + \varphi^\pm(q))} = \int_0^\pi dq \frac{H^\pm(q)}{\sqrt{1 - [R^\pm(q)]^2}}.$$

	J_N		J_∞	
	Fixed BC	Free BC	Fixed BC	Free BC
$N = 10, B = 1$	0.179	0.160	0.179	0.158
$N = 20, B = 1$	0.179	0.158	0.179	0.158
$N = 10, B = 2$	0.163	0.121	0.163	0.131
$N = 20, B = 2$	0.163	0.131	0.163	0.131

Table 5.1: Comparison of numerical values of the current for finite N and the value of the current in the thermodynamic limit for $\gamma = 0.2$, $m = k = e = 1$, $T_L = 1, T_R = 0$.

Since we have that

$$\frac{1}{\sqrt{1 - [R^\pm]^2}} = \frac{|\alpha^\pm|^2 + |\beta^\pm|^2}{2|\text{Im}(\alpha^\pm\beta^\pm)|}$$

and

$$\text{Im}(\alpha^\pm(q)\overline{\beta^\pm(q)}) = 2\gamma\omega^\pm(q) (1 + \gamma^2[\omega^\pm(q)]^2) \sin(q) \geq 0 \quad \text{for } q \in (0, \pi),$$

we get that

$$\begin{aligned} & \lim_{N \rightarrow \infty} \int_0^\pi dq \frac{\partial\omega^\pm}{\partial q}(q) \frac{\sin^2(q)[\omega^\pm(q)]^2}{|\alpha^\pm(q)\sin(qN) + \beta^\pm(q)\cos(qN)|^2} \\ &= \frac{1}{2\gamma} \int_0^\pi dq \frac{\partial\omega^\pm}{\partial q}(q) \frac{\omega^\pm(q)\sin(q)}{1 + \gamma^2[\omega^\pm(q)]^2} = \frac{1}{2\gamma} \int_{\omega^\pm(0)}^{\omega^\pm(\pi)} d\omega \frac{\omega \sin(q^\pm(\omega))}{1 + \gamma^2\omega^2}. \end{aligned} \quad (5.41)$$

We conclude that

$$J_\infty = (T_L - T_R) \frac{\gamma}{\pi} \left\{ \int_{\omega^+(0)}^{\omega^+(\pi)} d\omega \frac{\omega \sin(q^+(\omega))}{1 + \gamma^2\omega^2} + \int_{\omega^-(0)}^{\omega^-(\pi)} d\omega \frac{\omega \sin(q^-(\omega))}{1 + \gamma^2\omega^2} \right\}. \quad (5.42)$$

The two integrals run over the two bands of the spectrum: $[\omega^-(0), \omega^-(\pi)] = [0, (-B + \sqrt{B^2 + 16m})/2m]$ and $[\omega^+(0), \omega^+(\pi)] = [B/2m, (B + \sqrt{B^2 + 16m})/2m]$. We see that in the thermodynamic limit the transmission is exactly zero at energy values outside the two bands of the spectrum and also the current is explicitly expressed as sum of two terms coming from the two bands. For small ω behaviour of the transmission, $\mathcal{T}_\infty(\omega)$, we take the contribution due to the lower band (depending on the sign of eB we have $\omega^+(0) = 0$ or $\omega^-(0) = 0$). It is straightforward to see from Eq. (5.42) that $\mathcal{T}_\infty(\omega) \sim \omega^{3/2}$ for $B \neq 0$ while for $B = 0$, $\mathcal{T}_\infty(\omega) \sim \omega^2$.

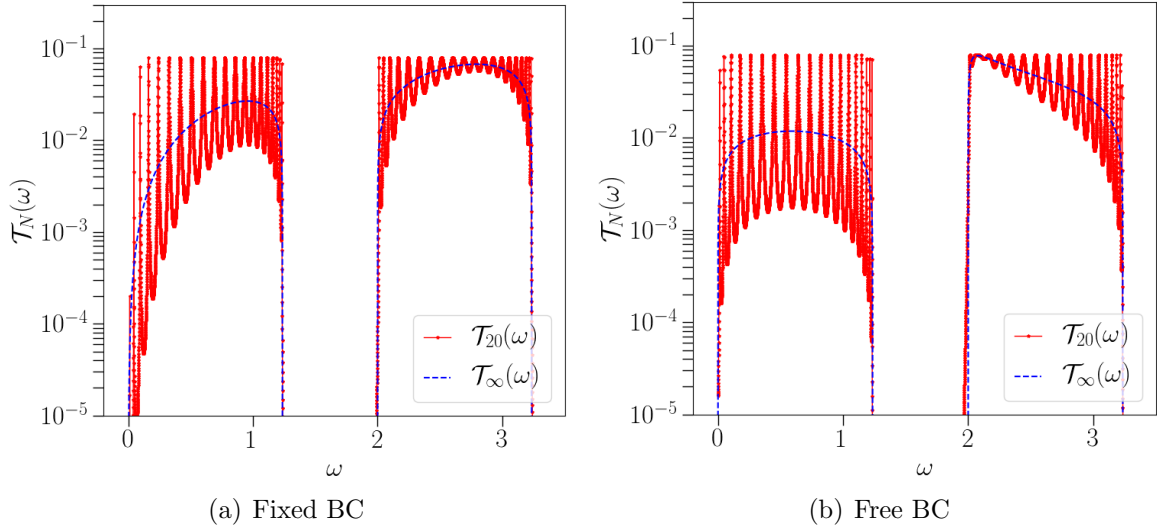


Figure 5.3: Comparison of the transmission $\mathcal{T}_N(\omega)$ for fixed and free boundary for $N = 20$ with $\mathcal{T}_\infty(\omega)$. Parameter values — $m = k = e = 1$, $\gamma = 0.2$ and $B = 2$.

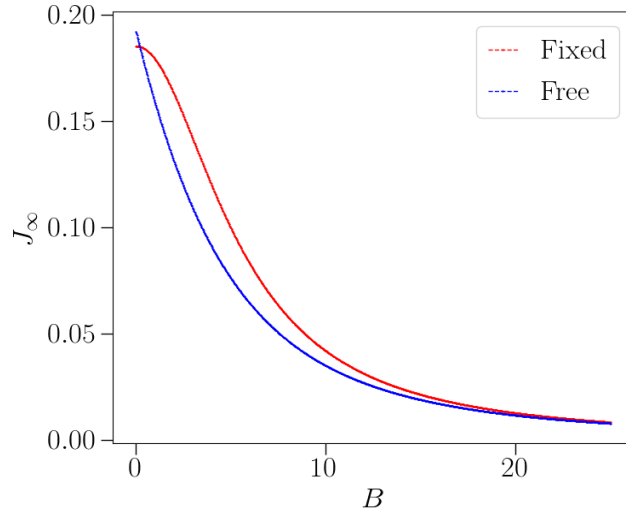


Figure 5.4: Variation of the current with the magnetic field. Parameter values — $e = m = k = 1$, $\gamma = 0.2$, $T_L = 1$, $T_R = 0$.

Free boundary conditions:

For free boundary conditions we have $c_\ell = 2 - \delta_{\ell,1} - \delta_{\ell,N}$. Recalling Eq. (5.25) and the definition of $q^\pm := q^\pm(\omega) \in \mathbb{C}$ the numbers f_ℓ^\pm, g_ℓ^\pm can once again be obtained with from

Eq. (5.26). We have

$$f_N^\pm = 2 \frac{(\cos(q_\pm) - 1)}{\sin(q_\pm)} \sin(q_\pm N), \quad g_{N-1}^\pm = \frac{\sin(q_\pm(N-1))}{\sin(q_\pm)},$$

$$\text{and } g_N^\pm = f_{N-1}^\pm = \frac{1}{\sin(q_\pm)} (\sin(q_\pm N) - \sin(q_\pm(N-1))),$$

where q^\pm is defined in Eq. (5.38). Using these we can express F_N^\pm defined by Eq. (5.32) as

$$F_N^\pm(\omega^\pm(q)) = \frac{1}{\sin(q)} [\alpha^\pm(q) \sin(qN) + \beta^\pm(q) \cos(qN)]$$

where

$$\alpha^\pm(q) = 2(\cos(q) - 1) - \gamma^2[\omega^\pm(q)]^2 \cos(q) + 2i\gamma\omega^\pm(q)(1 - \cos(q)),$$

$$\beta^\pm(q) = \gamma^2[\omega^\pm(q)]^2 \sin(q) + 2i\gamma\omega^\pm(q) \sin(q).$$

It has the same form as F_N^\pm appearing in Eq. (5.40) but with different expressions for α^\pm and β^\pm . Hence using the same method, and noticing that

$$\text{Im}(\alpha^\pm(q)\overline{\beta^\pm(q)}) = 2\gamma[\omega^\pm(q)]^2 \sin(q) [\mp B + (\gamma^2 + m)\omega^\pm(q)]$$

we deduce that

$$J_\infty = (T_L - T_R) \frac{\gamma}{\pi} \left\{ \int_{\omega^+(0)}^{\omega^+(\pi)} d\omega \frac{\sin(q^+(\omega))}{-B + (\gamma^2 + m)\omega} + \int_{\omega^-(0)}^{\omega^-(\pi)} d\omega \frac{\sin(q^-(\omega))}{B + (\gamma^2 + m)\omega} \right\}. \quad (5.43)$$

As in the case of fixed boundary condition, we have expressed the current as the sum of two integrals running over the two bands of the spectrum. However, from this expression, for small ω behaviour of $\mathcal{T}_\infty(\omega)$, the lower band gives $\mathcal{T}_\infty(\omega) \sim \omega^{1/2}$ and $\sim \omega^0$ for $B \neq 0$ and $B = 0$ respectively.

In Fig. (5.3a) and Fig. (5.3b), we show a comparison between $\mathcal{T}_\infty(\omega)$ derived for the two boundary conditions with the respect transmission obtained numerically for $N = 20$. It can be seen that the transmission in the thermodynamic limit looks exactly like the envelope

covered by the transmission for finite N . Table 1 shows the comparison of the numerically obtained current for $N = 10, 20$ and $B = 1, 2$ with the value of the current calculated from the Eq. (5.42) and Eq. (5.43) for the two boundary conditions respectively. These show a good agreement. We also show in Fig. (5.4) the variation of the current in thermodynamic limit J_∞ with respect to the magnetic field and we find that it decreases monotonically to 0 with the magnetic field B , as $1/B^2$ for large B , independently of the boundary conditions. We can also check easily that the limit $B \rightarrow 0$ and $N \rightarrow \infty$ commute, i.e. the limit of J_∞ as $B \rightarrow 0$ is equal to the normalised current of the ordered harmonic chain without magnetic field considered in [71, 72, 73, 68], for free and fixed boundary conditions.

5.3 Disordered magnetic field

In the Sec. 5.1, by using the non-equilibrium Green function formalism, we obtained an exact expression for the heat current, J_N , in the steady state of the chain for any spatial configuration of the magnetic field. We now consider the magnetic field to be disordered. We denote by $\langle J_N \rangle$ the expectation of the heat current with respect to the magnetic field distribution $\langle \cdot \rangle$ and our goal is to understand its scaling behavior in N .

Note that the iteration in equation Eq. 5.26 for $(f_n^-)_{n \geq 0}$ and $(g_n^-)_{n \geq 0}$ can now be thought in terms of the two dimensional discrete time Markov chain $(U_n)_{n \geq 0}$ given by

$$U_{n+1} = \begin{pmatrix} 2 - \omega^2 - \omega B_{n+1} & -1 \\ 1 & 0 \end{pmatrix} U_n, \quad \text{where } U_n := \begin{pmatrix} u_n \\ u_{n-1} \end{pmatrix} \quad \text{and } m = k = 1, \quad (5.44)$$

by choosing suitable initial conditions. By replacing the B_n 's by $-B_n$'s in the last display, we see that $(f_n^+)_{n \geq 0}$ and $(g_n^+)_{n \geq 0}$ can also be expressed in terms of $(U_n)_{n \geq 0}$. The state of the Markov chain is nothing but the result of a product of 2×2 product of independent and identically distributed random matrices. Roughly, the behaviour of F_N^\pm is related to the

growth of $\|U_N(\omega)\|$ which will be in the form $e^{2\lambda(\omega)N}$, where

$$\lambda(\omega) = \lim_{n \rightarrow \infty} \frac{1}{2n} \langle \log \|U_n(\omega)\| \rangle = \lim_{n \rightarrow \infty} \frac{1}{n} \langle \log |u_n(\omega)| \rangle > 0, \quad (5.45)$$

with $\langle \dots \rangle$ denoting a disorder average, is half the Lyapunov exponent associated to the Markov chain $(U_n)_{n \geq 0}$, or equivalently of the corresponding product of random matrices. The limit exists by Furstenberg's Theorem [74], is non-negative, independent of the initial condition U_0 and the limit holds in fact also for any realisation and not only by averaging over the magnetic field distribution.

For now we quickly discuss the effect of localization due to the random magnetic field on the heat transport and the need for calculating the Lyapunov exponent $\lambda(\omega)$ for small frequencies ω .

5.3.1 Effect of localization due to random magnetic field on the net Transmission

Using Eq. (5.14), we can calculate the net transmission $\mathcal{T}_N(\omega)$ for any spatial configuration of the magnetic field using a computer programme. In Fig. (5.5a) and Fig. (5.5b) we plot the net transmission function with ω for a uniform magnetic field and for a random magnetic field for different system sizes respectively. On comparison of the two plots, we can see that the randomness causes suppression of the net transmission and also the net transmission for the random magnetic field case goes down with system size while the system size has nearly no effect on the transmission for the uniform magnetic field. The suppression in case of random magnetic field is due to localization of the normal modes of the system. The normal modes of frequency ω get exponentially localized due to randomness with a localization length given by $1/\lambda(\omega)$ where $\lambda(\omega)$ is the Lyapunov exponent defined in Eq. (5.45). As a result of this they a priori do not contribute to the transmission. However, note that the transmission for random magnetic field is higher near $\omega = 0$ and goes down as we move away which means that the normal modes with energies closer to $\omega = 0$ have a larger localization length, i.e.

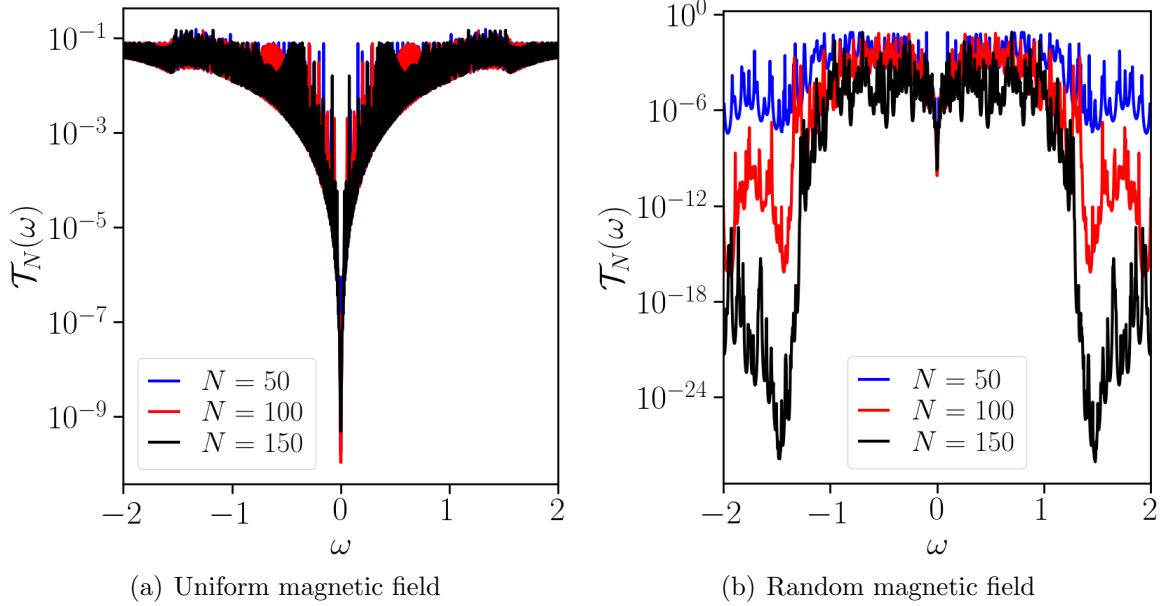


Figure 5.5: Variation of the net transmission, in units of $k_B = 1$, with ω for uniform magnetic field, panel (a), and random magnetic field, panel (b). The axes are in log scale and $\gamma = 0.2$. The magnetic field in (a) is set to be 1 on all oscillators and in (b) it was chosen uniformly from the interval $(0, 2)$. As can be seen clearly from the plots, the localization effects cause suppression of the transmission.

$\lambda(\omega) \rightarrow 0$ as $\omega \rightarrow 0$. Since we are eventually interested in the size dependence of the current, for large N , which is the integral of the transmission over all ω , we can reduce the integration limit to values of ω for which the localization length is greater than the system size. For the remaining ω values for which the localization length is less than the system size, the transmission would be negligible. Hence, we cut off the integral limit to $\omega = \omega_{max}^N$ where $1/\lambda(\omega_{max}^N) = N$ and the current is then given by

$$\langle J_N \rangle \approx 2(T_L - T_R) \int_0^{\omega_{max}^N} d\omega \lim_{N \rightarrow \infty} \langle \mathcal{T}_N(\omega) \rangle = 2(T_L - T_R) \int_0^{\omega_{max}^N} d\omega \mathcal{T}_\infty(\omega). \quad (5.46)$$

Note that the frequency ω_{max}^N would be very small for large N , and for such small frequencies we expect $\mathcal{T}_\infty(\omega)$ to have a weak dependence on disorder [since in the recursion Eq. (5.44), the randomness is multiplied by ω] — hence in the above equation $\mathcal{T}_\infty(\omega)$ is written without a disorder average and can in fact be determined by considering the chain in a *constant* magnetic field of strength $\langle B \rangle$. In Sec. 5.2, we showed that for constant magnetic field $\langle B \rangle \neq 0$, $\mathcal{T}_\infty(\omega) \sim \omega^{3/2}$ and $\sim \omega^{1/2}$ for fixed and free boundaries respectively, while for

$\langle B \rangle = 0$ it goes as ω^2 and ω^0 for the two boundary conditions respectively. To determine the size dependence of the current in addition to the small ω behaviour of $\mathcal{T}_\infty(\omega)$ we also need the small ω behaviour of $\lambda(\omega)$. We now proceed to the next section where we discuss the Lyapunov exponents of this equation.

5.3.2 Analysis of the Lyapunov exponents

In this section we present theoretical and numerical results on the asymptotics of Lyapunov exponents for small ω for the Markov processes defined by Eq. (5.44). The Lyapunov exponents are independent of the boundary conditions – so for this section we only work with fixed boundary conditions by setting $c_n = 2$ for all n – and of the initial condition of the process – i.e. it is the same for f_n^\pm and g_n^\pm . We show that Eq. (5.44) has three different behaviors for the Lyapunov exponent depending on the expected value $\langle B \rangle$ of the random magnetic field. For $\langle B \rangle > 0$ the Lyapunov exponent satisfies $\lambda(\omega) \sim \omega$ and for $\langle B \rangle < 0$, $\lambda(\omega) \sim \omega^{1/2}$. However, for $\langle B \rangle = 0$, $\lambda(\omega) \sim \omega^{2/3}$. Similar Lyapunov exponent behaviours are found for a harmonic oscillator with parametric noise, [75] and we will see that Eq. (5.44) could be written exactly in this form in the continuum limit.

Theoretical results for Lyapunov exponents

Let $(z_t)_{t \geq 0} \in \mathbb{R}^2$ be the solution of the following stochastic differential equation (with arbitrary initial condition)

$$\dot{z}_t = A_0 z_t + \varepsilon \sigma \xi_t A_1 z_t, \quad (5.47)$$

where ε is a small positive parameter, $\sigma > 0$ a constant, ξ_t a one dimensional standard white noise and A_0 and A_1 are 2×2 matrices such that

$$A_0 = \begin{pmatrix} 0 & 1 \\ -c & 0 \end{pmatrix}, \quad A_1 = \begin{pmatrix} 0 & 0 \\ -1 & 0 \end{pmatrix} \quad \text{with } c \in \mathbb{R}.$$

The Lyapunov exponent $\lambda_z(\varepsilon)$ of the process $(z_t)_{t \geq 0}$ is defined by

$$\lambda_z(\varepsilon) = \lim_{t \rightarrow \infty} \frac{1}{t} \langle \log \|z_t\| \rangle, \quad (5.48)$$

where $\langle \cdot \rangle$ denotes the expectation with respect to the white noise. It is proved in appendix 7.3 that if we denote $z_t = (u_t, v_t)^\perp$ then we have the Lyapunov exponent for $(u_t)_{t \geq 0}$ is the same as for $(z_t)_{t \geq 0}$:

$$\lambda_z(\varepsilon) = \lim_{t \rightarrow \infty} \frac{1}{t} \langle \log |u_t| \rangle. \quad (5.49)$$

The following result, proved in [76], gives the behaviour of the Lyapunov exponent $\lambda_z(\varepsilon)$ for small noise

1. If $c = 0$ then $\lambda_z(\varepsilon) = \hat{\lambda}(\sigma)\varepsilon^{2/3}$ where $\hat{\lambda}(\sigma)$ is defined in Eq. (7.41) .
2. If $c > 0$ then $\lambda_z(\varepsilon) \sim \frac{\sigma^2}{8c}\varepsilon^2$.
3. If $c < 0$ then $\lambda_z(\varepsilon) \sim \sqrt{|c|}$.

A sketch of the proof of this result is given in Appendix 7.3.

Consider now Eq. (5.44) defining the discrete time Markov chain $U_n = (u_n, u_{n-1})^\top$ and rewrite it in the following form, for small ω ,

$$u_{n+1} + u_{n-1} - 2u_n = -\omega \langle B \rangle u_n - \omega (B_{n+1} - \langle B \rangle) u_n + \mathcal{O}(\omega^2) .$$

In the continuum limit, the discrete time process $(u_n)_{n \geq 0}$ becomes then the continuous time process $(u_t)_{t \geq 0}$ solution of

$$\ddot{u}_t = -\omega \langle B \rangle u_t - \omega \sigma \xi_t u_t \quad (5.50)$$

where $(\xi_t)_{t \geq 0}$ is a standard white noise and σ^2 the variance of the $(B_n)_n$. Defining $w_t =$

$(u_t, \dot{u}_t)^\top$ we see that the previous equation reads

$$\dot{w}_t = \begin{pmatrix} 0 & 1 \\ -\omega \langle B \rangle & 0 \end{pmatrix} w_t + \sigma \omega \xi_t \begin{pmatrix} 0 & 0 \\ -1 & 0 \end{pmatrix} w_t . \quad (5.51)$$

We are interested in the Lyapunov exponent of the process $(u_t)_{t \geq 0}$ (or equivalently of the process $(w_t)_{t \geq 0}$ as said before):

$$\lambda_w(\omega) = \lim_{t \rightarrow \infty} \frac{1}{t} \langle \log \|w_t\| \rangle = \lim_{t \rightarrow \infty} \frac{1}{t} \langle \log |u_t| \rangle \quad (5.52)$$

Eq. (5.51) looks similar to Eq. (5.47) but to fit perfectly with Eq. (5.47) we perform the time scaling

$$\tilde{u}_t = u_{t/\sqrt{\omega}}$$

in Eq. (5.50) which gives by scaling invariance of white noise

$$\ddot{\tilde{u}}_t = -\langle B \rangle \tilde{u}_t - \omega^{1/4} \sigma \xi_t \tilde{u}_t \quad (5.53)$$

or equivalently for $\tilde{z}_t = (\tilde{u}_t, \dot{\tilde{u}}_t)^\top$ the equation

$$\dot{\tilde{z}}_t = \begin{pmatrix} 0 & 1 \\ -\langle B \rangle & 0 \end{pmatrix} \tilde{z}_t + \sigma \omega^{1/4} \xi_t \begin{pmatrix} 0 & 0 \\ -1 & 0 \end{pmatrix} \tilde{z}_t . \quad (5.54)$$

With the previous notation we have hence

$$\lambda_w(\omega) = \sqrt{\omega} \lambda_{\tilde{z}}(\omega^{1/4}) . \quad (5.55)$$

Eq. (5.54) fits perfectly Eq. (5.47) with $c = \langle B \rangle$ and $\varepsilon = \omega^{1/4}$. Then using point (i), (ii) and (iii) of Eq. (5.47) and Eq. (5.55) we get

1. If $\langle B \rangle = 0$, $\lambda_w(\omega) = \hat{\lambda}(\sigma) \omega^{2/3}$ where $\hat{\lambda}(\sigma)$ is defined in Eq. (7.41) .

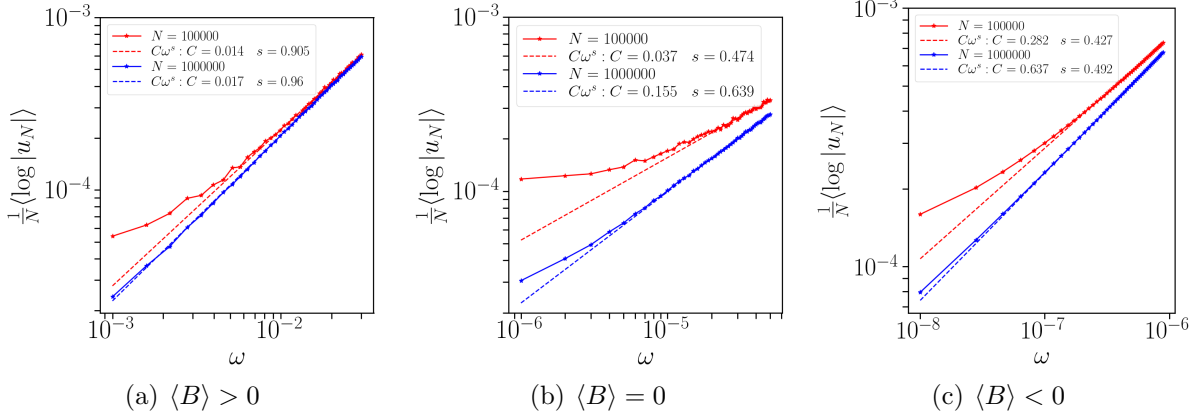


Figure 5.6: Variation of numerically calculated Lyapunov exponent, $\lambda = \frac{1}{N} \langle \log |u_N| \rangle$, with ω . $\langle \log |u_N| \rangle$ denotes average of $\log |u_N|$ over 100 realizations of the random magnetic field. For (a), (b) and (c) the magnetic fields were chosen randomly from the intervals $(0, 1)$, $(-1, 1)$ and $(-1, 0)$ respectively. The solid line is the data from the simulation while the dashed line is a power law fit, $C\omega^s$, to the data with C and s as fitting parameters. The obtained values of the fitting parameters agree appreciably with the theoretical values.

2. If $\langle B \rangle > 0$, $\lambda_w(\omega) \sim \frac{\sigma^2}{8\langle B \rangle} \omega$.
3. If $\langle B \rangle < 0$, $\lambda_w(\omega) \sim \sqrt{|\langle B \rangle|} \omega^{1/2}$.

It makes sense to believe that $\lambda(\omega)$ defined by Eq. (5.45) and $\lambda_w(\omega)$ defined by Eq. (5.52) have roughly the same behaviour as $\omega \rightarrow 0$ but a strong theoretical argument supporting this belief is missing. However, in the case $\langle B \rangle > 0$, we can obtain directly the behaviour of $\lambda(\omega)$ by following the approach of [77] and we observe then a good agreement at first order between $\lambda(\omega)$ and $\lambda_w(\omega)$, not only at the level of the exponent in ω but also at the level of the prefactor, see Table 5.2. Unfortunately we were not able to carry this approach for $\langle B \rangle < 0$ or $\langle B \rangle = 0$ and we decided hence to not pursue this approach. However numerical results presented in the next section support strongly the claim that $\lambda(\omega) \sim \lambda_w(\omega)$ for $\omega \rightarrow 0$.

Numerical results for Lyapunov exponents

We numerically calculate the Lyapunov exponents by using Eq. (5.26) to generate u_N for 100 realizations of the random magnetic field. The Lyapunov exponent would then be given by $\lambda = \frac{1}{N} \langle \log |u_N| \rangle$, where N is the number of oscillators. We plot in Fig. (5.6), the numerical

Case	Range of B_n	$s : \lambda(\omega) \sim C\omega^s$	C	$C_{\text{theoretical}}$
$\langle B \rangle > 0$ $\lambda(\omega) \sim \frac{\sigma^2}{8\langle B \rangle} \omega$	(0, 0.25)	0.986	0.0045	0.0052
	(0, 0.5)	0.999	0.0102	0.0104
	(0, 0.75)	1.0005	0.0156	0.0156
$\langle B \rangle < 0$ $\lambda(\omega) \sim \sqrt{ \langle B \rangle } \omega^{1/2}$	(-0.25, 0)	0.492	0.315	0.353
	(-0.5, 0)	0.492	0.444	0.5
	(-0.75, 0)	0.491	0.532	0.612
$\langle B \rangle = 0$ $\lambda(\omega) = \hat{\lambda}(\sigma) \omega^{2/3}$	(-0.25, 0.25)	0.658	0.073	0.079
	(-0.5, 0.5)	0.658	0.115	0.127
	(-0.75, 0.75)	0.649	0.136	0.167

Table 5.2: Comparison of analytical prefactor for the three cases with the numerical prefactor. For this table, $N = 10^7$.

data thus obtained for different ω and the power law fit, $C\omega^s$, for the data with C and s as fitting parameters. We see that the values of s obtained for the three cases, $\langle B \rangle > 0$, $\langle B \rangle < 0$ and $\langle B \rangle = 0$, agree reasonably well with the theoretically expected values. The prefactor, C , obtained for the three cases also seems to agree with the expected values from theory, see Table 5.2.

We now have the behaviour of the Lyapunov exponents at small ω for Eq. (5.26) and we found this to be different depending on the expectation value of the random magnetic field. The transmission is determined by f_N^+ as well as f_N^- and these two have different Lyapunov exponents for $\langle B \rangle \neq 0$, therefore the larger of the two exponents will dominate in the transmission. This is the Lyapunov exponent for f_N^- for $\langle B \rangle > 0$, while for $\langle B \rangle = 0$, f_N^+ and f_N^- have the same Lyapunov exponent. In the next section, we determine the size dependence of the current using these results for the Lyapunov exponents.

5.3.3 Size dependence of the current

We now have the small ω behaviour of $\lambda(\omega)$ for the transmission. We found this to be different for $\langle B \rangle \neq 0$ and $\langle B \rangle = 0$, so we expect different power laws for the current for the two cases. The boundary conditions will also play a role in the power law via the small ω behaviour of $\mathcal{T}_\infty(\omega)$. We therefore take the cases $\langle B \rangle \neq 0$ and $\langle B \rangle = 0$ separately for the

Boundary Conditions	Average magnetic field	$\mathcal{T}_\infty(\omega)$	$\lambda(\omega)$	Power law for the current $\langle J_N \rangle$
Fixed	$\langle B \rangle \neq 0$	$\sim \omega^{3/2}$	$\sim \omega$	$\sim 1/N^{5/2}$
Fixed	$\langle B \rangle = 0$	$\sim \omega^2$	$\sim \omega^{2/3}$	$\sim 1/N^{9/2}$
Free	$\langle B \rangle \neq 0$	$\sim \omega^{1/2}$	$\sim \omega$	$\sim 1/N^{3/2}$
Free	$\langle B \rangle = 0$	$\sim \omega^0$	$\sim \omega^{2/3}$	$\sim 1/N^{3/2}$

Table 5.3: Power law for the current for different boundary conditions and average magnetic fields.

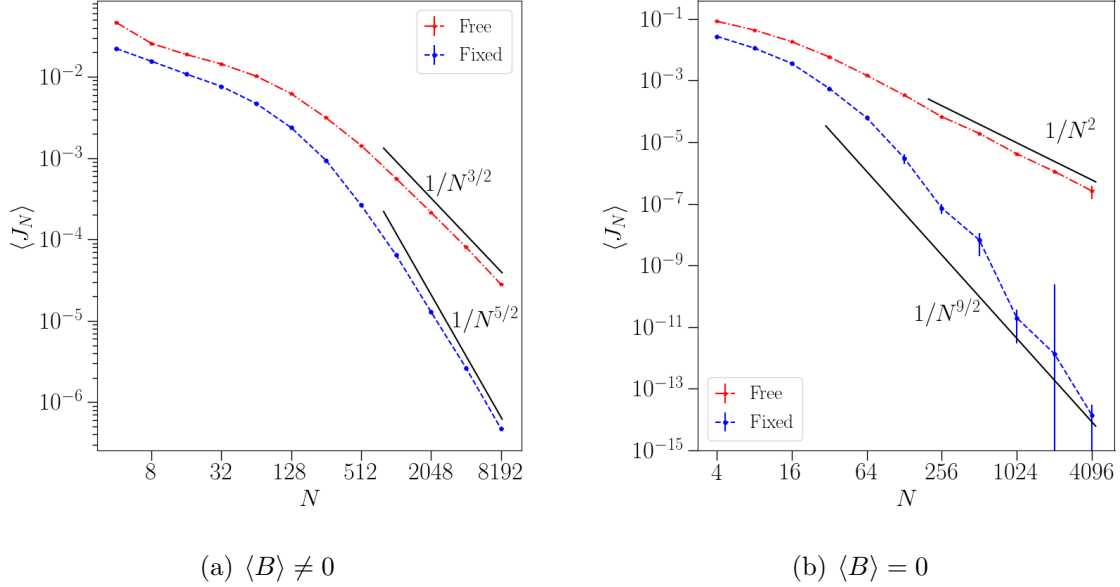


Figure 5.7: Numerically obtained power laws for the average current, averaged over 100 realizations of the disorder, with fixed and free boundary conditions. For $\langle B \rangle > 0$, B_n is chosen from $(1, 3)$ while for $\langle B \rangle = 0$, B_n is chosen from $(-2, 2)$.

two boundary conditions.

Fixed boundary conditions:

(a) For $\langle B \rangle \neq 0$, $\mathcal{T}_\infty(\omega) \sim \omega^{3/2}$ and $\lambda(\omega) \sim \omega$. Therefore using these in Eq. (5.46) we have $\langle J_N \rangle \sim 1/N^{5/2}$.

(b) For $\langle B \rangle = 0$, $\mathcal{T}_\infty(\omega) \sim \omega^2$ and $\lambda(\omega) \sim \omega^{2/3}$ which gives $\langle J_N \rangle \sim 1/N^{9/2}$.

Free boundary conditions:

(a) For $\langle B \rangle \neq 0$, $\mathcal{T}_\infty(\omega) \sim \omega^{1/2}$ and $\lambda(\omega) \sim \omega$ which gives $\langle J_N \rangle \sim 1/N^{3/2}$.

(b) For $\langle B \rangle = 0$, $\mathcal{T}_\infty(\omega) \sim \omega^0$ and $\lambda(\omega) \sim \omega^{2/3}$ which gives $\langle J_N \rangle \sim 1/N^{3/2}$.

The results are summarized in Table 5.3. Fig (5.7) shows the numerically obtained power laws for $\langle B \rangle \neq 0$ and $\langle B \rangle = 0$. Numerically, the power laws are obtained by calculating $\mathcal{T}_N(\omega)$ for different ω and then performing the integration numerically. We expect to see the power law behaviour at some large enough N . We see a reasonable agreement with the theoretically expected power laws except for the case with $\langle B \rangle = 0$ and free BC, where we get $\langle J_N \rangle \sim 1/N^2$ instead of the expected $\langle J_N \rangle \sim 1/N^{3/2}$.

The case with $\langle B \rangle = 0$ seems to be quite subtle because of the following reasons:

- The assumption that $\mathcal{T}_\infty(\omega)$ may be replaced by the transmission for the uniform case for small ω does not hold good for $\langle B \rangle = 0$ case. This can be clearly seen from Fig. (5.8), where we show a comparison of the transmission for small ω for $\langle B \rangle \neq 0$ and $\langle B \rangle = 0$ with their respective uniform cases. While $\langle B \rangle \neq 0$ shows a clear agreement with the corresponding uniform case, $\langle B \rangle = 0$ case shows a clear disagreement. It is not clear how to estimate $\mathcal{T}_\infty(\omega)$ for this case.
- Interestingly we note that the transmission coefficient has peaks at much lower frequencies than the ordered case. These peaks correspond to the normal modes of the isolated chain and it is then of interest to study the system size dependence of the lowest allowed normal mode frequency, ω_s^N , for the disordered chains with $\langle B \rangle \neq 0$ and $\langle B \rangle = 0$, and the ordered case with $B = 0$. In Fig. (5.9) we show the scaling of ω_s^N with N . We see that, for $\langle B \rangle \neq 0$, $\omega_{\max}^N \sim 1/N$ while $\omega_s^N \sim 1/N^2$. Thus, for any finite but large N , we have $\omega_{\max}^N > \omega_s^N$ and there are a sufficient number of conducting modes. On the other hand, for $\langle B \rangle = 0$, both ω_{\max}^N and ω_s^N scale as $1/N^{3/2}$ and this could be the reason why our heuristic approach for current scaling fails for this case.

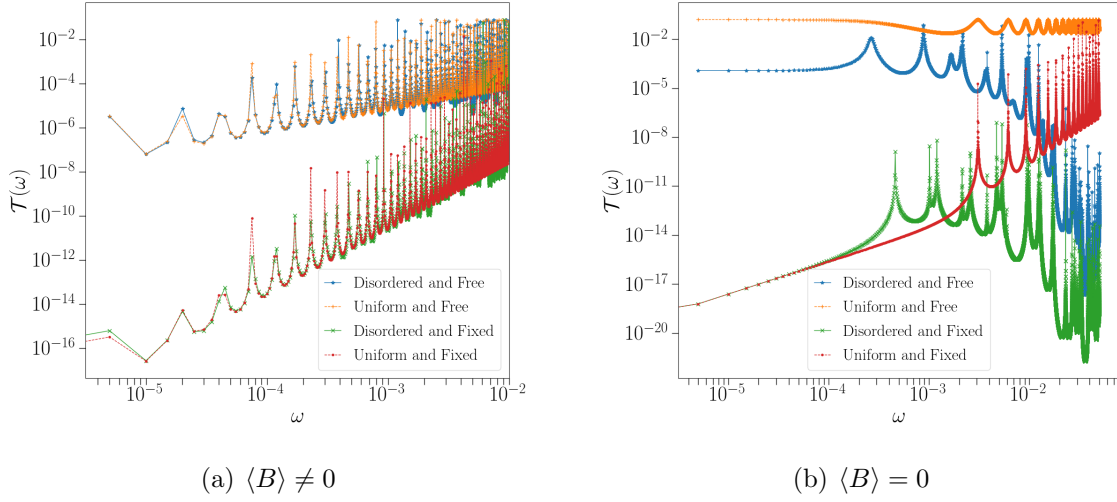


Figure 5.8: Comparison for the transmission for disordered and uniform cases for the two boundary conditions. For $\langle B \rangle \neq 0$, B_n is chosen from $(1, 3)$ while for $\langle B \rangle = 0$, B_n is chosen from $(-1, 1)$. These are compared with the transmission for the uniform cases with $B_n = \langle B \rangle$ respectively.

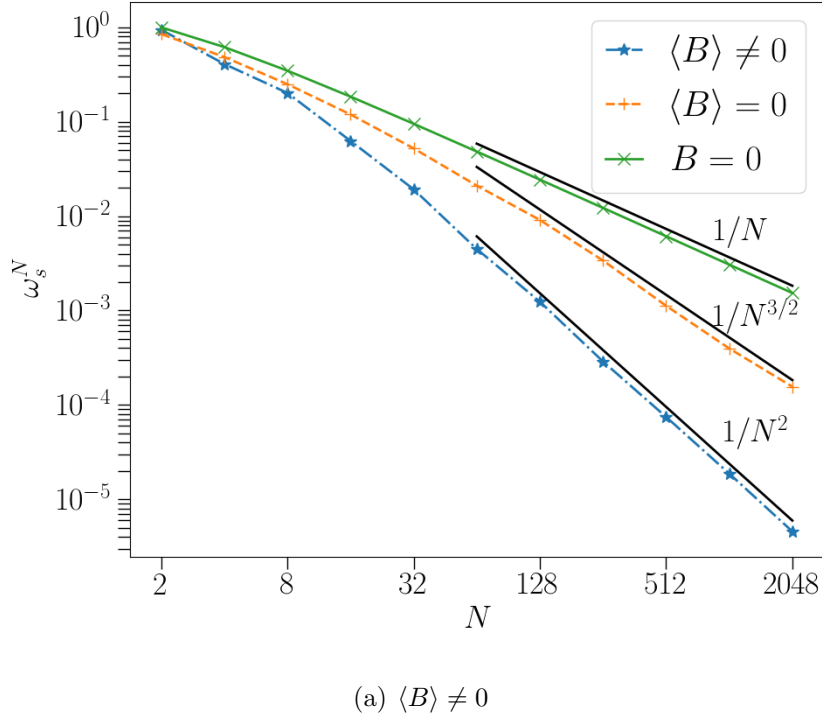


Figure 5.9: Scaling of lowest allowed normal mode, ω_s^N with the system size, N . For $\langle B \rangle \neq 0$, B_n is chosen from $(1, 3)$ while for $\langle B \rangle = 0$, B_n is chosen from $(-1, 1)$. The $B = 0$ plot corresponds to the ordered chain (the ordered case $B \neq 0$ is not shown and has the scaling N^{-2}).

5.4 Conclusion

In conclusion, we studied heat transport in an harmonic chain in the presence of a uniform and disordered magnetic field. Using non-equilibrium Green's function formalism we found that the heat current has contribution from two different terms involving two different Green's functions $G_1^+(\omega)$ and $G_2^+(\omega)$. for any spatial configuration of magnetic field. These can be interpreted physically as the transmission amplitude of a transverse plane wave being scattered without or with the $\pi/2$ rotation of its polarization respectively. This happens due to the fact that the magnetic field couples the x and y coordinates of the oscillators. We expressed the required components of the Green's functions as a product of 2×2 transfer matrices which we used to obtain explicit results for the uniform and random magnetic field cases. For the uniform case, in the thermodynamic limit, the currents become N -independent and we obtained analytic expressions for the current for free and fixed boundary conditions. These expressions show that at small ω and $B \neq 0$, the transmission, $\mathcal{T}_\infty(\omega) \sim \omega^{3/2}$ for fixed boundary and $\mathcal{T}_\infty(\omega) \sim \omega^{1/2}$ for free boundary.

We next considered the case where the magnetic field is disordered and derived power laws for the current with respect to the system size. The power laws were found to be sensitive to boundary conditions and the expectation value of the magnetic field. This was understood as arising from the different behaviour of the Lyapunov exponent $\lambda(\omega)$ and $\mathcal{T}_\infty(\omega)$ for small frequency ω . The small ω behaviour of $\mathcal{T}_\infty(\omega)$ was approximated to be the same as for the uniform case which was dependent on the boundary conditions imposed on the chain. To estimate the Lyapunov exponent we mapped the discrete time process which determines the Green's functions to the motion of a harmonic oscillator with parametric noise. This not only revealed an interesting connection between the Lyapunov exponents of the two systems but also showed that the Lyapunov exponent have different behaviour for different expectation values of the magnetic field. For $\langle B \rangle > 0$, $\langle B \rangle = 0$ and $\langle B \rangle < 0$ we find that the Lyapunov exponents were of order ω , $\omega^{2/3}$ and $\omega^{1/2}$ respectively. These behaviours of the Lyapunov exponent were also verified numerically. Using the results for the $\mathcal{T}_\infty(\omega)$ and $\lambda(\omega)$, we make analytic predictions of different system-size dependences of the current,

depending on the expectation value of the magnetic field and the boundary conditions. For free boundary conditions the current decreases as $1/N^{3/2}$ irrespective of the expectation value of the magnetic field. However, for fixed boundary conditions the current decreases as $1/N^{3/2}$ and $1/N^{9/2}$ for $\langle B \rangle \neq 0$ and $\langle B \rangle = 0$ respectively. Our direct numerical estimates show disagreement for the case $\langle B \rangle = 0$, and this is especially clear for the case with free boundary conditions. We discussed possible reasons for the disagreement, amongst which is the intriguing numerical observation of the $1/N^{3/2}$ system-size dependence of the lowest normal mode frequency for the $\langle B \rangle = 0$ case. The resolution of this issue remains an interesting outstanding problem.

Chapter 6

Conclusions

In this thesis, we looked at transport characteristics of models hosting topological phases in open system geometries. These models support special edge modes, within topologically non-trivial parameter regimes, that can carry dissipation less edge currents and are robust, to a certain degree, to symmetry preserving disorder. Due to the edge modes, topological phases possess quantized transport properties and therefore, the transport in such models lies in the ballistic regime. In this regime, the role of the reservoirs and their coupling with the system play an important role and thus, a microscopic modeling of the reservoirs and its contacts with the system become important. To that end, the NEGF formalism is a powerful tool and we used this formalism to study transport characteristics of some models hosting topological phases and a classical model, namely a chain of harmonic oscillators in presence of a magnetic field.

In chapter 2, we first considered a general model for a spinless superconducting wire in contact with reservoirs kept initially at some chemical potentials and temperatures. Using the NEGF formalism, we derived an exact solution for the nonequilibrium steady state of the wire. From this solution, we obtained compact expressions for particle, heat currents and other two point correlators of the model. These expressions were put in standard Landauer form from which the physical interpretations of the different terms became explicit. The physical interpretation was given in terms of the scattering amplitudes of different scattering processes namely the

normal transmission, Andreev transmission and the Andreev reflection. We also looked at other features such as the corrections of high energy bound states to the nonequilibrium steady state.

As application of this formalism we considered transport properties of the 1D nearest neighbour Kitaev chain and next-to-nearest neighbour Kitaev chain. We looked at particle and heat transport due to the topologically non-trivial bound states in these models. As expected from earlier studies [14, 15, 16], the particle conductance shows a zero bias peak of strength 2, in units of $e = h = 1$, attributed to the presence of the MBS. The thermal conductance, on the other hand, is zero deep within the topological phase but near the topological phase transition point, it shows a peak of strength $\pi^2 k_B^2 T/6$, where T is the temperature of the reservoirs. The next-to-nearest neighbour Kitaev chain hosts two different topological phases with one and two topological modes localized at each end. We find that this leads to multiple peaks in the conductance at the energies of these modes.

In chapter 3, we reconsidered the physical interpretation of different contributions to the heat and current expressions and analytically demonstrated the equivalence of different terms with the scattering amplitudes. The NEGF expressions involved multiple transmission coefficients namely $T_1(\omega)$, $T_2(\omega)$ and $T_3(\omega)$ which were shown to exactly equal the normal transmission, Andreev transmission and the Andreev reflection of a plane electron wave incident on the wire from one of the reservoirs, respectively.

In chapter 4, we considered a simple 2D model for a Chern insulator (SBHZ model) in contact with metallic leads at either ends. We looked at the quantization of the two-terminal conductance and the nature of the scattering states formed by the edge modes within the two-terminal setup. We verified that the two-terminal longitudinal conductance is quantized when the Fermi level is in the band gap of the insulator. We also looked at finite size effects of the quantized two-terminal conductance and find that the growth of the conductance, to the quantized value, shows oscillations as a function of both the system size and the system-reservoir coupling. The oscillation period shows a simple scaling with the system size and the coupling strength. A proof of the quantization in this open system geometry would be

desirable and remains an open problem.

To understand the nature of the scattering states formed by the edge modes, we looked at the charge density and the current density inside the insulator as well as inside the leads. We find that in the insulating region, the current density due to the edge modes is, as expected, localized along the boundaries of the sample. Remarkably, for the case when the reservoirs are in the vicinity of vanishing Fermi levels, we find that even inside the leads, the current density is highly localized and moves along zig-zag lines at 45° to the longitudinal direction. The current enters the insulator from one corner and leaves at the diagonally opposite corner.

In the last chapter, we considered heat transport due to a harmonic wire in presence of ordered and disordered magnetic fields. For the ordered case, we showed that the heat transmission at low frequencies is strongly modified due to the presence of magnetic field by obtaining the exact expressions for the heat current in the thermodynamic limit. We then considered the disordered magnetic field case where we were interested in the power law scaling of the disordered averaged current with the system size. This power law is determined by the low frequency behaviour of the localization length and the heat transmission. We showed that the frequency dependence Lyapunov exponent, inverse of the localization length, of this system is exactly the same as that of a harmonic oscillator with noisy frequency. The Lyapunov exponents were found to be dependent on whether expectation value of the magnetic field was zero or non-zero. Using the results for the Lyapunov exponents and assuming that the transmission at low frequencies is independent of the disorder, we found the current power laws are different for zero and non-zero expectation value of the magnetic field. Our direct numerical estimates for the power laws show disagreement for the case $\langle B \rangle = 0$, and this is especially clear for the case with free boundary conditions. We discussed possible reasons for the disagreement, amongst which is the intriguing numerical observation of the $1/N^{3/2}$ system-size dependence of the lowest normal mode frequency for the $\langle B \rangle = 0$ case. The resolution of this issue remains an interesting outstanding problem.

Chapter 7

Appendix

7.1 Derivation of the current expression

We present the derivation of the expression for the current in Eq. (2.39) here. We start by substituting Eq. (2.38) in Eq. (2.37) we get,

$$J_L = 2\text{Im}\left\{ \int d\omega d\omega' e^{i(\omega-\omega')t} \left\langle c_m^\dagger(\omega) \left\{ \eta_m^L(\omega') + [\Sigma_L^+(\omega')]_{ml} \tilde{c}_l(\omega') \right\} \right\rangle \right\} \quad (7.1)$$

Using Eq. (2.33) in the above expression we have, ra

$$\left\langle c_m^\dagger(\omega) \left\{ \eta_m^L(\omega') + [\Sigma_L^+(\omega')]_{ml} \tilde{c}_l(\omega') \right\} \right\rangle = A_1 + A_2 + A_3 + A_4 + A_5 \quad (7.2)$$

where,

$$A_1 = \int_{-\infty}^{\infty} \int_{-\infty}^{\infty} d\omega d\omega' e^{i(\omega-\omega')t} [G_1^-(\omega)]_{km} \left\langle \eta_k^{L\dagger}(\omega) \eta_m^L(\omega') \right\rangle = \int_{-\infty}^{\infty} d\omega \text{Tr} [G_1^-(\omega) \Gamma_L(\omega)] f_L(\omega)$$

$$\begin{aligned}
A_2 &= \int_{-\infty}^{\infty} \int_{-\infty}^{\infty} d\omega d\omega' e^{i(\omega-\omega')t} [G_1^-(\omega)]_{km} [\Sigma_L^+(\omega')]_{ml} [G_1^+(\omega')]_{lk'} \langle \eta_k^{L\dagger}(\omega) \eta_{k'}^L(\omega') \rangle \\
&= \int_{-\infty}^{\infty} d\omega \text{Tr} [G_1^-(\omega) \Sigma_L^+(\omega) G_1^+(\omega) \Gamma_L(\omega)] f_L(\omega)
\end{aligned} \tag{7.3}$$

$$\begin{aligned}
A_3 &= \int_{-\infty}^{\infty} \int_{-\infty}^{\infty} d\omega d\omega' e^{i(\omega-\omega')t} [G_1^-(\omega)]_{km} [\Sigma_L^+(\omega')]_{ml} [G_1^+(\omega')]_{lk'} \langle \eta_k^{R\dagger}(\omega) \eta_{k'}^R(\omega') \rangle \\
&= \int_{-\infty}^{\infty} d\omega \text{Tr} [G_1^-(\omega) \Sigma_L^+(\omega) G_1^+(\omega) \Gamma_R(\omega)] f_R(\omega)
\end{aligned} \tag{7.4}$$

$$\begin{aligned}
A_4 &= \int_{-\infty}^{\infty} \int_{-\infty}^{\infty} d\omega d\omega' e^{i(\omega-\omega')t} [G_2^-(\omega)]_{km} [\Sigma_L^+(\omega')]_{ml} [G_2^+(\omega')]_{lk'} \langle \eta_k^L(-\omega) \eta_{k'}^{L\dagger}(-\omega') \rangle \\
&= \int_{-\infty}^{\infty} d\omega \text{Tr} [G_2^-(\omega) \Sigma_L^+(\omega) G_2^+(\omega) \Gamma_L^T(-\omega)] (1 - f_L(-\omega))
\end{aligned} \tag{7.5}$$

$$\begin{aligned}
A_5 &= \int_{-\infty}^{\infty} \int_{-\infty}^{\infty} d\omega d\omega' e^{i(\omega-\omega')t} [G_2^-(\omega)]_{km} [\Sigma_L^+(\omega')]_{ml} [G_2^+(\omega')]_{lk'} \langle \eta_k^R(-\omega) \eta_{k'}^{R\dagger}(-\omega') \rangle \\
&= \int_{-\infty}^{\infty} d\omega \text{Tr} [G_2^-(\omega) \Sigma_L^+(\omega) G_2^+(\omega) \Gamma_R^T(-\omega)] (1 - f_R(-\omega))
\end{aligned} \tag{7.6}$$

The imaginary parts of A_1 , A_2 , A_3 , A_4 and A_5 can be shown to be the following,

$$\text{Im}\{A_1\} = \int_{-\infty}^{\infty} d\omega \text{Tr} \left[\frac{G_1^-(\omega) - G_1^+(\omega)}{2i} \Gamma_L(\omega) \right] f_L(\omega) \tag{7.7}$$

$$\frac{-1}{\pi} \text{Im}\{A_2\} = \int_{-\infty}^{\infty} d\omega \text{Tr} [G_1^-(\omega) \Gamma_L(\omega) G_1^+(\omega) \Gamma_L(\omega)] f_L(\omega) \tag{7.8}$$

$$\frac{-1}{\pi} \text{Im}\{A_3\} = \int_{-\infty}^{\infty} d\omega \text{Tr} [G_1^-(\omega) \Gamma_L(\omega) G_1^+(\omega) \Gamma_R(\omega)] f_R(\omega) \tag{7.9}$$

$$\frac{1}{\pi} \text{Im}\{A_4\} = \int_{-\infty}^{\infty} d\omega \text{Tr} [G_2^-(\omega) \Gamma_L(\omega) G_2^+(\omega) \Gamma_L^T(-\omega)] (f_L(-\omega) - 1) \tag{7.10}$$

$$\frac{1}{\pi} \text{Im}\{A_5\} = \int_{-\infty}^{\infty} d\omega \text{Tr} [G_2^-(\omega) \Gamma_L(\omega) G_2^+(\omega) \Gamma_R^T(-\omega)] (f_R(-\omega) - 1) \tag{7.11}$$

It is fairly straightforward to show that,

$$[G_1^-(\omega) - G_1^+(\omega)]/2i = \pi [G_1^+(\omega) (\Gamma_L(\omega) + \Gamma_R(\omega)) G_1^-(\omega) + G_2^+(\omega) (\Gamma_L^T(-\omega) + \Gamma_R^T(-\omega)) G_2^-(\omega)]$$

Substituting this result in Eq. (7.7) and adding up the imaginary parts of the terms A_1 , A_2 , A_3 , A_4 and A_5 , we obtain the required expression for the current entering the wire from the

left reservoir to be

$$J_L = \int_{-\infty}^{\infty} d\omega \left(T_1(\omega)(f_L^e(\omega) - f_R^e(\omega)) + T_2(\omega)(f_L^e(\omega) - f_R^h(\omega)) + T_3(\omega)(f_L^e(\omega) - f_L^h(\omega)) \right),$$

where $G_1^-(\omega) = [G_1^+(\omega)]^\dagger$, $G_2^-(\omega) = [G_2^+(\omega)]^\dagger$ and

$$T_1(\omega) = 4\pi^2 \text{Tr} [G_1^+(\omega) \Gamma_R(\omega) G_1^-(\omega) \Gamma_L(\omega)], \quad (7.12)$$

$$T_2(\omega) = 4\pi^2 \text{Tr} [G_2^+(\omega) \Gamma_R^T(-\omega) G_2^-(\omega) \Gamma_L(\omega)] \text{ and} \quad (7.13)$$

$$T_3(\omega) = 4\pi^2 \text{Tr} [G_2^+(\omega) \Gamma_L^T(-\omega) G_2^-(\omega) \Gamma_L(\omega)]. \quad (7.14)$$

7.2 Derivation of the expressions for bound state contribution to the correlators

To obtain the contribution of high energy bound states to the two point correlators we begin by considering form of the Hamiltonian written in Eq. 2.54. Clearly, the equations of motion for the entire system could be written as,

$$\begin{pmatrix} \dot{C}(t) \\ \dot{C}^\dagger(t) \end{pmatrix} = -i\mathcal{Z} \begin{pmatrix} C(t) \\ C^\dagger(t) \end{pmatrix} \quad (7.15)$$

where $C(t)$ and \mathcal{Z} are the same as in section 2.4. This directly gives us the full solution of to be,

$$c_i(t) = i[\mathcal{G}_1(t)]_{lm} c_m + i[\mathcal{G}_2(t)]_{lm} c_m^\dagger \quad (7.16)$$

where,

$$\mathcal{G}(t) = -ie^{-i\mathcal{Z}t} \theta(t) = \begin{pmatrix} \mathcal{G}_1(t) & \mathcal{G}_2(t) \\ \mathcal{G}_2^*(t) & \mathcal{G}_1^*(t) \end{pmatrix}. \quad (7.17)$$

We can also expand this Green's function in terms of the eigen vectors of the matrix \mathcal{Z} as,

$$[\mathcal{G}_1(t)]_{pq} = -i \sum_E e^{-iEt} \Psi_E(p) \Psi_E^*(q) \quad \text{and} \quad (7.18)$$

$$[\mathcal{G}_2(t)]_{pq} = -i \sum_E e^{-iEt} \Psi_E(p) \Phi_E^*(q). \quad (7.19)$$

where $\begin{pmatrix} \Psi_E \\ \Phi_E \end{pmatrix}$ is the eigenvector of the matrix \mathcal{Z} with energy E . In the long time limit, it can be shown that these expressions reduce to [33],

$$\lim_{t \rightarrow \infty} [\mathcal{G}_1(t)]_{pq} = -i \sum_{E_b} e^{-iE_b t} \Psi_{E_b}(p) \Psi_{E_b}^*(q) \quad \text{and} \quad (7.20)$$

$$\lim_{t \rightarrow \infty} [\mathcal{G}_2(t)]_{pq} = -i \sum_{E_b} e^{-iE_b t} \Psi_{E_b}(p) \Phi_{E_b}^*(q). \quad (7.21)$$

The sum now runs only over the bound states of the Hamiltonian. The Fourier transform of this green's function is given by,

$$\tilde{\mathcal{G}}(\omega) = \begin{pmatrix} \tilde{\mathcal{G}}_1(\omega) & \tilde{\mathcal{G}}_2(\omega) \\ \tilde{\mathcal{G}}_2^*(\omega) & \tilde{\mathcal{G}}_1^*(\omega) \end{pmatrix} = \frac{1}{\omega + i\epsilon - \mathcal{Z}} \quad (7.22)$$

Using these Green's function we can obtain the two point correlators of the system as a sum of the steady state contribution and the bound state contribution. To see this explicitly, we first need to relate the components Green's functions $\tilde{\mathcal{G}}_1(\omega)$ and $\tilde{\mathcal{G}}_2(\omega)$ with the Green's functions $G_1^+(\omega)$ and $G_2^+(\omega)$. Note that $G_1^+(\omega)$ and $G_2^+(\omega)$ are matrices of dimension N while $\tilde{\mathcal{G}}_1(\omega)$ and $\tilde{\mathcal{G}}_2(\omega)$ are matrices of dimension N_S . So, we split $\tilde{\mathcal{G}}_1(\omega)$ and $\tilde{\mathcal{G}}_2(\omega)$ as follows,

$$\tilde{\mathcal{G}}_1(\omega) = \begin{pmatrix} G_1^W(\omega) & G_1^{WL}(\omega) & G_1^{WR}(\omega) \\ G_1^{LW}(\omega) & G_1^L(\omega) & G_1^{LR}(\omega) \\ G_1^{RW}(\omega) & G_1^{RL}(\omega) & G_1^R(\omega) \end{pmatrix} \quad (7.23)$$

where the components of $G_1^W(\omega)$ are given by $[\tilde{\mathcal{G}}_1(\omega)]_{ij}$, the components of $G_1^{WL}(\omega)$ are given by $[\tilde{\mathcal{G}}_1(\omega)]_{i\alpha}$ and like wise for the other matrices in this equation. We remind the reader here

that i, j, m, n denote the sites on the wire while as α, μ, ν and α', μ', ν' denote left bath and right bath sites respectively. $\tilde{\mathcal{G}}_2(\omega)$ can be split similarly. We now rewrite Eq. 7.22 in the following block form,

$$\begin{pmatrix} \omega - H_W & -V_L & -V_R & -K & 0 & 0 \\ -V_L^\dagger & \omega - H_L & 0 & 0 & 0 & 0 \\ -V_R^\dagger & 0 & \omega - H_R & 0 & 0 & 0 \\ K^* & 0 & 0 & \omega + H_W^* & V_L^* & V_R^* \\ 0 & 0 & 0 & V_L^{\dagger*} & \omega + H_L^* & 0 \\ 0 & 0 & 0 & V_R^{\dagger*} & 0 & \omega + H_R^* \end{pmatrix} \begin{pmatrix} G_1^W & G_1^{WL} & G_1^{WR} & G_2^W & G_2^{WL} & G_2^{WR} \\ G_1^{LW} & G_1^L & G_1^{LR} & G_2^{LW} & G_2^L & G_2^{LR} \\ G_1^{RW} & G_1^{RL} & G_1^R & G_2^{RW} & G_2^{RL} & G_2^R \\ G_2^{W*} & G_2^{WL*} & G_2^{WR*} & G_1^{W*} & G_1^{WL*} & G_1^{WR*} \\ G_2^{LW*} & G_2^{L*} & G_2^{LR*} & G_1^{LW*} & G_1^{L*} & G_1^{LR*} \\ G_2^{RW*} & G_2^{RL*} & G_2^{R*} & G_1^{RW*} & G_1^{RL*} & G_1^{R*} \end{pmatrix} = I$$

From this we obtain the following required relations,

$$G_1^W(\omega) = G_1^+(\omega) \quad , \quad G_2^W(\omega) = G_2^+(-\omega) \quad (7.24)$$

$$G_1^{WL}(\omega) = G_1^+(\omega)V_L g_L^+(\omega) \quad (7.25)$$

$$G_1^{WR}(\omega) = G_1^+(\omega)V_R g_R^+(\omega) \quad (7.26)$$

$$G_2^{WL}(\omega) = G_2^+(-\omega)V_L^* g_L^{\dagger*}(\omega) \quad (7.27)$$

$$G_2^{WR}(\omega) = G_2^+(-\omega)V_R^* g_R^{\dagger*}(\omega) \quad (7.28)$$

We can now consider the two point correlators of the wire operators. Assuming initially that there is no correlation between the wire and the baths we can write these as,

$$\begin{aligned}
\langle c_l^\dagger(t)c_m(t) \rangle &= \sum_{\alpha\nu} \left[[\mathcal{G}_1^\dagger(t)]_{\alpha l} \langle c_\alpha^\dagger c_\nu \rangle [\mathcal{G}_1(t)]_{m\nu} + [\mathcal{G}_2^\dagger(t)]_{\alpha l} \langle c_\alpha c_\nu^\dagger \rangle [\mathcal{G}_2(t)]_{m\nu} \right] \\
&+ \sum_{\alpha'\nu'} \left[[\mathcal{G}_1^\dagger(t)]_{\alpha' l} \langle c_{\alpha'}^\dagger c_{\nu'} \rangle [\mathcal{G}_1(t)]_{m\nu'} + [\mathcal{G}_2^\dagger(t)]_{\alpha' l} \langle c_{\alpha'} c_{\nu'}^\dagger \rangle [\mathcal{G}_2(t)]_{m\nu'} \right] \\
&+ \sum_{ij} \left[[\mathcal{G}_1^\dagger(t)]_{il} \langle c_i^\dagger c_j \rangle [\mathcal{G}_1(t)]_{mj} + [\mathcal{G}_2^\dagger(t)]_{il} \langle c_i c_j^\dagger \rangle [\mathcal{G}_2(t)]_{mj} \right]
\end{aligned} \tag{7.29}$$

$$\begin{aligned}
\langle c_l(t)c_m(t) \rangle &= \sum_{\alpha\nu} \left[[\mathcal{G}_1(t)]_{l\alpha} \langle c_\alpha c_\nu^\dagger \rangle [\mathcal{G}_2(t)]_{m\nu} + [\mathcal{G}_2(t)]_{l\alpha} \langle c_\alpha^\dagger c_\nu \rangle [\mathcal{G}_1(t)]_{m\nu} \right] \\
&+ \sum_{\alpha'\nu'} \left[[\mathcal{G}_1(t)]_{l\alpha'} \langle c_{\alpha'} c_{\nu'}^\dagger \rangle [\mathcal{G}_2(t)]_{m\nu'} + [\mathcal{G}_2(t)]_{l\alpha'} \langle c_{\alpha'}^\dagger c_{\nu'} \rangle [\mathcal{G}_1(t)]_{m\nu'} \right] \\
&+ \sum_{ij} \left[[\mathcal{G}_2(t)]_{li} \langle c_i^\dagger c_j \rangle [\mathcal{G}_1(t)]_{mj} + [\mathcal{G}_1(t)]_{li} \langle c_i c_j^\dagger \rangle [\mathcal{G}_2(t)]_{mj} \right]
\end{aligned} \tag{7.30}$$

where $\langle c_p^\dagger c_q \rangle$ and $\langle c_p c_q^\dagger \rangle$, p, q denoting sites anywhere in the entire system, are the initial correlations of the system which are determined by the initial states of the reservoirs and the wire. Note that the full solution depends on the initial state of the wire. We assume that the wire operators are initially un-correlated i.e. $\langle c_i^\dagger c_j \rangle = 0$ and $\langle c_i c_j^\dagger \rangle = \delta_{ij}$ which is the same as choosing the initial state of the wire to be $|0\rangle\langle 0|$. The expressions in Eq. (7.24-7.28) enable the use of a similar algebra as in Ref. [33] to obtain,

$$\langle c_l^\dagger(t)c_m(t) \rangle = N_{lm}^{SS} + N_{lm}^{BS}(t) \quad \text{and} \tag{7.31}$$

$$\langle c_l(t)c_m(t) \rangle = M_{lm}^{SS} + M_{lm}^{BS}(t), \tag{7.32}$$

where N_{lm}^{SS} and M_{lm}^{SS} are the steady state contributions given by Eq. 2.51 and Eq. 2.52 respectively. $N_{lm}^{BS}(t)$ and $M_{lm}^{BS}(t)$ are the bound state contributions to these correlators which are defined by Eq. 2.62 and Eq. 2.63 respectively.

7.3 Lyapunov exponent for a harmonic oscillator with parametric noise

In order to obtain an expansion of $\lambda_z(\varepsilon)$ we follow the strategy developed by Pardoux et al. in [78] and by Wihstutz in [79]. The first step of the proof is to use the ergodic theorem to obtain an explicit formula (see Eq. (7.38)) for $\lambda_z(\varepsilon)$ instead of Eq. (5.48). In the second step we perform a perturbation analysis in ε with this new expression.

First we express the solution of the 2-dimensional SDE $(z_t)_{t \geq 0}$ in terms of a 1-dimensional SDE. Define $(\theta_t)_{t \geq 0}$ to be the solution of

$$\dot{\theta}_t = h_0(\theta_t) + \frac{1}{2}\varepsilon^2 \partial_\theta h_1(\theta_t) h_1(\theta_t) + \varepsilon h_1(\theta_t) \xi_t, \quad (7.33)$$

with

$$h_0(\theta) = \sin^2(\theta)(c-1) - c \quad \text{and} \quad h_1(\theta) = -\sigma \cos^2(\theta). \quad (7.34)$$

One can check that

$$z_t = R_t (\cos(\theta_t), \sin(\theta_t))^\top$$

where

$$R_t = \|z_0\| \exp \left(\int_0^t [q_0(\theta_\tau) + \varepsilon^2 r(\theta_\tau)] d\tau - \varepsilon \int_0^t q_1(\theta_\tau) \xi_\tau d\tau \right), \quad (7.35)$$

with

$$q_0(\theta) = (1-c) \cos(\theta) \sin(\theta), \quad q_1(\theta) = \sigma^2 \cos(\theta) \sin(\theta), \quad (7.36)$$

$$r(\theta) = \frac{\sigma^2 \cos^2(\theta)}{2} [2 \cos^2(\theta) - 1]. \quad (7.37)$$

Observe that $\|z_t\| = R_t$. Moreover, since in Eq. (7.33) the noise is vanishing exactly at the points $\theta_k^* = (2k+1)\pi/2$, $k \in \mathbb{Z}$, and that the drift in Eq. (7.33) at θ_k^* is equal to -1 , we see that starting from $\theta_0 \in [\theta_{k-1}^*, \theta_k^*)$ the process $(\theta_t)_{t \geq 0}$ will pass successively in the intervals

$\theta_0 \in [\theta_\ell^*, \theta_{\ell+1}^*)$ for $\ell \leq k-1$ without coming back to an interval previously visited. This defines a sequence of random times $t_\ell = \inf\{t \geq 0 ; \theta_t \in [\theta_{k-\ell-1}^*, \theta_{k-\ell}^*)\}$ for $\ell \geq 0$ with $t_0 = 0$. The process is thus clearly not ergodic. A simple way to restore this ergodicity (that will be needed later) is to consider the process $(\tilde{\theta}_t)_{t \geq 0}$, living in $[-\pi/2, \pi/2)$, and defined by $\tilde{\theta}_t = \theta_t + (k-\ell)\pi$ for $t \in [t_\ell, t_{\ell+1})$. The process $\tilde{\theta}_t$ satisfies the same stochastic differential equation as $(\theta_t)_{t \geq 0}$ but when it reaches $-\pi/2$ it is immediately reset to $\pi/2$. Equivalently $(\tilde{\theta}_t)_{t \geq 0}$ is solution of Eq. (7.33) but seen as a SDE on the torus $[-\pi/2, \pi/2)$ where the two end points of the interval have been identified. The process $(\tilde{\theta}_t)_{t \geq 0}$ has now the nice property to be ergodic. We denote by $\rho_\varepsilon(\theta)d\theta$ its invariant measure which is computed below. Observe moreover that Eq. (7.35) still holds by replacing θ by $\tilde{\theta}$ because the functions q_0, q_1, r are π -periodic. In order to keep notation simple we denote in the sequel the process $\tilde{\theta}$ by θ .

By definition (5.48) of Lyapunov exponent and Eq. (7.35) we get that

$$\begin{aligned} \lambda_z(\varepsilon) &= \lim_{t \rightarrow \infty} \frac{1}{t} \left\langle \int_0^t [q_0(\theta_\tau) + \varepsilon^2 r(\theta_\tau)] d\tau + \varepsilon \int_0^t q_1(\theta_\tau) \xi_\tau d\tau \right\rangle \\ &= \lim_{t \rightarrow \infty} \frac{1}{t} \left\langle \int_0^t [q_0(\theta_\tau) + \varepsilon^2 r(\theta_\tau)] d\tau \right\rangle, \end{aligned}$$

since $\langle \int_0^t q_1(\theta_\tau) \xi_\tau d\tau \rangle = 0$. Then by using the ergodic theorem we obtain

$$\lambda_z(\varepsilon) = \int_{-\pi/2}^{\pi/2} [q_0(\theta) + \varepsilon^2 r(\theta)] \rho_\varepsilon(\theta) d\theta. \quad (7.38)$$

The expansion in ε for $\lambda_z(\varepsilon)$ can then be obtained from the expansion of ρ_ε .

Before doing this we prove Eq. (5.49), i.e. that the process $(z_t)_{t \geq 0} = ((u_t, v_t)^\top)_{t \geq 0}$ and the process $(u_t)_{t \geq 0}$ have the same Lyapunov exponent. By definition we have

$$\lim_{t \rightarrow \infty} \frac{1}{t} \langle \log |u_t| \rangle = \lim_{t \rightarrow \infty} \frac{1}{t} \langle \log \|z_t\| \rangle + \lim_{t \rightarrow \infty} \frac{1}{t} \langle \log |\cos(\theta_t)| \rangle. \quad (7.39)$$

Since (θ_t) is an ergodic process we obtain that

$$\lim_{t \rightarrow \infty} \frac{1}{t} \langle \log |\cos(\theta_t)| \rangle = \lim_{t \rightarrow \infty} \frac{1}{t} \int_{-\pi/2}^{\pi/2} \rho_\varepsilon(\theta) \log(|\cos(\theta)|) d\theta = 0 .$$

This proves the claim.

Let us now compute ρ_ε which is the solution of the stationary Fokker-Planck equation

$$\partial_\theta \left[\frac{\varepsilon^2}{2} \partial_\theta (h_1^2 \rho_\varepsilon) - (h_0 + \frac{\varepsilon^2}{2} h_1 \partial_\theta h_1) \rho_\varepsilon \right] = 0 . \quad (7.40)$$

If we look for a solution such that $\frac{\varepsilon^2}{2} \partial_\theta (h_1^2 \rho_\varepsilon) - (h_0 + \frac{\varepsilon^2}{2} h_1 \partial_\theta h_1) \rho_\varepsilon = 0$ we get

$$\rho_\varepsilon(\theta) \propto \cos^{-2}(\theta) e^{-\frac{2\varepsilon^{-2}}{3\sigma^2} \tan^3(\theta) - \frac{2c\varepsilon^{-2}}{\sigma^2} \tan(\theta)}$$

which is not normalisable. Hence we have to look for a normalisable solution such that $\frac{\varepsilon^2}{2} \partial_\theta (h_1^2 \rho_\varepsilon) - (h_0 + \frac{\varepsilon^2}{2} h_1 \partial_\theta h_1) \rho_\varepsilon = A$ for some constant A . We get then that

$$\rho_\varepsilon(\theta) = Z_\varepsilon^{-1} v_\varepsilon(\theta) \cos^{-2}(\theta) \int_{-\infty}^{\tan(\theta)} \exp \left(\frac{2\varepsilon^{-2}}{3\sigma^2} u^3 + \frac{2c\varepsilon^{-2}}{\sigma^2} u \right) du$$

with

$$v_\varepsilon(\theta) = \exp \left\{ -\frac{2\varepsilon^{-2}}{3\sigma^4} \tan^3(\theta) - \frac{2c\varepsilon^{-2}}{\sigma^4} \tan(\theta) \right\}$$

and Z_ε the partition function making ρ_ε a probability. Injecting this in Eq. (7.38) we may derive the results claimed by a careful saddle point analysis. We prefer instead to rely on a more heuristic analysis to bypass boring computations.

It is natural to expect that as $\varepsilon \rightarrow 0$ the stationary measure $\rho_\varepsilon(\theta) d\theta$ will converge to the one of $\dot{\theta}_t = h_0(\theta_t)$ (i.e. Eq. (7.33) with $\varepsilon = 0$). However as we will see this deterministic dynamical system has different behaviours depending on the value of c and that in some cases we have also to compute the next order corrections.

If $c > 0$, the deterministic dynamical system has a unique invariant state $\rho_0(\theta)d\theta$ with $\rho_0(\theta) = -\frac{\sqrt{c}}{\pi}h_0^{-1}(\theta)$ because h_0 never vanishes on $[-\pi/2, \pi/2)$. Hence $\rho_\varepsilon \rightarrow \rho_0$ as $\varepsilon \rightarrow 0$. However, since $\int_0^\pi q_0(\theta)\rho_0(\theta)d\theta = 0$, we have to expand ρ_ε at order ε^2 to obtain the behavior of λ_ε in Eq. (7.38). Let us assume that $\rho_\varepsilon = \rho_0 + \varepsilon^2\delta\rho_0 + o(\varepsilon^2)$, inject this in Eq. (7.40) and identify the powers in ε . We obtain that

$$\partial_\theta[h_0(\delta\rho_0)] = \frac{1}{2}\partial_\theta[\partial_\theta(h_1^2\rho_0) - (h_1\partial_\theta h_1)\rho_0]$$

which implies, since $\int_{-\pi/2}^{\pi/2}(\delta\rho_0)(\theta)d\theta = 0$ that

$$\delta\rho_0 = \frac{A}{h_0} + \frac{1}{2h_0}[\partial_\theta(h_1^2\rho_0) - (h_1\partial_\theta h_1)\rho_0].$$

We deduce that

$$\delta\rho_0 = \frac{A}{h_0} + \frac{\sigma^2\sqrt{c}}{\pi}\left(\frac{\sin(\theta)\cos^3(\theta)}{h_0^2} + (c-1)\left(\frac{\cos^5(\theta)\sin(\theta)}{h_0^3(\theta)}\right)\right).$$

Since $\int_{-\pi/2}^{\pi/2}(\delta\rho_0)(\theta)d\theta = 0$ we obtain $A = 0$ and

$$\delta\rho_0 = \frac{\sigma^2\sqrt{c}}{\pi}\left(\frac{\sin(\theta)\cos^3(\theta)}{h_0^2} + (c-1)\left(\frac{\cos^5(\theta)\sin(\theta)}{h_0^3(\theta)}\right)\right).$$

Hence we get that

$$\lambda_z(\varepsilon) = \varepsilon^2 \int_{-\pi/2}^{\pi/2} (r(\theta)\rho_0(\theta) + q_0(\theta)\delta\rho_0(\theta)) d\theta + o(\varepsilon^2).$$

By the change of variable $x = \tan(\theta)$ we get

$$\begin{aligned} \int_{-\pi/2}^{\pi/2} r(\theta)\rho_0(\theta)d\theta &= \frac{\sigma^2\sqrt{c}}{2\pi} \int_{-\infty}^{\infty} \frac{x^2-1}{(1+x^2)(x^2+c)} dx = \frac{\sigma^2}{2(\sqrt{c}+1)^2}. \\ \int_{-\pi/2}^{\pi/2} q_0(\theta)\delta\rho_0(\theta)d\theta &= \sigma^2 \left(\frac{(4\sqrt{c}+1)(c-1)^2}{8(\sqrt{c}+1)^4c} + \frac{1-c}{2(\sqrt{c}+1)^3} \right). \end{aligned}$$

Hence we finally get

$$\lambda_z(\varepsilon) = \varepsilon^2 \frac{\sigma^2}{8c} + o(\varepsilon^2).$$

This proves case (ii).

If $c < 0$ then $\frac{c}{c-1} \in (0, 1)$ and the function h_0 vanishes on $[-\pi/2, \pi/2)$ if and only if $\theta \in [-\pi/2, \pi/2)$ is solution of

$$\sin^2(\theta) = \frac{c}{c-1}.$$

There are two solutions $\theta^* > 0$ and $-\theta^* < 0$. The deterministic dynamical has two extremal invariant probability measures given by $\delta_{\pm\theta^*}$. Since $h'_0(\theta^*) < 0 < h'_0(-\theta^*)$, $\delta_{-\theta^*}$ is unstable while δ_{θ^*} is stable. By introducing noise in this dynamical system the stable stationary state is selected when the intensity of the noise is sent to zero afterwards, i.e. $\rho_\varepsilon(\theta)d\theta \rightarrow \delta_{\theta^*}$. We conclude that

$$\lim_{\varepsilon \rightarrow 0} \lambda_z(\varepsilon) = q_0(\theta^*) = \sqrt{|c|}.$$

This proves case (iii).

The case $c = 0$ is more delicate. Since $h_0(\cdot) = -\sin^2(\cdot)$, the unique invariant measure for the deterministic dynamical system is δ_0 (stable) and we expect that $\rho_\varepsilon(\theta)d\theta \rightarrow \delta_0$ as $\varepsilon \rightarrow 0$. Observe however that $q_0(0) = 0$ so that we have to find the first correction to the approximation of ρ_ε to δ_0 . Due to the singularity of the Dirac mass we cannot perform an expansion analysis in ε . Hence we will use another argument to get item (i). Consider the following linear transformation $T_\varepsilon = \begin{pmatrix} \varepsilon^{2/3} & 0 \\ 0 & 1 \end{pmatrix}$ which is such that $\varepsilon^{2/3}\|z\| \leq \|T_\varepsilon z\| \leq \|z\|$ for any $z \in \mathbb{R}^2$ and $\varepsilon \leq 1$. This implies that $(z_t)_{t \geq 0}$ and $(T_\varepsilon z_t)_{t \geq 0}$ have the same Lyapunov exponent. Expressing as we did before

$$\hat{z}_t := T_\varepsilon z_t = \|\hat{z}_t\| (\cos \hat{\theta}_t, \sin \hat{\theta}_t)^\top$$

we notice that

$$\dot{\hat{\theta}}_t = \varepsilon^{2/3} \left(-\sin^2(\hat{\theta}_t) - \sigma^2 \sin(\hat{\theta}_t) \cos^3(\hat{\theta}_t) \right) - \varepsilon^{1/3} \sigma \cos^2(\hat{\theta}_t) \xi_t,$$

which implies by scaling invariance of the white noise that $\hat{\theta}_t = \alpha_{t\varepsilon^{2/3}}$ where

$$\dot{\alpha}_t = (-\sin^2(\alpha_t) - \sigma^2 \sin(\alpha_t) \cos^3(\alpha_t)) - \sigma \cos^2(\alpha_t) \xi_t .$$

If $\hat{\rho}(\alpha)d\alpha$ is the unique invariant measure for $(\alpha_t)_{t \geq 0}$ we have by a scaling argument that the Lyapunov exponent satisfies

$$\lambda_z(\varepsilon) = \varepsilon^{2/3} \hat{\lambda}(\sigma)$$

with

$$\hat{\lambda}(\sigma) = \int_{-\pi/2}^{\pi/2} (q_0(\alpha) + r(\alpha)) \hat{\rho}(\alpha) d\alpha, \quad (7.41)$$

where q_0 and r are defined respectively in Eq. (7.36) and Eq. (7.37) with $c = 0$. To obtain the value of $\hat{\lambda}(\sigma)$ it is sufficient to find $\hat{\rho}$ which is the unique normalisable function of the Fokker-Planck equation associated to the process $(\alpha_t)_{t \geq 0}$, i.e.

$$\hat{\rho}(\alpha) = \hat{Z}^{-1} \cos^{-2}(\alpha) e^{-\frac{2}{3\sigma^2} \tan^3(\alpha)} \int_{-\infty}^{\tan(\alpha)} \exp\left(\frac{2u^3}{3\sigma^2}\right) du ,$$

where \hat{Z} is the normalisation constant making $\hat{\rho}$ a probability measure.

Bibliography

- [1] M. Z. Hasan and C. L. Kane, *Reviews of modern physics* **82**, 3045 (2010).
- [2] J. E. Moore, *Nature* **464**, 194 (2010).
- [3] A. Agarwala, A. Haldar, and V. B. Shenoy, *Annals of physics* **385**, 469 (2017).
- [4] E. H. Hall *et al.*, *American journal of mathematics* **2**, 287 (1879).
- [5] D. Obana, F. Liu, and K. Wakabayashi, *Physical review B* **100**, 075437 (2019).
- [6] A. Y. Kitaev, *Physics-Uspekhi* **44**, 131 (2001).
- [7] F. D. M. Haldane, *Physical review letters* **61**, 2015 (1988).
- [8] B. A. Bernevig, T. L. Hughes, and S.-C. Zhang, *Science* **314**, 1757 (2006).
- [9] C. L. Kane and E. J. Mele, *Physical review letters* **95**, 146802 (2005).
- [10] G. Jotzu, M. Messer, R. Desbuquois, M. Lebrat, T. Uehlinger, D. Greif, and T. Esslinger, *Nature* **515**, 237 (2014).
- [11] M. König, S. Wiedmann, C. Brüne, A. Roth, H. Buhmann, L. W. Molenkamp, X.-L. Qi, and S.-C. Zhang, *Science* **318**, 766 (2007).
- [12] N. Read and D. Green, *Physical review B* **61**, 10267 (2000).
- [13] M. Sato, *Physics letters B* **575**, 126 (2003).
- [14] R. M. Lutchyn, J. D. Sau, and S. D. Sarma, *Physical review letters* **105**, 077001 (2010).

- [15] D. Roy, C. Bolech, and N. Shah, *Physical review B* **86**, 094503 (2012).
- [16] M. Thakurathi, O. Deb, and D. Sen, *Journal of physics: condensed matter* **27**, 275702 (2015).
- [17] A. Agarwala and V. B. Shenoy, *Physical review letters* **118**, 236402 (2017).
- [18] T. Peng, C.-B. Hua, R. Chen, D.-H. Xu, and B. Zhou, *Physical review B* **103**, 085307 (2021).
- [19] Z.-R. Liu, C.-B. Hua, T. Peng, and B. Zhou, *Physical review B* **105**, 245301 (2022).
- [20] A. Kitaev, *Annals of physics* **321**, 2 (2006).
- [21] J. Nasu, J. Yoshitake, and Y. Motome, *Physical review letters* **119**, 127204 (2017).
- [22] Z. Wang, X.-L. Qi, and S.-C. Zhang, *Physical review B* **84**, 014527 (2011).
- [23] K. Shiozaki and S. Fujimoto, *Physical review letters* **110**, 076804 (2013).
- [24] V. Mourik, K. Zuo, S. M. Frolov, S. Plissard, E. P. Bakkers, and L. P. Kouwenhoven, *Science* **336**, 1003 (2012).
- [25] A. Das, Y. Ronen, Y. Most, Y. Oreg, M. Heiblum, and H. Shtrikman, *Nature Physics* **8**, 887 (2012).
- [26] H. Zhang, M. W. de Moor, J. D. Bommer, D. Xu, G. Wang, N. van Loo, C.-X. Liu, S. Gazibegovic, J. A. Logan, D. Car, *et al.*, arXiv preprint arXiv:2101.11456 (2021).
- [27] H. Song, Z. Zhang, D. Pan, D. Liu, Z. Wang, Z. Cao, L. Liu, L. Wen, D. Liao, R. Zhuo, *et al.*, *Physical review research* **4**, 033235 (2022).
- [28] F. Nichele, A. C. Drachmann, A. M. Whiticar, E. C. O'Farrell, H. J. Suominen, A. Fornieri, T. Wang, G. C. Gardner, C. Thomas, A. T. Hatke, *et al.*, *Physical review letters* **119**, 136803 (2017).

- [29] D. J. Thouless, M. Kohmoto, M. P. Nightingale, and M. den Nijs, *Physical review letters* **49**, 405 (1982).
- [30] S. Datta, *Electronic transport in mesoscopic systems* (Cambridge university press, 1997).
- [31] A. Dhar and D. Roy, *Journal of statistical physics* **125**, 801 (2006).
- [32] A. Kamenev, *Field theory of non-equilibrium systems* (Cambridge University Press, 2023).
- [33] A. Dhar and D. Sen, *Physical review B* **73**, 085119 (2006).
- [34] L. Fu and C. L. Kane, *Physical review letters* **100**, 096407 (2008).
- [35] J. D. Sau, R. M. Lutchyn, S. Tewari, and S. D. Sarma, *Physical review letters* **104**, 040502 (2010).
- [36] Y. Oreg, G. Refael, and F. von Oppen, *Physical review letters* **105**, 177002 (2010).
- [37] J. D. Sau, S. Tewari, R. M. Lutchyn, T. D. Stanescu, and S. D. Sarma, *Physical review B* **82**, 214509 (2010).
- [38] V. Mourik, K. Zuo, S. M. Frolov, and S. Plissard, *Science* **336**, 1003 (2012).
- [39] A. Das, Y. Ronen, Y. Most, Y. Oreg, M. Heiblum, and H. Shtrikman, *Nature physics* **8**, 887 (2012).
- [40] M. Deng, C. Yu, G. Huang, M. Larsson, P. Caroff, and H. Xu, *Nano letters* **12**, 6414 (2012).
- [41] L. P. Rokhinson, X. Liu, and J. K. Furdyna, *Nature physics* **8**, 795 (2012).
- [42] A. Finck, D. J. Van Harlingen, P. Mohseni, K. Jung, and X. Li, *Physical review letters* **110**, 126406 (2013).
- [43] H. Churchill, V. Fatemi, K. Grove-Rasmussen, M. Deng, P. Caroff, H. Xu, and C. M. Marcus, *Physical review B* **87**, 241401 (2013).

- [44] G. Kells, D. Meidan, and P. Brouwer, *Physical review B* **86**, 100503 (2012).
- [45] H. Pan and S. D. Sarma, *Physical review research* **2**, 013377 (2020).
- [46] S. Frolov, *Nature* **592**, 350 (2021).
- [47] R. Shankar, arXiv preprint arXiv:1804.06471 (2018).
- [48] S. Tamaki, M. Sasada, and K. Saito, *Physical review letters* **119**, 110602 (2017).
- [49] K. Saito and M. Sasada, *Communications in mathematical physics* **361**, 951 (2018).
- [50] S. Tamaki and K. Saito, *Physical review E* **98**, 052134 (2018).
- [51] G. Basile, C. Bernardin, M. Jara, T. Komorowski, and S. Olla, In: Lepri S. (eds) *Thermal Transport in Low Dimensions. Lecture Notes in Physics* **291** (2016).
- [52] A. Sytcheva, U. Löw, S. Yasin, J. Wosnitza, S. Zherlitsyn, P. Thalmeier, T. Goto, P. Wyder, and B. Lüthi, *Physical review B* **81**, 214415 (2010).
- [53] R. Doornenbal, G. Skantzaris, and H. Stoof, *Physical review B* **91**, 045419 (2015).
- [54] A. M. Lobos and S. D. Sarma, *New journal of physics* **17**, 065010 (2015).
- [55] A. R. Akhmerov, J. P. Dahlhaus, F. Hassler, M. Wimmer, and C. W. J. Beenakker, *Physical review letters* **106**, 057001 (2011).
- [56] N. Bondyopadhyaya and D. Roy, *Journal of statistical physics* **187**, 11 (2022).
- [57] J.-P. Blaizot and G. Ripka, *Quantum theory of finite systems*, Vol. 3 (MIT press Cambridge, MA, 1986).
- [58] N. Bondyopadhyaya and D. Roy, *Physical review B* **99**, 214514 (2019).
- [59] Y. Niu, S. B. Chung, C.-H. Hsu, I. Mandal, S. Raghu, and S. Chakravarty, *Physical review B* **85**, 035110 (2012).
- [60] R. Nehra, A. Sharma, and A. Soori, *EPL (Europhysics letters)* **130**, 27003 (2020).

- [61] G. Stefanucci, *Physical review B* **75**, 195115 (2007).
- [62] E. Khosravi, S. Kurth, G. Stefanucci, and E. Gross, *Applied physics A* **93**, 355 (2008).
- [63] É. Jussiau, M. Hasegawa, and R. S. Whitney, *Physical review B* **100**, 115411 (2019).
- [64] R. Wakatsuki, M. Ezawa, and N. Nagaosa, *Physical review B* **89**, 174514 (2014).
- [65] D. Vodola, L. Lepori, E. Ercolessi, and G. Pupillo, *New journal of physics* **18**, 015001 (2015).
- [66] G. Dolcetto, M. Sasseti, and T. L. Schmidt, *La Rivista del nuovo cimento* **39**, 113 (2016).
- [67] G. Gusev, Z. Kvon, E. Olshanetsky, and N. Mikhailov, *Solid state communication* **302**, 113701 (2019).
- [68] D. Roy and A. Dhar, *Journal of Statistical Physics* **131**, 535 (2008).
- [69] A. Casher and J. Lebowitz, *Journal of mathematical physics* **12**, 1701 (1971).
- [70] V. Kannan, A. Dhar, and J. Lebowitz, *Physical review E* **85**, 041118 (2012).
- [71] Z. Rieder, J. Lebowitz, and E. Lieb, *Journal of mathematical physics* **8**, 1073 (1967).
- [72] H. Nakazawa, *Progress of theoretical physics* **39**, 236 (1968).
- [73] H. Nakazawa, *Progress of theoretical physics supplement* **45**, 231 (1970).
- [74] H. Furstenberg, *Transactions of the American mathematical society*. **108**, 377 (1963).
- [75] H. Crauel, P. Imkeller, and M. Steinkamp, “Bifurcations of one-dimensional stochastic differential equations,” in *Stochastic Dynamics* (Springer New York, New York, NY, 1999).
- [76] V. Wihstutz, “Perturbation methods for lyapunov exponents,” in *Stochastic Dynamics* (Springer New York, New York, NY, 1999) pp. 209–239.

- [77] H. Matsuda and K. Ishii, *Progress of theoretical physics* , 56 (1970).
- [78] E. Pardoux and V. Wihstutz, *SIAM journal on applied mathematics* **48**, 442 (1988).
- [79] V. Wihstutz, “Ergodic theory of linear parameter-excited systems,” in *Stochastic Systems: The Mathematics of Filtering and Identification and Applications*, edited by M. Hazewinkel and J. C. Willems (Springer Netherlands, Dordrecht, 1981) pp. 205–218.